AFRL-AFOSR-UK-TR-2013-0058

Control of Low Reynolds Number Flows with Fluid Structure Interactions

Professor Ismet Gursul

University of Bath
Department of Mechanical Engineering
Claverton Down
Bath BA2 7AY
UNITED KINGDOM

EOARD Grant 10-3093

Report Date: February 2014

Final Report from 01 October 2010 to 30 September 2013

Air Force Research Laboratory
Air Force Office of Scientific Research
European Office of Aerospace Research and Development
Unit 4515, APO AE 09421-4515

REPORT DOCUMENTATION PAGE

Form Approved OMB No. 0704-0188

1. REPORT DATE *(DD-MM-YYYY)*
02 February 2014

2. REPORT TYPE
Final Report

3. DATES COVERED *(From – To)*
1 October 2010 – 30 September 2013

4. TITLE AND SUBTITLE

Control of Low Reynolds Number Flows with Fluid Structure Interactions

5a. CONTRACT NUMBER

FA8655-10-1-3093

5b. GRANT NUMBER

Grant 10-3093

5c. PROGRAM ELEMENT NUMBER

61102F

6. AUTHOR(S)

Professor Ismet Gursul

5d. PROJECT NUMBER

5d. TASK NUMBER

5e. WORK UNIT NUMBER

7. PERFORMING ORGANIZATION NAME(S) AND ADDRESS(ES)
University of Bath
Department of Mechanical Engineering
Claverton Down
Bath BA2 7AY
UNITED KINGDOM

8. PERFORMING ORGANIZATION REPORT NUMBER

N/A

9. SPONSORING/MONITORING AGENCY NAME(S) AND ADDRESS(ES)

EOARD
Unit 4515
APO AE 09421-4515

10. SPONSOR/MONITOR’S ACRONYM(S)

AFRL/AFOSR/IOE (EOARD)

11. SPONSOR/MONITOR’S REPORT NUMBER(S)

AFRL-AFOSR-UK-TR-2013-0058

12. DISTRIBUTION/AVAILABILITY STATEMENT

Distribution A: Approved for public release; distribution is unlimited.

13. SUPPLEMENTARY NOTES

14. ABSTRACT

The purpose of this project is to is to investigate the possibility of exploiting the flexibility inherent to micro air vehicle structures to create small-amplitude oscillations that delay stall and increase lift. Initially two-dimensional rigid airfoils undergoing small-amplitude plunging oscillations are considered, this is then expanded to finite wings and finally flexible wings. For the 2D airfoil case two mechanisms of lift generation are identified: deflected jets for pre-stall angles of attack and convected leading-edge vortices for post-stall angles of attack. For rigid airfoils plunging with small-amplitude, two mechanisms of lift enhancement have been identified: deflected jets and convected LEVs. For finite wings oscillating at post-stall incidence, similar lift-enhancing convected LEVs are observed, however the flow field is more complicated. For oscillating flexible wings appropriate spanwise flexibility can significantly enhance lift performance. In terms of the flow field, the rigid wing exhibits weak vortical structures near the leading-edge, which are essentially the three-dimensional version of the LEV dipole observed for flat plate airfoils. Conversely the flexible wing exhibits a strong convected LEV, strong tip vortex and thus high lift.

15. SUBJECT TERMS

EOARD, Pressure Gain Combustion, turbine engines

16. SECURITY CLASSIFICATION OF:			**17. LIMITATION OF ABSTRACT**	**18, NUMBER OF PAGES**	**19a. NAME OF RESPONSIBLE PERSON**
a. REPORT	**b. ABSTRACT**	**c. THIS PAGE**			Gregg Abate
UNCLAS	UNCLAS	UNCLAS	SAR	126	**19b. TELEPHONE NUMBER** *(Include area code)* +44 (0)1895 616021

Standard Form 298 (Rev. 8/98)
Prescribed by ANSI Std. Z39-18

CONTROL OF LOW REYNOLDS NUMBER FLOWS WITH FLUID STRUCTURE INTERACTIONS

Contract No: FA8655-10-1-3093

Final Report

submitted to
Dr. Gregg Abate
Aeronautical Sciences Program Manager
Air Force Office of Scientific Research (AFOSR)
European Office of Aerospace Research and Development (EOARD)

and

Dr. Douglas R. Smith Civ USAF AFMC AFOSR/RSA
Flow Interactions & Control, Program Manager
Air Force Office of Scientific Research

by

Professor Ismet Gursul
Department of Mechanical Engineering
University of Bath
Bath, BA2 7AY
United Kingdom

October 2013

Summary

This is the final report for the project “Control of Low Reynolds Number Flows with Fluid Structure Interactions”. The purpose of this project is to investigate the possibility of exploiting the flexibility inherent to micro air vehicle structures to create small-amplitude oscillations that delay stall and increase lift. Initially two-dimensional rigid airfoils undergoing small-amplitude plunging oscillations are considered, this is then expanded to finite wings and finally flexible wings. For the 2D airfoil case two mechanisms of lift generation are identified: deflected jets for pre-stall angles of attack and convected leading-edge vortices for post-stall angles of attack. The deflected jets are formed through pairing of the trailing-edge vortices to form dipoles. Depending on the inclination of these dipoles they can self-advect upwards or downwards. The direction is determined by the initial conditions, and for the NACA 0012 geometry these deflected jets are stable resulting in very large lift coefficients: $C_l \approx 3.5$. It was shown that deflected jets form once the trailing-edge vortex circulation passes a threshold, and the direction (upwards / downwards) is determined by an asymmetry in the circulation of the trailing-edge vortices. Due to this asymmetry criterion the upwards deflected jet was not observed for post-stall angles of attack due to the overwhelming bias in the trailing-edge vortex strength with increasing angle of attack. The other method of lift generation, convected leading-edge vortices, is observed for post-stall angles of attack. At low Strouhal numbers time-averaged lift coefficient increases approximately proportionally with plunge velocity. Superimposed

onto this linear trend are several local optima due to resonance with the natural shedding frequency, its harmonics and subharmonic. At higher Strouhal numbers a significant fall in lift is observed, this is due to the development of a lower-surface leading-edge vortex, which counteracts the positive effect of the upper-surface leading-edge vortex, combined with the formation of a mode-2 flow field. A mode-2 flow field is defined as a flow where the upper surface leading-edge vortex forms during the downward motion but loses its coherency during the upward motion due to impingement with the upward moving airfoil. Conversely in a mode-1 flow field the leading-edge vortex forms but is shed and convected into the wake. A mode-1 flow field is generally associated with high-lift and a mode-2 with low lift. Nevertheless the switch from drag to thrust correlates very closely with the switch from mode-1 to mode-2 demonstrating the thrust enhancing effect of a mode-2 flow field. Geometry of the airfoil was shown to have a significant effect on both of these lift-enhancement mechanisms. For a flat plate geometry at high Strouhal numbers instead of convected leading-edge vortices, leading-edge vortex dipoles form. These are associated with low-lift and high-drag due to the large separation they promote. Furthermore although deflected jets still form for pre-stall incidences, these jets are unstable and periodically switch direction. It is suggested that this jet switching is driven by an instability created by the leading-edge vortices.

For rigid finite wings similar lift-enhancing convected leading-edge vortices are observed but with a generally more complicated three-dimensional flow field. Due to the finite wing the leading-edge vortex must anchor on the wing surface. The tip vortex then acts to drive this anchor point inboard creating an undulation in the leading-edge vortex. This effect is particularly pronounced for the elliptical planform. For certain cases the interaction between the upper-surface and lower-surface tip vortex can create vortex rings that expand in the spanwise direction. As one would expect the degree of lift enhancement is diminished by decreasing aspect ratio. In terms of deflected jets the finite wing is found to prevent their formation. It is suggested that this is due to one of two possible reasons. Either the tip vortex acts as an anchor point which dictates the shedding time and therefore prevents asymmetric vortex pairing, or the asymmetry in circulation that is characteristic of two-dimensional deflected jets cannot be supported for three-dimensional vortex rings due to Helmholtz's first theorem.

For finite flexible wings, flexibility can improve lift performance substantially. For the higher aspect ratio, $sAR = 3$, wing flexibility more than doubled time-averaged lift coefficient in comparison with its rigid counterpart. This increase in lift was associated with significant spanwise deformation of the wing. For a Strouhal number of $Sr_c = 1.5$, the tip lags the root by approximately 90^o but with an amplitude 1.84 times larger. The effect of this deformation on the flow field is to inhibit the formation of a leading-edge vortex ring and strengthening of the tip vortex. Similar results were observed a $sAR = 1.5$ wing.

Table of Contents

List of Figures

Nomenclature

A = Peak-to-peak amplitude

c = chord length

C_D = time-averaged drag coefficient, $\overline{F_x}/0.5\rho c s U_{\infty}^{2}$

C_L = time-averaged lift coefficient, $\overline{F_y}/0.5\rho c s U_{\infty}^{2}$

C_P = time-averaged power coefficient, $\overline{F_y U_{pl}}/0.5\rho c s U_{\infty}^{2}$

f = forcing frequency

F_x = instantaneous streamwise force

F_y = instantaneous cross-stream force

Re = Reynolds number

s = wing span

sAR = semi aspect ratio

Sr_A = Strouhal number based on amplitude, fA/U_{∞}

Sr_c = Strouhal number based on chord length, fc/U_{∞}

$Sr_{c,nat}$ = Strouhal number of the natural frequency

U_{pl} = instantaneous plunging velocity

U_∞ = freestream velocity

u = streamwise velocity

v = cross-stream velocity

w = spanwise velocity

x = streamwise direction

y = cross-stream direction

z = spanwise direction

α = angle of attack

λ = elastic parameter, $EI/0.5\rho U_\infty^2 s^3$

θ = phase lag relative to root

ω = vorticity magnitude

ω_z = spanwise vorticity

1. Introduction

This report serves as the final report for the project “Control of Low Reynolds Number Flows with Fluid Structure Interactions”. The purpose of this project is to utilize fluid-structure interactions to control separated flows, delay stall and increase lift.

Recent advances in micro-technology have created an opportunity to mount miniature surveillance equipment on small (wing span less than 15 cm) flying aircraft known as Micro Air Vehicles (MAVs). Such micro-technology includes tiny CCD cameras, infra-red sensors, and computer-chip sized hazard detectors. MAVs could be suitable for reconnaissance and surveillance, as well as numerous other applications such as coastal surveillance, crop monitoring, telecommunications, news broadcasting, remote sensing and mineral exploration. MAVs have similar dimensions to birds and insects, and similar Reynolds numbers. Mini Unmanned Air Vehicles (UAVs) are slightly larger, with correspondingly larger Reynolds numbers.

As the length scale of small aircraft is small and flight speed is low, the Reynolds number is low, typically $Re = 10^3$–10^5. At these low Reynolds numbers, separated and vortical flows are dominant, making lift and thrust generation challenging due to the strong viscous effects as discussed in recent review articles [1-4]. Because of the poor lift generation in cruise flight, it will be necessary for fixed-wing MAVs to fly at relatively high angles of attack, close to stall conditions. In addition, it may be necessary to fly in the poststall regime during vertical gusts. Hence, the delay of stall is necessary for stable MAV flight. High angle of attack flows with large separated regions are also typical for flapping-wing MAVs. Leading-edge vortices are known to enhance lift in unsteady aerodynamics. Periodic excitation of the flow to generate leading-edge vortices for fixed-wing MAVs is therefore a sensible approach.

Consequently, active flow control will be necessary. This can be achieved by means of unsteady blowing, suction, moving surfaces, and plasma actuators. However, these conventional flow control techniques such as blowing are not necessarily practical at these small scales, and often, the space available is insufficient to place actuators or blowing chambers. In addition, weight, volume and power consumption of the potential actuation systems need to be considered. For example, plasma actuators, when the power supply is considered, may not be practical at these small scales. In this project, we focused on the periodic excitation of separated flows by means of wing oscillations. Fluid-structure interactions can be exploited to control the separated flows, and thus increase lift and delay stall. Small aircraft are inherently lightweight and flexible, hence wing vibrations can be used to excite the separated flows.

1.1. Frequencies of fluid instabilities and wing structure

Extensive research on active flow control of separated flows around airfoils and wings has shown that partial or full reattachment is possible when the inherent instabilities in the separated flow are excited [5]. Depending on the airfoil shape and excitation characteristics, at least three different instabilities may be important for effective excitation: 1) initial shear layer instability or its subharmonics, although this appears to be more effective for delta wings [6]; 2) instability of the separation bubble [7]; and 3) wake instability [8,9]. Flow control research on separated flows suggests that the optimal Strouhal number of unsteady excitation is on the order of unity, $fc/U_\infty = O(1)$. Typically, the frequencies of the instability of the separation bubble and wake instability are on this order of magnitude. An alternative control strategy relying on much higher frequencies was also discussed by Glezer *et al.* [10].

Figure 1 shows the qualitative variation of the frequency of the fluid instabilities (corresponding to $fc/U_\infty = O(1)$) as a function of wing span. As the wing span increases from very small (MAVs) to large (civil transport aircraft), the frequency of flow instabilities does not vary much once variations in the wing chord length and flight speed are taken into account. Also shown on Figure 1 is the qualitative variation of the natural frequency of the wing structure. It decreases substantially with increasing wing span. For a typical civil transport, the structural frequency may be on the order of few Hertz, while typically this quantity is on the order of 10^2 Hertz for micro air vehicles. As illustrated in Figure 1, structural frequencies and fluid instability frequencies are therefore close to each other for small aircraft. This presents an opportunity to exploit wing vibrations for flow control purposes. For small aircraft, small-amplitude wing vibrations could potentially excite characteristic frequencies of the fluid instabilities.

While one tries to suppress the vibrations for large aircraft because of fatigue and passenger comfort issues, this requirement is not necessary for small aircraft (MAVs), because they have limited (much shorter) life time and no passengers. Thus, exploiting the flexibility of the wing structure to excite the fluid for flow control becomes a possibility at low Reynolds numbers. In practical applications, this technique can be achieved by the torsional (pitching) and bending (plunging) vibrations of flexible wings by means of piezoelectric actuators and/or elastic mounting of rigid wings. For example, if a torsional spring used for mounting is tuned correctly, airfoil/wing oscillations are easier to produce. External excitation at resonant structural frequencies for less power input or self-excited wing vibrations for zero power input can also be considered.

1.2. Small-amplitude high-frequency oscillations

As the main objective is to exploit the fluid-structure interactions for flow control, naturally small-amplitude and high-frequency wing oscillations are relevant. Here we will discuss the range of dimensionless parameters and compare with the biological flows where pitching and plunging motions are observed [11-13]. The first parameter is the Strouhal number based on the chord length,

$$Sr_c = f\,c\,/U_\infty \tag{1}$$

which can be considered as the ratio of two time scales (convective time unit and the period of the motion). Since it is related to the convection of the leading-edge vortices, this parameter is important in determining the unsteady lift. In biological flows, one observes large amplitude motion (amplitude on the order of chord length, $a/c = O(1)$) at low frequencies (Strouhal number based on the chord length, $Sr_c = fc/U_\infty = O(10^{-1})$). However, in our case, we have small amplitude motion ($a/c = O(10^{-1})$) at high frequency (Strouhal number, $Sr_c = fc/U_\infty = O(1)$). Hence, the kinematics is very different from the biological flows.

The second parameter is more relevant to the thrust generation. The history of the subject is given in the review article by Platzer *et al.* [14]. It has been shown that the most important parameter for thrust generation is the Strouhal number based on the amplitude, which is defined as:

$$Sr_A = f A / U_\infty , \tag{2}$$

where A is the peak-to-peak amplitude of the trailing-edge. This parameter can also be considered as normalized plunge velocity. It is also related to the maximum effective angle of attack $\alpha_{\text{eff, max}}$, through:

$$\alpha_{eff,\max} = \alpha + \tan^{-1}\frac{U_{pl}}{U_\infty} = \alpha + \tan^{-1}\frac{2\pi f a}{U_\infty} = \alpha + \tan^{-1}\pi Sr_A \tag{3}$$

where U_{pl} is the maximum plunge velocity. Interestingly, Strouhal number based on the amplitude, which is a measure of the change in the effective angle of attack due to the unsteady motion, is similar in nature and our case.

Even though the flows that we are interested in are very different from biologically inspired flows, we note that the flexibility of the wings in insects and birds has been documented [15,16]. There is a belief among biologists that wing flexibility improves the aerodynamics [17,18]. Therefore, even though the kinematics of the biological flows and the flows considered in this report are very different, we share the same goal, performance improvement through flexibility.

In this report as a starting point rigid airfoils in forced plunging motion are considered. As the frequency of the plunging motion is varied, various modes of vortex topology and two different mechanisms of high-lift production are identified. Then, so as to investigate planform and tip effects, this is extended to finite rigid wings. Finally the vortex dynamics and lift production of oscillating flexible wings are considered.

2. Methods, Assumptions and Procedures

Force, Digital Image Correlation (DIC), two-dimensional Particle Image Velocimetry (PIV) and volumetric velocimetry measurements were conducted for plunging rigid and flexible wings mounted vertically in a closed-loop water tunnel, see Figure 2. For a review of parameters studied, see Table 1; uncertainties are calculated based on the methods of Moffat [19] taking into account both bias and precision errors.

Table 1 Experimental Parameters

Parameter	Range Considered	Uncertainty
Re	10,000 to 20,000	+/- 200
α	0° to 20°	+/- 0.5°
a/c	0.025 to 0.20	+/- 0.003
Sr_c	0 to 3	+/- 2.3%

2.1. Experimental Setup

The experiments were conducted in a free-surface closed-loop water tunnel (Eidetics Model 1520) at the University of Bath. The water tunnel is capable of flow speeds in the range 0 to 0.5 m/s and has a working section of dimensions 381 mm x 508 mm x 1530 mm. The turbulence intensity has previously [20] been measured by LDV to be less than 0.5%.

Mounted on top of the tunnel is the experimental rig, see Figure 2. The oscillations were supplied via a Motavario 0.37 kW three-phase motor, 5:1 wormgear and IMO Jaguar Controller. The position of the root of the wings was measured through a rotary encoder attached to the spindle of the worm gear shaft. The rotary encoder was also used to trigger the DIC, PIV and volumetric velocimetry systems and determine the instantaneous velocity for the calculation of power coefficient.

For the two-dimensional airfoil cases a NACA 0012 and flat plate profile are considered, see Figure 3. Both wings have a chord of 0.1 m and span of 0.3 m. The NACA 0012 wing was constructed by rapid prototyping from SLS Duraform Prototype PA. It has two internal 8 mm diameter steel rods spanning from root to tip to ensure a high spanwise stiffness. The tip deformation was monitored with a digital camera and did not exceed 1% of the chord length for the largest amplitude and frequency. The flat plate wing was constructed from 4 mm mild steel plate, with a semi-circular leading and trailing edge. Both wings were placed between an upper and lower end plate with clearances maintained at 2 mm.

For the finite wing cases a total of four wings were tested, comprising of two elliptical and two rectangular flat plates, see Figure 4. Whilst the chord length (c) is kept constant at 100 mm, the span length (b) is varied to allow investigation into the effect of aspect ratio. A span length of 200 mm and 100 mm were explored for each planform shape. The wing profile has round, semi-circular leading and trailing edges with a thickness-to-chord ratio (*t*/*c*) of 0.03.

For the oscillating flexible case two wings are considered: *sAR* = 1.5 and 3. For *sAR* = 3, two rigidities are considered: a rigid flat plate (RFP) and a highly flexible plate (HFP). The RFP wing was fabricated from mild steel of thickness 0.04c. The HFP wing was of thickness 0.03c and fabricated from polyethylene. The flexible material was held in a mild steel holder to guarantee chordwise rigidity along the root, see Figure 5a. The deformation is therefore predominantly spanwise bending. The *sAR* = 3 wings have semi-circular leading and trailing edges and dimensions of 0.1 m chord and 0.3 m span. The rigidity of the highly flexible wing was measured as: $\lambda = 1.26$; the rigid wing can be taken as: $\lambda = 639.7$. For *sAR* = 1.5, one rigid (*t* = 1.5 mm) and four flexible (*t* = 1 mm) wings are considered. The rigid wind is manufactured from mild steel. The flexible wings are manufactured from PTFE (*E* = 800 MPa, measured), polypropylene (*E* = 1700 MPa, Matweb), polycarbonate (*E* = 2300 MPa, manufacturer specification), and nylon (*E* = 3000 MPa, Matweb). The flexible material was clamped in an interchangeable mild steel holder to guarantee chordwise rigidity along the root, see Figure 5b. The rigid wing is silver soldered into a separate holder to guarantee rigidity. The *sAR* = 1.5 wings have right-angled leading and trailing edges, and dimensions of 0.1 m chord and 0.15 m span.

2.2. Force Measurements

The forces in the streamwise (F_x) and cross-stream (F_y) directions were measured through a two-component binocular strain gauge force balance [21]. Four force balances of differing rigidities were used so as to achieve the desired accuracy whilst minimizing flexibility. The signal from the strain gauges was amplified by a Wheatstone bridge circuit and sampled at either 1 kHz for 20,000 samples (stationary cases), or 360 per cycle (dynamic cases). The forces were then calculated from the average voltage through linear calibration curves. The calibration curves consisted of twenty three points, and were performed daily before and after testing. Each data set consists of an average of at least four individual runs.

2.3. Digital Image Correlation Measurements

The deformation of the flexible wings was measured using a Limess DIC system. This consists of a pair of Photron SA3 cameras, which are capable of image acquisition with a resolution of 1024 x 1024 pixels at 1,000 fps, with the images processed in VIC-3D. Normally these cameras are mounted at an angle to each other to give depth information and the same field of view. In the current scenario this was not appropriate because refraction at the water-glass-air interface leads to image warping which will give erroneous results. To minimise this effect the cameras were instead kept parallel and the angle was created by angling the lenses with Scheimpflug mounts, see Figure 2b. The measurements were validated before each measurement by measuring the stationary rigid wing as it is manually moved through 5 mm steps in the range:

0 to 30 mm. The error was always less than 0.15% of the chord length. The calibration consisted of at least 60 images of a randomly orientated 12 x 9 grid. The majority of results shown herein are instantaneous results for Strouhal numbers of Sr_c = 0.075 to 2.025 with a Sr_c = 0.075 interval. These were acquired at a rate of twenty four images per cycle for a minimum of ten cycles. The midchord position, deformation, twist angle, effective angle of attack, amplitude, and phase along the span were then derived in MATLAB by taking 1 mm wide slices at regular spanwise locations. Due to the finite subgrid size (size of pixel area for cross-correlation) used in DIC processing it was not possible to perform measurements at z/s = 0 or 1. The wings shown in the PIV and velocimetry figures were built from the phase-averaged deformation measurements.

2.4. 2D PIV Measurements

The flow was seeded with 8 – 12 μm hollow glass spheres. The velocity field around the airfoil was measured using a TSI Inc. 2D-PIV system incorporating a dual ND:YAG 50 mJ pulsed laser, 2 MP Powerview Plus 12 bit CCD camera and TSI Model 610034 synchronizer. For the measurements over the upper surface the laser was positioned behind with the camera below, see Figure 6a. The shadow created by the airfoil therefore obscured the lower surface. For measurements over the lower surface the laser was rotated 90 degrees, see Figure 6b. The PIV images were analyzed using the software Insight 3G using an FFT correlator with interrogation windows of 32 x 32 pixels to generate a vector field of 99 x 73 vectors, approximately giving a 2 mm spatial resolution.

Upper and lower surface measurements were performed for the *sAR* = 3 flexible wing at *z/s* = 0.05 intervals from *z/s* = 0.05 to 1.20, to give 24 individual planes.

2.5. Volumetric Velocimetry Measurements

The volumetric flow measurements were acquired using a three-component velocimetry (TSI V3V™) system based on the techniques developed by Pereira et al. [22] for defocusing digital particle image velocimetry (DDPIV). The flow was seeded with 50 μm hollow glass particles. The volume of interest was illuminated using a dual ND:YAG 200 mJ pulsed laser, equipped with two cylindrical lenses offset by 90 degrees from each other to generate a laser cone, see Figure 7a. The laser cones were fired 700 μs apart. The images were acquired using three 4MP 12 bit CCD cameras placed to form an equilateral triangle whose common focal plane defines the most distant plane within the volume of interest. DDPIV uses multiple off-axis apertures to generate multiple defocused particle images where the particle’s separation distance and location give its position in three-dimensional space. If the three images of a single particle were superimposed, the particle would appear as a triangle with its centre equating to its x-y coordinates and the size of the triangle equating to its z coordinate. The cameras were calibrated by translating a rectangular plate of regularly spaced grid dots across the volume of interest with image triplets acquired at 5 mm intervals to generate a camera signature graph.

There are four stages from image to gridded velocity data. First the particles are identified in each of the 6 captured images (two times of three), using a 2D particle identification algorithm. Second, using the triangles generated during the calibration stage the particles are grouped between the three images to form complete triplets. This gives two sets of three-dimensional particle coordinates equating to the two times. Third, the particles are 'tracked' through a 3D particle tracking algorithm using the relaxation method first proposed by Baek and Lee [23]. This essentially uses an iterative process to update the probability of two particles matching between two frames, at each step, using neighbour particle displacement similarity criteria as well as flow estimates, and then choosing the particle match with greatest probability. This is outlined in more detail by Pereira et al. [24]. A median filter was applied to remove any outliers. Finally the randomly spaced vectors from 200 separate phase-locked measurements are interpolated onto a uniformly spaced grid of voxel size 8 mm with a 55% overlap to give phase-averaged uniformly spaced velocity vectors. The grid interpolation produced 25,000 to 37,000 grid vectors within a measurement volume of 140 × 140 × 90 mm.

In all cases to capture the entire region of interest it was necessary to perform measurements separately for multiple volumes and then merge these volumes. In the case of the rigid wings this was generally successful and it was possible to take measurements close to the wings' surface. However, for the flexible wings the region above the upper surface of the wing was largely obscured in several phases by the wing itself, see Figure 8. This effect was particularly severe for the larger aspect ratio more flexible wings due to the larger deformation. It was not possible to angle the cameras due to the image warping that would be created by the water-glass-air interface, and a water prism was not practical due to the obstruction created by the water tunnel's structural supporting bars (see Figure 7a). Instead to capture data within the obscured region two methods were used. For the sAR = 3 rigid and flexible wings measurements were performed using 2D-PIV with the camera tilted six degrees to the horizontal. This angle will create image warping so that measurements will differ across the area of interest. To quantify this error, time-averaged measurements were performed for the same area in the centre of the tunnel, with no model, with and without an angle applied. The difference between the two sets of measurements is less than 1% of the freestream velocity, see Figure 9. However, 2D-PIV only acquires the u and v components of velocity so it is not possible to derive chordwise vorticity, cross-stream vorticity, or vorticity magnitude. The question therefore arises is it appropriate to use only spanwise vorticity in the obscured region? In answer, shown in Figure 10 is an isosurface of $\omega c/U_\infty$ = 25 overlaid with contours of ω_z/ω acquired using DDPIV. Where the isosurface is dark red or blue, over 95% of the vorticity is spanwise. In the region z/s = 0 to 0.9 the flow is therefore predominantly two-dimensional and it is appropriate to use 2D-PIV measurements. The u and v components of velocity from the 2D-PIV measurements were therefore used to fill in the obscured region in the volumetric data in the region z/s = 0 to 0.9, with only

DDPIV data used outside of this region. The five volumes of DDPIV and twenty-four slices of 2D-PIV data were combined in MATLAB through interpolation onto a common grid. For *sAR* = 1.5 the problem of the obscured region was overcome by performing measurements with the DDPIV camera angled from the side of the water tunnel, see Figure 7b. To minimize the effect of laser reflections from the wing's upper surface the V3V images were pre-processed using a mean image subtraction routine.

Once the volumes were merged the desired flow properties such as vorticity magnitude were then calculated. These flow properties were imported into Tecplot 360™ for plotting, along with a model of the wing built from the phase-averaged DIC measurements.

3. Results and Discussion

3.1. Lift enhancement of oscillating rigid airfoils

3.1.1. Two mechanisms of high-lift

Figure 11 illustrates two high-lift mechanisms for an airfoil oscillating with small amplitude: a) leading-edge vortices for post-stall angles of attack; b) deflected trailing-edge vortices for pre-stall angles of attack. In the first mechanism, for the stationary airfoil the flow is fully separated at the leading-edge and therefore part of the suction is lost. For the oscillating airfoil, a LEV is produced during the downstroke and once formed it convects over the upper surface creating a low-pressure wave as it passes. Extremely small amplitude oscillations of a SD7003 airfoil at a post-stall incidence have been shown to increase time-averaged lift [25]. Furthermore, small amplitude airfoil oscillations for a NACA0012 airfoil [26] and a flat plate airfoil [27] at a post-stall incidence have also been studied. Various experimental methods including particle image velocimetry (PIV) measurements and force measurements were combined with high-fidelity simulations. These findings highlight the delay of stall and lift enhancement on oscillating airfoils, and also identify an interesting phenomenon due to a strong interaction between the airfoil and vortex. In this new mode of vortex topology, a leading-edge vortex is generated during the downward motion of the airfoil and then impinges on the upward moving airfoil, resulting in rapid loss of its coherency. As a result in this flow regime no coherent vortices are convected downstream over the suction surface of the airfoil, which has a considerable effect on the aerodynamic forces.

In the second mechanism shown in Figure 11, asymmetric wake flow can be observed at even zero angle of attack if the Strouhal number is sufficiently high. This asymmetric flow generates non-zero time-averaged lift. For zero mean angle of attack, various studies of plunging airfoils [28-32] and pitching airfoils [33-35] showed that asymmetric wake flows are possible at high Strouhal numbers. Emblemsvag *et al.* [33] was the first to suggest that, at high frequencies, the vortices tend to shed in pairs (vortex dipoles) and this triggers the deflected wakes. Hence, dipole formation is important and becomes more likely with increasing frequency due to the decreasing distance between the vortices and increasing strength of the vortices. A symmetry breaking criterion, based on a simple model of a dipole and its self-induced velocity, was suggested by Godoy-Diana *et al.* [35]. The model was developed based on the measured strength of the vortices and the phase velocity of the vortex street for zero mean angle of attack. It will be shown in this report that deflected flows are possible up to the stall angle, resulting in very high time-averaged lift coefficients. The details of these two high-lift mechanisms are discussed below.

3.1.2. Leading-edge vortices

Figure 12 shows the variation of the time-averaged lift coefficient as a function of Strouhal number based on the chord length for a NACA 0012 airfoil at a post-stall angle of attack of 15 degrees and a Reynolds number of 10,000 for different amplitudes [26]. It is seen that significant lift enhancement is possible, which increases with increasing amplitude until a critical high frequency is reached. The sudden drop in the lift for larger amplitudes will be discussed below. Up to $Sr_c \approx 0.5$, the increase in the time-averaged lift is monotonic, and, in fact, it has been shown that the lift increase is approximately proportional to the Strouhal number based on the amplitude [26]. At around $Sr_c \approx 0.5$, there is a local maximum, which is visible for almost all amplitudes. For the largest amplitude $a/c = 0.20$, the lift coefficient is also given for $Re = 20{,}000$. The same peak has been found, revealing no effect of Reynolds number. In Figure 12, a second peak around $Sr_c \approx 1.0$ and third peak around $Sr_c \approx 2.0$ are also visible. We note that a peak was observed at a Strouhal number of $Sr_c \approx 0.4$ in the direct numerical simulations of Andro and Jacquin [37] for a plunging NACA 0012 airfoil at *Re* = 1,000. In their case, the peak was attributed to an optimal interaction of the leading-edge vortices with the airfoil. We shall return to the physical mechanisms behind these peaks later on.

Figure 13(a) presents the streamlines and the magnitude of the total velocity vector for the stationary NACA 0012 airfoil at a post-stall angle of attack of 15 degrees for *Re* = 10,000. The large region of separation becomes much smaller when the airfoil is plunged periodically with small amplitude as shown in Figure 13(b). With increasing Strouhal number, the flow becomes more attached, leading to increased lift as well as reduced drag in agreement with the direct force measurements shown in Figure 12. In fact, at high Strouhal numbers, a time-averaged jet is formed downstream of the trailing-edge, which indicates thrust generation.

Figure 14 shows the vorticity in the phase-averaged flow field at the top and bottom of the plunging motion for different Strouhal numbers. For Strouhal numbers less than Sr_c = 2.5 the main feature is the generation of leading-edge vortices during the downward motion and their subsequent convection downstream. Other features such as generation of secondary vortex of opposite sign and vortex interactions and merging in the wake are less important. Consequently we call this type of flow: *mode-1*, where the LEV is basically convected. Figure 14(e) shows a *mode-2* flow field. Here the LEV is formed during the downward motion and loses its coherency entirely during the upward motion due to the impingement with the airfoil. This form of flow field (no convected LEV) does not arise abruptly; Figure 14(d) shows a mixed mode. A time history of a mode-2 vortex flow is presented more clearly in Figure 15 for a larger plunge amplitude (a/c = 0.10). The dramatic vortex-airfoil interaction and loss of vortex coherency are visible during the upward motion of the airfoil (Figure 15e to h).

Figure 16 shows the boundary between the mode-1 and mode-2 in the amplitude-Strouhal number plane. The boundary is illustrated as a shaded region, where the flow field is of mixed mode (there is a discernible convected LEV, but it is very weak). Different vortex topologies in mode-1 and mode-2 flow fields affect the time-averaged forces significantly. It is seen that the boundary region correlates well with the zero time-averaged drag points. Hence, in the mode-1 region there is drag, while the mode-2 region generates thrust. Also, there is usually high-lift in mode-1, but low-lift in mode-2. In Figure 16, lines of constant maximum effective angle of attack are shown, which can also be considered as the lines of constant plunge velocity (or Strouhal number based on the amplitude), as discussed with Equations (2) and (3) earlier. Since the mode-switch band occurs in the approximate range of $\alpha_{\mathrm{eff,max}} = 48°$ to $\alpha_{\mathrm{eff,max}} = 68°$, or alternatively $Sr_A = 0.20$ to $Sr_A = 0.43$, one can conclude that the mode-switch does not bear a strong correlation with either constant effective angle of attack or constant Strouhal number based on amplitude. So in a similar manner to the observations of Young and Lai [38] for drag, neutral and thrust wakes, wake structure regions do not follow lines of constant Strouhal number based on amplitude.

It is interesting to consider the time-averaged lift in the amplitude-Strouhal number plane, and relate this to the mode-1 and mode-2 flows. As the frequency (Strouhal number based on the chord length) or amplitude is increased, the plunge velocity (or “excitation” velocity) is also increased. Therefore, excitation level is not constant when either the frequency or amplitude is varied. In order to take this into account, we define a modified lift coefficient based on the vector sum of the free stream velocity and maximum plunge velocity:

$$\hat{C}_l = \frac{L}{\frac{1}{2}\rho(U_\infty^2 + U_{pl}^2)c} \tag{4}$$

Figure 17 shows a contour plot of the modified lift normalized by the lift coefficient of the stationary airfoil, as a function of amplitude and Strouhal number based on the chord length. The most apparent feature of Figure 17 is the existence of three regions of optimal excitation with their Strouhal number ranges centered around Sr_c = 0.5, 1.0, and 2.0. It is interesting that the three regions are located on a constant plunge velocity of $U_{pl}/U_\infty = 0.5$ shown with a dashed line in Figure 17. Hence, the optimum plunge velocity is approximately half the free stream velocity. The band shown with the two solid lines is the same region that separates mode-1 and mode-2 flow fields as discussed earlier.

Hence, all three optimal operating conditions have a mode-1 flow field, confirming that convected leading-edge vortices provide the most efficient conditions for maximizing the time-averaged lift. Hence the mode-2 flow field is associated with a loss of lift.

Returning to the frequency range of the optimal excitation conditions shown in Figure 17, these regions are closely related to the natural shedding frequency measured in the wake [26]. The measurements suggest that the optimal frequencies are related to the fundamental, subharmonic and the first harmonic of the natural shedding frequency. This agrees with earlier observations of the vortex lock-in phenomenon in the wakes of the stalled airfoils [8,9]. One expects that when oscillated at the natural shedding frequency, its harmonics or subharmonics, the wake becomes more ordered and synchronized, with an increased spanwise correlation of the flow, in a similar manner to vortex lock-in of oscillating cylinders [39]. This was confirmed for the periodically plunging airfoil at a post-stall incidence [26].

Finally, we return to the sudden drop of the time-averaged lift for larger amplitudes in Figure 12. Figure 18 shows that, at high Strouhal numbers, a lower-surface leading-edge vortex forms. This is best illustrated in Figure 18(d) for the largest Strouhal number. The lower-surface vortex strengthens rapidly with increasing Strouhal number, and becomes nearly equal to the circulation of the upper-surface vortex [26]. As the low pressure region induced by the lower-surface vortex counteracts the lift, we observe a decrease in the lift eventually resulting in a time-averaged lift coefficient comparable to that of a stationary airfoil.

3.1.3. Bifurcated/asymmetric flows

For zero mean angle of attack at high Strouhal numbers, the symmetry may be broken by deflected jets. Figure 19 shows the transition towards symmetry breaking with increasing Strouhal number. Thus there is the possibility of asymmetric flow fields and non-zero lift even at zero angle of attack. As this phenomenon is related to the formation of vortex dipoles, it is believed that the trailing edge vortices alone are responsible for deflected jets and any criteria should be derived from their properties. This is supported by the results of Jones *et al.* [28], who simulated deflected jets with an inviscid unsteady panel code, where no leading-edge vortex exists because separation is not modelled. Nevertheless, we will also show that the leading-edge vortex may influence the stability of the deflect jet. For the stable case the direction of the deflection (upwards or downwards) is determined by the sign of the starting vortex when the airfoil starts to move up or down [28]. For non-zero mean angles of attack, it also depends on the angle of attack [36], indicating that starting vortex as well as the bound vortex play a role. Usually the stable deflected flow field is established within a couple of plunge cycles.

Figure 20 shows the time-averaged lift coefficient [36] for various angles of attack in the range 0° to 20° for $a/c = 0.15$. For angles of attack less than or equal to the stall angle (10° in this case), at high Strouhal numbers, significant bifurcations are observed in the time-averaged lift coefficient resulting in two lift coefficient branches. The upper branch is associated with an upwards deflected jet, and the lower branch is associated with a downwards deflected jet. These branches are stable and highly repeatable, and are achieved by increasing or decreasing the frequency in the experiments. Increasing frequency (solid line) refers to starting from stationary and increasing the frequency very slowly (while waiting for the flow to reach a stable asymptotic state after each change in frequency); decreasing frequency (dashed line) refers to impulsively starting at the maximum frequency and decreasing the frequency very slowly. The upper branch is termed *mode A* and the lower branch is termed *mode B*. It is seen that, when there are two branches, the lift coefficient for mode A can be very high, in fact higher than those due to the leading-edge vortices discussed previously. For Strouhal numbers less than the bifurcation point the lift coefficient is the same for increasing and decreasing frequency. For angles of attack larger than the stall angle, there are no longer distinct branches and the lift for both increasing and decreasing frequency matches with only minor hysteresis for $\alpha = 12.5^\circ$.

Shown in Figure 21 is time-averaged velocity for typical pre-bifurcation, mode A and mode B flow fields at zero angle of attack. The pre-bifurcation flow field in Figure 21(a) shows a jet aligned horizontally, whereas Figure 21 (b) and (c) reveal deflected jets. For mode A, the time-averaged jet is deflected upwards and there is a high-velocity region over the upper surface, while for mode B the inverse is true. The time-averaged lift data shown in Figure 20 and the time-averaged velocity in Figure 21 reveal that the lift direction is the same as the direction of the vertical component of the deflected jet, i.e., mode A is associated with positive lift and mode B with negative lift. This is consistent with the simulations performed at much lower Reynolds numbers [32,33]. This relationship between the direction of the lift and the direction of momentum in the deflected jet is contrary to what one would intuitively expect. However, a simple control volume analysis [36] applied to the measurement domain shown in Figure 21(c), shows that the momentum flux terms are small compared to the measured lift, and therefore the time-averaged lift is dominated by the pressure difference resultant from the velocity difference over the upper and lower surfaces.

Figure 22 reveals the details of the vortex dipole formation. For mode A, a clockwise trailing-edge vortex (TEV) forms during the upward motion and loiters near the airfoil during the downward motion during which the counter-clockwise TEV forms. Due to the relative positions of the vortices, the resulting dipole has a self-induced velocity in the upwards direction, thereby creating an upwards deflected jet. For mode B, similar events occur but mirrored in the *x*-axis and phase-shifted by *T*/2. Due to the asymmetry of the flow near the trailing-edge, asymmetry is also created near the leading-edge. Mode A has a stronger upper-surface LEV, which also explains the higher time-averaged velocity above the upper surface. For mode B, the inverse is true: stronger lower-surface LEV causes higher time-averaged velocity over the lower surface.

For non-zero angles of attack, Figure 23 reveals that similar dual flows exist, which is expected based on the upper and lower branches of the time-averaged lift shown in Figure 20. Phase-averaged vorticity contours for mode A (left column) and mode B (right column) are qualitatively similar for $\alpha = 0°$, 5°, and 10°. There is a slight increase in the distance between the vortices of the dipole with increasing angle of attack for mode A, while this effect appears to be very small for mode B. For other oscillation amplitudes, except for small values $a/c \leq 0.05$, bifurcation of the lift and the main features of the flow fields are similar, but with bifurcation at different values of Strouhal number. For small amplitudes ($a/c \leq 0.05$), bifurcation was not observed within the range of Strouhal numbers tested ($Sr_c \leq 3.0$). This is shown in Figure 24 in the amplitude-Strouhal number plane. It is postulated that bifurcation may still be possible for these smaller amplitudes but at very high Strouhal numbers beyond the range of the experiments. The effect of geometric angle of attack on the boundary of the single/dual flow fields appears to be small. It is also seen that this boundary takes place in the thrust producing region.

As the bifurcation occurs at different Strouhal numbers based on the chord length for different amplitudes *a/c*, Strouhal number based on amplitude and effective angle of attack due to the plunging motion can be considered as possible criteria in determining the onset of deflected jets. Figure 25 shows the variation of the maximum and minimum effective angles of attack as a function of Strouhal number based on the amplitude. The bifurcation points for different oscillation amplitudes are shown on the diagram. It is seen that there is some correlation: the onset of bifurcation fall within the range $Sr_A = 0.45 \pm 0.07$ and $\alpha_{eff,\ max} = 60° \pm 9°$. However, these criteria cannot explain why there is no bifurcation at larger angle of attack and there is also a monotonic decrease in $Sr_A\ /\ \alpha_{eff}$ with decreasing amplitude which suggests it is not a universal criterion. Instead, in a similar manner to Godoy-Diana *et al.* [35], better correlations and insight can be derived from the measurements of the trailing-edge vortices. It was found [36] that as the difference in the absolute value of the circulation of the clockwise and counter-clockwise vortices increases there is stronger trend towards a downwards deflected flow. This difference in circulation grows with increasing angle of attack. Thus, at a post-stall angle of attack of $\alpha = 15°$, stronger counter-clockwise vortex and weaker clockwise vortex cause the flow to be heavily biased towards a downwards deflected jet, and this is therefore the only mode that exists. Similarity of this single post-stall mode to the pre-stall mode B is shown in Figure 26. Given the very strong similarity, it is appropriate to classify this single flow field as a mode B. Given the significance of asymmetry as a key mechanism, a new parameter is suggested based on the angular velocity of a vortex pair [40]:

$$\frac{(\Gamma_{T+} + \Gamma_{T-})}{d^2} \qquad (5)$$

where *d* is the distance between the vortices. This is made dimensionless as:

$$\frac{(\Gamma_{T+} + \Gamma_{T-})c}{U_\infty d^2} \qquad (6)$$

This represents a non-dimensional TEV *asymmetry parameter*. The current results suggest this parameter determines whether the time-averaged jet is deflected upwards or downwards.

A second parameter, which has been found to be important, is a strength parameter, derived from the average of the circulations of the TEVs. Figure 27 shows the data points in the plane of the asymmetry parameter versus this normalized circulation parameter. The horizontal line separates the single and dual flow modes. A vertical line separates mode A and mode B. If the circulation parameter is less than a critical value (for small amplitudes and frequencies), there is only one flow field. For larger values of circulation parameter, dual flows exist. If the asymmetry parameter is less than a critical value, mode A is generated. For larger values of the asymmetry parameter, only mode B is produced. At large angles of attack, the asymmetry parameter is large even in the pre-bifurcation range. Indeed for α = 15°, all of the data points are on the mode B side, making a mode B flow field the only possible outcome. Therefore mode B is selected as shown in Figure 26 for α = 15°.

In Figure 28, the circulation parameter is defined based on the plunge velocity instead. It is seen that there is a clear boundary between the single and dual modes with minimal scatter of the data. The critical value of circulation normalized by plunge velocity is $\overline{\Gamma}/U_P\, c = 1.85$. The circulation normalized by the plunge velocity, $\Gamma/U_p\, c = \Gamma/(2\pi fac)$, can be also interpreted as the inverse of a modified Strouhal number based on the dipole velocity Γ/a, the frequency and chord length.

3.1.4. Effect of airfoil shape

The airfoil shape can have significant effect on both of these high-lift mechanisms (leading-edge vortices and asymmetric flows). For a post-stall angle of attack of 15 degrees, Figure 29 compares the time-averaged lift and drag coefficients for a NACA 0012 airfoil and a thin flat plate as a function of Strouhal number at different oscillation amplitudes [27]. For fixed-wing aircraft, thin airfoils are generally preferable at low Reynolds numbers [41]. It is seen in Figure 29 that there are strong similarities for the time-averaged lift [27]. The peaks in the lift and the Strouhal numbers at which these peaks occur are similar. This is consistent with earlier explanations of the origin of the peaks, namely, resonance with the wake instabilities. The wakes of stationary airfoils at post-stall angles of attack are likely to be similar as the flow separation takes place at the leading-edge. Comparable lift is produced for the flat plate up to a Strouhal number of unity, but after this, the lift decreases. In terms of drag, while thrust generation occurs for the NACA 0012 airfoil with increasing Strouhal number and amplitude, thrust is never produced for the flat plate.

These features can be understood by the comparison of the time-averaged velocity (Figure 30) and phase-averaged vorticity (Figure 31) for different Strouhal numbers. For a small amplitude $a/c = 0.025$, it is seen in Figure 30 that the time-averaged flows look similar for the two airfoils for Strouhal numbers up to $Sr_c = 1.0$. Whereas beyond this value, the flow separation region becomes larger for the flat plate whilst separation almost disappears for the NACA 0012 airfoil. This trend is also visible in the phase-averaged vorticity fields shown in Figure 31. Particularly for $Sr_c \geq 2.0$, for the flat plate geometry the leading-edge vortices are convected almost parallel to the free stream and much further away from the airfoil surface. This causes decreased lift and increased drag, and explains why thrust is never achieved.

For a larger amplitude of $a/c = 0.15$, a new phenomenon is observed as shown in Figure 32. In this figure, the vorticity fields are in a counter-clockwise loop starting at the top of the motion in the top left corner, moving down through the left column to the bottom of the motion in the bottom right, and then up through the right column back to the start. At $t/T = 0$ there is a clear, strong counter-clockwise lower surface LEV. This interacts with the boundary-layer to form clockwise vorticity. During the initial stages of the downward motion (*t/T* = 0 to 2/12) this clockwise vorticity forms a vortex that pinches off by the point of maximum effective angle of attack (*t/T* = 3/12). This clockwise vortex pairs with the counter-clockwise to create a vortex dipole that convects away from the leading-edge in an upstream direction (*t/T* = 2/12 to 7/12). During this "vortex ejection" both vortices rapidly dissipate. This dissipation in the phase-averaged flow is an indication of the vortices becoming highly three-dimensional. This flow results in low lift and high drag. In contrast, this phenomenon was never observed for the NACA 0012 airfoil, and there is no sign of interaction between the upper- and lower-surface LEVs.

The second high-lift mechanism (asymmetric/bifurcated flows) was also investigated for the flat plate airfoil [27]. For zero angle of attack at high Strouhal numbers, the flat plate experiences deflected jets that are prone to periodic oscillations in direction, resulting in oscillation of the lift coefficient with a period on the order of 100 cycles. This is shown in Figure 33. Crosswise coordinates of the clockwise and counter-clockwise TEVs are shown in Figure 33(a) for the same phase (when the airfoil is at the bottom of motion) in each cycle. These phase-locked measurements show that the location of the vortices varies periodically. The circulation of these vortices also varies for the same phase in each cycle. The period of the oscillations is two orders of magnitude larger than the plunging period. It is interesting that this type of unstable jets was previously observed for rigid and flexible airfoils oscillating in still fluid [30] with a very similar oscillation period of around 100*T*. As a result of these periodic switches in the direction of the jet, the lift force fluctuates. Figure 33(d) shows the variation of *period-averaged* lift coefficient, which reveals oscillations that are approximately sinusoidal with an amplitude of $C_l \approx 5$.

For the flat plate, one can observe similar deflected vortex dipoles to those of the NACA 0012 airfoil during the peak deflection angles of the periodic oscillations. This is shown in Figure 34 for mode A, where the TEV dipoles appear very similar even though this is a stable flow for the NACA 0012 airfoil and unstable for the flat plate. Conversely the location and strength of the LEV differs significantly which would suggest that the jet switching is driven by an instability created by the LEV.

3.2. Lift enhancement of oscillating rigid finite wings

3.2.1. Coupling with wake instabilities

Resonance with the wake instabilities also exists for low-aspect-ratio wings [42-44]. Figure 35 presents a comparison of the time-averaged lift coefficients of the two-dimensional airfoil and the (semi-aspect ratio) $sAR = 2$ rectangular wing with NACA0012 cross-section. Both wings are subject to an oscillating amplitude of $a/c = 0.15$ and a geometric angle of attack of $\alpha = 20°$. Overall the optimal frequencies are quite similar between the two wings with peaks observed at $Sr_c \approx 0.5$, $Sr_c \approx 0.9$ and $Sr_c \approx 1.5$ for the low aspect ratio case. The peaks that we observe for the low aspect ratio wing, illustrate that the phenomenon is not confined to quasi-two-dimensional flows. Force measurements were also carried out at a different Reynolds number of *Re* = 20,000, illustrating similar lift performance. Considering, similar Strouhal numbers require different forcing frequencies, due to the change in freestream velocity, the existence of similarly located peaks reinforce that this is a fluid dynamic phenomenon. As previously mentioned, the lock-in phenomenon with the sub-harmonic and harmonic of the natural vortex shedding frequency, in the case of a two-dimensional NACA0012 airfoil, provides an explanation for the existence of peaks in lift. Similar measurements of the wake vortex shedding frequency have been performed and summarized in Figure 36. It is seen that, for the angle of attack of $\alpha = 20°$ (corresponding to Figure 35), we observe a vortex shedding frequency of $Sr_c \approx 0.54$, which is significantly closer to the first peak in lift. Even at very low Reynolds numbers (*Re* = 300-500), vortex shedding from low-aspect-ratio wings has been reported [45].

Measurements of wake vortex shedding frequency for other angles of attack are also shown in Figure 36. A comparison is made with the vortex shedding frequencies reported by Rojratsirikul *et al.* [46], indicated by the shaded region, which includes various aspect ratios (*AR* = 1 - 10, and also 2D airfoils) and Reynolds numbers in the range of 10,000 to 120,000. This is superimposed by a dashed line of constant Strouhal number $Sr_d \approx 0.17$, as proposed by Rojratsirikul *et al.* [46], for which the projected height is used, instead of the chord length, as the characteristic length. The wake measurements for the *sAR* = 2 wing reveal a good fit with the literature. Superimposed within the same graph are the locations of the first and second peaks in the time-averaged lift for various angles of attack. It is seen that the first peak for α = 20°, is very close to the natural vortex shedding frequency in the wake. However, for α = 10°, the data seem to suggest that the first peak could be the sub-harmonic of the natural vortex shedding frequency. The interpretation is even more difficult for α = 15°, for which the first peak of the lift is between the fundamental and the subharmonic of vortex shedding. It is apparent that the peaks in lift are on the same order as the frequencies of the wake instabilities of the stationary wing. However, the first peak remains remarkably unchanged for all three incidences, while the fundamental frequency of the wake instability and the second peak varies. The same is observed in the case of a flat plate wing with the same aspect ratio. This brings the question whether or not any other phenomenon might be contributing to the selection of the optimal frequency. This is discussed below for both the NACA 0012 and flat plate cross-sections.

Velocity magnitude and streamlines in the mid-span plane are shown in Figure 37 for the *sAR* = 2 wing with the NACA 0012 cross-section. Two phases in the cycle, corresponding to the halfway point and bottom of the downstroke, are shown at different operating Strouhal numbers. The two phases here give a good indication of the progression of the LEVs and TEVs at the early stages of their formation. Here Sr_c = 0.45 corresponds to the frequency at which the first peak in lift is observed (see Figure 35). With increasing frequency the leading edge vortex becomes more compact. In relation to the peaks that we observe in the time-averaged lift measurements, $Sr_c \approx 0.6$ corresponds to a local trough and $Sr_c \approx 0.9$ corresponds to the second peak. There is an apparent interaction between leading edge vortex and trailing edge-vortex for $Sr_c = 0.6$. In essence, the Strouhal number determines when the LEV reaches the trailing edge of the wing, yielding frequencies that synchronize the passing of the LEV with the formation of the TEV. Such appears to be the case at $Sr_c = 0.6$ and in the process, the LEV forms a dipole with the TEV. Due to the positioning and orientation of these two vortices, their induced velocity is directed upstream. At $Sr_c = 0.9$ the wing appears to recover somewhat, due to the delay of the leading edge vortex in reaching the trailing edge of the wing, significantly reducing the width of the wake. Consequently, the interaction between the leading edge and trailing edge vortices appears to contribute to the selection of optimal frequencies for lift.

Figure 38 shows iso-surfaces of constant velocity magnitude and vorticity magnitude in volumetric measurements over the $sAR = 2$ flat plate wing. The three frequencies here are very close to peaks and troughs observed in the time-averaged lift measurements. Similarities can be observed with respect to the size and location of the leading and trailing edge vortices, at the midspan of the wing, when comparing the 2D and 3D measurements. At $Sr_c = 0.4$, vortex dipoles are absent along the span, however, at $Sr_c = 0.6$ a vortex dipole is observed at a further location inboard of the midspan, and evidently absent closer to the tip beyond the leading edge vortex. For $Sr_c = 0.8$, there seems to be very little difference in streamline pattern inboard of the midspan location. Iso-surfaces of velocity magnitude illustrate that in the case of Sr_c = 0.6, a stronger interaction between the LEV and TEV is nonetheless observed close to the midspan of the wing.

3.2.2. Main features of the vortical flows

A comparison of the computed and experimental results [47,48] for the sAR = 1 rectangular wing plunging at Sr_c = 0.65 is shown in Figure 39. The flow is reflected about the wing centerline (z = 0) with the assumption of lateral symmetry. (Note that the calibration process near the end plate resulted in a small region with no data). The three-dimensional phased-averaged flow structure is represented using the iso-surface of the Q-criterion (Qc/U_∞ = 20). Overall good agreement is observed between experiments and computations in terms of the main flow features. As the wing plunges downward (Figure 39b-e), a leading-edge vortex is formed due to the increasing effective angle of attack. This vortex is fairly coherent in the spanwise direction and is pinned at the front corners of the plate. The formation and strengthening of the tip vortices is also observed during the downstroke motion. The tip vortices join with the trailing-edge vortex (containing vorticity generated on the bottom plate surface) to form a vortex loop extending from one wing front corner to the opposing edge. These features are consistent with the vortical structures observed over finite wings previously [45,49-55].

In Figure 39, spanwise undulations of the leading-edge vortex are observed near the end of the downstroke (Figure 39f, g). The leading-edge vortex evolves into an “arch-type” structure similar to that found by Visbal [56]. The legs of the arch-vortex move downstream and towards the wing centerline. During the upstroke, the tip vortices appear to breakdown and the trailing-edge vortex is shed into the wake. For this relatively moderate-amplitude high-frequency heaving motion, the arch-vortex remains over the wing well into the next plunging cycle. For instance, in Figure 39d, the arch vortex is still located near the mid-chord and does not reach the trailing edge until the initiation of the subsequent upstroke (Figure 39h).

Figure 40 compares the evolution of the leading-edge vortex at Sr_c = 0.8 for various wing planforms. The effect on the elliptical wing with b/c = 2 is interesting, the leading edge vortex undergoes a remarkable transformation, developing a distinct undulation (see phase c). This strong undulation encountered on the elliptical wing also occurs for the rectangular wing at some other Strouhal numbers [47,48]. These examples demonstrate that the three-dimensional vortical structures are quite complex. Figure 41 reveals the progression of the undulation for both the elliptical and rectangular wing at Sr_c = 0.75 by presenting the vortex core locations, using the Q-criterion as a core identification tool. Twelve phases in the cycle are used to observe the progression of the undulation with time. Apparently, the undulation exists quite early on in the cycle. Initially close to the tip of the wing, but as the cycle progresses, the undulation both amplifies and travels inboard. It is interesting to note that the undulation appears far more prominent for the rectangular wing. Its overall shape is also highly sensitive to Strouhal number.

Figure 42 shows the vortical structures at higher Strouhal numbers of Sr_c = 1.0-1.35 for flat-plate wings. The higher Strouhal numbers appear to dampen any strong undulations across the span of the wings. We observe instead that the LEV anchor point remains quite close to the tip, and moves further away from the surface further inboard of the wing. The considerable vertical movement is consistent with a reduction in lift performance at the higher Strouhal numbers. A sudden dissipation of the leading edge vortex is observed near the root with increasing Strouhal number. (This is similar to the flat-plate airfoil case shown in Figure 32 and discussed in more detail). It is apparent that the breakdown of the leading edge vortex is dependent on the spanwise position. Whilst, the leading edge vortex is pinned to the surface of the wing, it remains largely coherent closer to the tip, but loses coherency inboard.

Finally, we point out the formation of unusual vortex rings for flows with high Strouhal number. Both upper surface and lower surface tip vortices are generated at high Strouhal numbers due to the higher effective angles of attack. Figure 43 show that these tip vortices form a vortex ring. Although the iso-surfaces represent a constant Q-criterion value, colour maps have been superimposed to illustrate any variation in the streamwise component of vorticity, ω_x. In this way tip vortices formed during the downstroke and upstroke can be differentiated. In Figure 43, it is evident that the vortex ring consists of an interaction between lower and upper surface tip vortices. The comparison at various Strouhal numbers suggests that the phenomenon is associated with high Strouhal numbers. This vortex ring induces velocity in the spanwise (and outboard) direction. It should be noted that in the previous work on pitching wings at high Strouhal number, wake vortices have been observed to undergo spanwise compression [52,53], for which tip vortices have an induced velocity directed towards the symmetry plane of the wing. The tip vortices described here seem to differ significantly from these studies.

3.2.3. Bifurcated / Asymmetric Flows

A further consequence of using a finite wing is that the bifurcated / asymmetric wakes discussed in the two-dimensional case (Section 3.1.3) have not been observed for finite wings for the same conditions (Strouhal number and amplitude) [57]. Shown in Figure 44 is a comparison of the time-averaged lift for a ‘2D’ NACA 0012 airfoil and a ‘3D’ sAR = 3 finite NACA 0012 wing. The results for the airfoil demonstrate a clear bifurcation resulting in two modes as previously discussed. The finite wing however demonstrates a single mode with approximately zero time-averaged lift which would indicate that deflected jets have been prevented. It is worth noting that this is exactly the same wing and experimental setup with the only change being the removal of the tip end-plate. To investigate the effect of this tip endplate, experiments were performed where the proximity of the tip endplate was varied, see Figure 45. The transition from dual-mode to single mode is surprisingly abrupt, within 0.25c (see Figure 45b). As will be shown later there are two possible effects of the tip end-plate that could explain this abrupt transition: firstly it inhibits the tip vortex and secondly it creates vortex cylinders instead of vortex rings. Either of these effects could be significant in causing the change from dual mode to single mode.

Figure 46a shows the time-averaged flow field for the 2D airfoil and Figure 46b for the 3D finite wing. For the 2D airfoil there are clear deflected jets as previously discussed; for the finite wing the jet is aligned with the horizontal. Similar measurements have also been performed, not presented here, for far higher Strouhal numbers of up to $Sr_c = 4.050$ which show the same symmetric time-averaged flow field for the finite wing. Hence the finite wing prevents / inhibits deflected jets.

Shown in Figures 47 and 48 are volumetric velocimetry measurements from a top and side perspective. The left column is for the 2D airfoil; the right column the 3D finite wing. Each row represents a different phase, either: top, middle-down, bottom or middle-up. For the 2D airfoil case the flow field shows clear deflected jets, see Figure 48. The trailing-edge vortices are highly two-dimensional, forming cylinders with the only three-dimensional feature being a very small branch between the two vortices at the tip end-plate. This branch is very weak in comparison with the TEVs and is possibly a junction vortex created by the interaction of the TEV pair with the tip end-plate. Conversely the 3D finite wing is a highly three-dimensional flow field. Near the root the TEVs form cylinders but at a spanwise location these cylinders break into a double helix structure with two branches. One branch goes downstream to connect with the last vortex; one branch goes upstream to connect with the next vortex. There is therefore a long ‘daisy chain’ of interconnected TEVs forming a long series of vortex loops / rings. The point at which this double helix structure forms appears to move inboard as the TEVs propagate downstream. In addition, there is also a strong tip vortex.

From analysis of these and further results [57] it is suggested that there are two possible causes of the prevention of deflected jets in finite wing cases: the tip vortex or vortex rings. It is possible that the tip vortex may prevent deflected jets by acting as an anchor point for the forming TEVs, effectively enforcing a boundary condition that prevents vortex pairing. This is based on observations of the 2D case. In Figure 22 it can be observed that one of the defining characteristics in determining the onset of symmetry breaking is the location of the TEVs and therefore the timing of their shedding. For example, in the pre-bifurcation case (left column) shown in Figure 22 the TEVs in the wake are equidistantly spaced in the x-direction. As observed by Godoy-Diana *et al.*[34,35] symmetry breaking occurs when this equidistant spacing is broken leading to one vortex moves closer to another. This vortex pairing can occur in one of two ways, either the clockwise vortex moves to the counter-clockwise vortex or the counter-clockwise vortex moves to the clockwise vortex which gives the two possible modes / directions. For a finite wing it is possible the tip vortex enforces a time-shedding constraint that prevents TEV movement in the x-direction. The second possible explanation is the vortex rings in the wake. One of the central observations in the 2D case is that deflected jets are characterized by an asymmetry in the TEV strength as defined by the asymmetry parameter, see Figures 27 and 28. This asymmetry in TEV strength was observed for all cases studied. For the vortex rings observed over the finite wing in Figures 47 and 48 this asymmetry cannot be supported according to Helmholtz's first theorem. Indeed the measured values were $\Gamma/U_\infty c$ = 4.15 and 4.16 for the counter-clockwise and clockwise TEVs. This prevention of TEV asymmetry is quite a strong explanation but is based on the tenet that deflected jets cannot exist without asymmetry in TEV strength.

3.3. Lift enhancement of oscillating flexible wings

3.3.1. High Aspect Ratio Wing

In this section the aerodynamics and fluid-structure interactions of flexible rectangular wings of aspect ratio: *sAR* = 3 which are clamped at the root and subjected to a harmonic plunging motion are considered [58]. As flow control and lift enhancement were the main objectives, post-stall angles of attack and small amplitude excitation at the root are considered. For simplicity, wings with flat-plate cross-section are considered. An example is shown in Figure 49 for three wings with different flexibility at an angle of attack of 15°. It is seen that, up to $Sr_c \approx 0.8$, the time-averaged lift coefficients are the same for all wings. However, after this point the lift curves start to diverge. For the "highly flexible" wing, there is substantial lift enhancement compared to the rigid wing, which seems to increase with increasing Strouhal number. It appears that there is no optimal Strouhal number. For this wing, the natural frequency of the first bending mode was measured as $Sr_c = 1.5$ in still fluid in the absence of free-stream flow. At the natural frequency, the lift coefficient of this wing is more than the double of that of the rigid wing. Therefore, detailed measurements of the wing deformation and phase-averaged flow were made at this Strouhal number, $Sr_c = 1.5$, which is also in the realistic range for micro air vehicle applications as shown in Figure 1.

The deformation of this wing is mostly in the bending mode with negligible twist. As the spanwise flexibility is dominant, the deformation of the wing tip is important to characterize the fluid-structure interaction. Figure 50 shows the variation of the amplitude ratio and phase angle of the wing tip as a function of Strouhal number. The tip amplitude increases with increasing frequency, revealing a local maximum around $Sr_c \approx 1.3$. The phase angle (with respect to the root) increases with increasing frequency. At the natural frequency ($Sr_c = 1.5$), the tip amplitude is 1.84 times the value at the root, and the phase angle is around 90°. This phase lag is similar to that found for maximum lift for a flexible plate tilted to horizontal and plunging at zero free-stream velocity [59].

These characteristics of the fluid-structure interaction are similar to those of a system with damping. The wing shape during the plunging cycle is represented in Figure 51. The mid-chord position is plotted as a function of the spanwise direction at different phases in the cycle. The solid lines are for the root moving downwards and dashed lines are for the root moving upwards. When moving down the wing tends to be deformed upwards, and when moving up the wing tends to be deformed downwards. This indicates that the tip motion lags behind the root motion.

Figure 52 and 53 show the volumetric velocity measurements for the rigid and “highly flexible” wing at this Strouhal number. Iso-surfaces of the phase-averaged vorticity magnitude overlaid with spanwise vorticity reveal that the rigid wing experiences LEV dipole formation (similar to the case of the flat-plate airfoil in Figure 32), whilst the flexible wing experiences a stronger convected LEV and tip vortex. While the LEV dipole for the rigid wing dissipates very quickly and does not contribute much to the lift, the much stronger LEV and tip vortex explain the significantly higher lift. Hence, the flexibility inhibits LEV dipole formation, resulting in a stronger convected LEV and stronger tip vortex, which contributes to lift [60].

3.3.2. Low Aspect Ratio Wing

For a smaller, more realistic, aspect ratio of *sAR* = 1.5 similar results to the high aspect ratio case are observed [61]. Shown in Figure 54 is the change (relative to Sr_c = 0) in time-averaged lift coefficient for the rigid and flexible wings oscillating with an amplitude of a/c = 0.15 and α = 15°. For the rigid (mild steel) case, initially lift coefficient increases with local maxima at Sr_c = 0.450 and 0.825. These peaks are similar to those previously been observed for two-dimensional and finite plunging wings that were attributed to resonance with the natural shedding frequency, its harmonics and subharmonics. After Sr_c = 0.825 the lift improvement deteriorates becoming negative for Sr_c > 1.85. Flexibility improves the lift performance for all cases. The maximum recorded is ΔC_l = 1.97 for the PTFE wing at Sr_c = 1.80. This is significantly larger than the maximum for the rigid wing of ΔC_l = 0.64 at Sr_c = 0.825. The flexible wings still demonstrate the Sr_c = 0.45 peak, however the latter peak is not apparent for all cases. There is the suggestion of several peaks for the polypropylene wing at Sr_c = 0.825, 1.275 and 1.650 however these are within the bounds of experimental uncertainty. The PTFE wing was selected for further measurements due to its optimal performance.

Shown in Figure 55 is the tip amplitude ratio (solid line) and tip phase lag (dashed line) against Strouhal number for the PTFE wing. Initially the amplitude ratio consistently increases reaching a maximum at Sr_c = 1.125 of a_{tip}/a_{root} = 1.70, and then decaying after. The tip phase lag consistently increases. For this wing the natural frequency was measured as $Sr_c = 1.54 \pm 0.15$. This is larger than the frequency corresponding to peak tip amplitude; however one would expect this behaviour in a system with damping. The tip phase-lag of 90° at $Sr_c \approx 1.43$ does however lie within the uncertainty range for the natural frequency, demonstrating a result similar to the higher aspect ratio flexible wing.

Shown in Figure 56 are isosurfaces of phase-averaged vorticity for the rigid wing for twelve phases in the cycle. These isosurfaces are colored by contours of spanwise vorticity. Blue therefore represents clockwise rotation (looking from the tip towards the root), and red counter-clockwise rotation. The phases are in a loop starting with the top of the motion (t/T = 0/12) at the top moving down through the left column to the bottom of the motion (t/T = 6/12) before moving back up through the right column to reset the motion to the top. For the rigid wing, the root and tip move in-phase. Starting with the top of the motion (t/T = 0/12), in the wake are the remnants of the trailing-edge and tip vortices from the previous cycle. Likewise there is a region of clockwise vorticity near the leading-edge which is the remnants of a previous LEV, and below the tip are remnants of the previous tip vortex. This tip vortex is coloured green because there is minimal rotation around the z-axis. As the wing begins to move downwards (t/T = 1/12 to 3/12) these remnants convect downstream and lose their coherency. In addition a new TEV and tip vortex form and grow in strength. More interestingly a very strong LEV forms very rapidly and appears to detach from the wing by t/T = 3/12. For t/T = 2/12 to 6/12 a vortex ring is observed linking the primary clockwise LEV with the counter-clockwise upper-surface LEV from the previous cycle. This vortex loop encircles the primary LEV drawing it upstream and away from the airfoil surface. This vortex loop is more clearly demonstrated from an upstream perspective in Figure 57. Considering only the near root flow this behaviour is very similar to the LEV dipole previously observed for an infinite flat plate wing. However, in this case the behavior is complicated by the three-dimensional nature of a finite wing which necessitates the dipole to close on itself. Nevertheless the result is the same, an upper surface LEV that pairs with the lower surface LEV to form a dipole that convects upstream and away from the upper surface resulting in low lift.

Shown in Figure 58 are isosurfaces for the PTFE wing. The higher values of isosurface level in this case are necessary due to the generally higher levels of vorticity. In this case the tip lags the root by 98°. The root therefore reaches the extremes of its motion at t/T = 0/12 and 6/12; whereas the tip reaches the extremes of its motion at approximately t/T = 3/12 and 9/12. At the top of the root motion (t/T = 0/12) there is still a strong LEV form the previous cycle close to the upper surface. Comparing just this phase with the equivalent in Figure 56 the difference in LEV behaviour is very apparent. For the flexible wing there is a strong coherent LEV which convects close to the upper surface. This LEV connects with the lower surface tip vortex, note that until $t/T \approx 3/12$ the tip is still moving upwards. As the root moves downwards (t/T = 1/12 to 3/12) the LEV convects downstream and a counter-clockwise TEV and clockwise LEV begin to form near the root. The LEV and TEV are only partially captured in the volumetric measurements due to the proximity of the wing. Once the tip reaches the top of its motion (*t/T* = 3/12), the LEV disconnects from the tip vortex and instead closes on the upper surface. Conversely the lower surface tip vortex disconnects from the LEV and instead connects to the upper surface tip vortex that has begun to form due to the downward motion of the tip. During this downward motion the LEV and TEV spread from the root towards the tip (*t/T* = 4/12 to 6/12). Once the root reaches the bottom of its motion, the LEV and TEV are shed from the root but continue to grow further outboard, this is most clearly visible at time: *t/T* = 9/12. In addition the previous lower surface tip vortex continues to wrap itself around the upper surface tip vortex to form a vortex loop (see *t/T* = 8/12). Once the tip reaches the bottom of its motion (*t/T* = 9/12), the LEV and TEV are shed completely. By direct comparison of Figure 56 with Figure 58 it is clear that the flexible wing does not experience a LEV dipole. Instead a strong LEV forms and convects close to the upper surface which coupled with the stronger tip vortex explains the higher lift.

4. Conclusions

For rigid airfoils plunging with small-amplitude, two mechanisms of lift enhancement have been identified: deflected jets and convected LEVs. Deflected jets form at high Strouhal numbers for pre-stall angles of attack. They are caused by pairing of the clockwise and counter-clockwise TEVs to form dipoles. These dipoles are asymmetric in position and strength, and therefore self-advect at an angle to the freestream creating asymmetry in the flow field. This asymmetry can create very large lift coefficients, up to $C_l \approx 6$, even for zero degrees angle of attack. Dual jets do not form at low Strouhal numbers due to insufficient vortex strength, nor at larger incidences due to overwhelming bias for a particular direction. Convected LEVs have been shown to be an effective means of lift enhancement for post-stall angles of attack. At low Strouhal numbers upper-surface LEVs form during the downward motion of the airfoil and then convect over the upper surface creating a low pressure region. As these LEVs are created by the plunging motion, the increase in lift coefficient is approximately proportional to the plunge velocity. This form of flow control is particularly effective when the plunge frequency equals the natural shedding frequency, its harmonics or subharmonics, and continues until high Strouhal numbers when a new mode of LEV behavior is observed. In this new mode the LEV still forms during the downward motion, but remains over the leading-edge and is therefore destroyed through impingement with the upward moving airfoil. Even though this new mode is associated with low lift it does correlate very well with the switch from drag to thrust. Both of these mechanisms are strongly influenced by the choice of airfoil shape. For a flat plate airfoil, instead of stable deflected jets, the deflected jets periodically switch direction resulting in periodic changes in the direction of lift with a large period. Instead of convected LEVs, LEV dipoles form for Strouhal numbers greater than unity. These LEV dipoles propagate upstream and away from the airfoil surface resulting in very low lift.

For finite wings oscillating at post-stall incidence, similar lift-enhancing convected LEVs are observed, however the flow field is more complicated. The LEV anchors towards the tip on the wing's upper surface. The tip vortex acts to drive this anchor point inboard towards the root creating an undulation in the LEV. This effect is most pronounced for the elliptical planform. The degree of lift-enhancement is diminished by decreasing aspect ratio. For certain cases interaction between the upper-surface and lower-surface tip vortex can result in tip vortex rings which expand in the spanwise direction. In addition, the high-lift deflected jets observed for the 2D airfoil are prevented for the finite wing. It is postulated that there are two possible causes: the tip vortex or vortex rings. The tip vortex could enforce a boundary condition which ensures symmetry by preventing premature TEV shedding. Alternatively according to Helmholtz's first theorem the asymmetry in TEV strength that characterizes 2D deflected jets cannot be supported for vortex rings.

For oscillating flexible wings appropriate spanwise flexibility can significantly enhance lift performance. For a Strouhal number of $Sr_c = 1.5$, a $sAR = 3$ flexible wing has a lift coefficient more than twice its rigid counterpart. This improvement is associated with significant spanwise deformation of the wing such that the tip lags the root by 90^0 but with an amplitude 1.84 times larger. In terms of the flow field, the rigid wing exhibits weak vortical structures near the leading-edge, which are essentially the three-dimensional version of the LEV dipole observed for flat plate airfoils. Conversely the flexible wing exhibits a strong convected LEV, strong tip vortex and thus high lift.

References

[1] Mueller, T.J., and DeLaurier, J.D., "Aerodynamics of Small Vehicles," *Annual Review of Fluid Mechanics*, Vol. 35, 2003, pp. 89-111.

[2] Shyy, W., Berg, M., and Ljungqvist, D., "Flapping and Flexible Wings for Biological and Micro Air Vehicles," *Progress in Aerospace Sciences*, Vol. 35, No. 5, 1999, pp. 455-505.

[3] Ho, S., Nassef, H., Pornsinsirirak, N., Tai, Y.C., and Ho, C.M., "Unsteady Aerodynamics and Flow Control for Flapping Wing Flyers," *Progress in Aerospace Sciences*, Vol. 39, No. 8, 2003, pp. 635-681.

[4] Gursul, I., "Vortex Flows on Uavs: Issues and Challenges," *Aeronautical Journal*, Vol. 108, No. 1090, 2004, pp. 597-610.

[5] Seifert, A., Greenblatt, D., and Wygnanski, I.J., "Active Separation Control: An Overview of Reynolds and Mach Numbers Effects," *Aerospace Science and Technology*, Vol. 8, No. 7, 2004, pp. 569-582.

[6] Gursul, I., Wang, Z., and Vardaki, E., "Review of Flow Control Mechanisms of Leading-Edge Vortices," *Progress in Aerospace Sciences*, Vol. 43, No. 7-8, 2007, pp. 246-270.

[7] Raju, R., Mittal, R., and Cattafesta, L., "Dynamics of Airfoil Separation Control Using Zero-Net Mass-Flux Forcing," *AIAA Journal*, Vol. 46, No. 12, 2008, pp. 3103-3115.

[8] Wu, J.Z., Lu, X.Y., Denny, A.G., Fan, M., and Wu, J.M., "Post-Stall Flow Control on an Airfoil by Local Unsteady Forcing," *Journal of Fluid Mechanics*, Vol. 371, 1998, pp. 21-58.

[9] Miranda, S., Vlachos, P.P., Telionis, D.P., and Zeiger, M.D., "Flow Control of a Sharp-Edged Airfoil," *AIAA Journal*, Vol. 43, No. 4, 2005, pp. 716-726.

[10] Glezer, A., Amitay, M., and Honohan, A.M., "Aspects of Low- and High-Frequency Actuation for Aerodynamic Flow Control," *AIAA Journal*, Vol. 43, No. 7, 2005, pp. 1501-1511.

[11] Maxworthy, T., "The Fluid-Dynamics of Insect Flight," *Annual Review of Fluid Mechanics*, Vol. 13, 1981, pp. 329-350.

[12] Triantafyllou, M.S., Triantafyllou, G.S., and Yue, D.K.P., "Hydrodynamics of Fishlike Swimming," *Annual Review of Fluid Mechanics*, Vol. 32, 2000, pp. 33-53.

[13] Azuma, A., *The Biokinetics of Flying and Swimming*, 2nd ed., AIAA, Washington, 2006.

[14] Platzer, M.F., Jones, K.D., Young, J., and Lai, J.C.S., "Flapping-Wing Aerodynamics: Progress and Challenges," *AIAA Journal*, Vol. 46, No. 9, 2008, pp. 2136-2149.

[15] Wootton, R.J., "Support and Deformability in Insect Wings," *Journal of Zoology*, Vol. 193, No. APR, 1981, pp. 447-468.

[16] Steppan, S.J., "Flexural Stiffness Patterns of Butterfly Wings (Papilionoidea)," *Journal of Research on the Lepidoptera*, Vol. 35, 2000, pp. 61-77.

[17] Sunada, S., Zeng, L.J., and Kawachi, K., "The Relationship between Dragonfly Wing Structure and Torsional Deformation," *Journal of Theoretical Biology*, Vol. 193, No. 1, 1998, pp. 39-45.

[18] Vanella, M., Fitzgerald, T., Preidikman, S., Balaras, E., and Balachandran, B., "Influence of Flexibility on the Aerodynamic Performance of a Hovering Wing," *Journal of Experimental Biology*, Vol. 212, No. 1, 2009, pp. 95-105.

[19] Moffat, R.J., "Describing the Uncertainties in Experimental Results," *Experimental Thermal and Fluid Science*, Vol. 1, No. 1, 1988, pp. 3-17.

[20] Heathcote, S. "Flexible Flapping Airfoil Propulsion at Low Reynolds Numbers," Ph.D. Dissertation, Dept of Mechanical Engineering, University of Bath, Bath, 2006.

[21] Frampton, K.D., Goldfarb, M., Monopoli, D., and Cveticanin, D. "Passive Aeroelastic Tailoring for Optimal Flapping Wings". *Fixed and Flapping Wing Aerodynamics for Micro Air Vehicle Applications* Amer Inst Aeronautics & Astronautics, Reston, 2002, pp. 473-482.

[22] Pereira, F., and Gharib, M., "Defocusing Digital Particle Image Velocimetry and the Three-Dimensional Characterization of Two-Phase Flows," *Measurement Science & Technology*, Vol. 13, No. 5, 2002, pp. 683-694.

[23] Baek, S.J., and Lee, S.J., "A New Two-Frame Particle Tracking Algorithm Using Match Probability," *Experiments in Fluids*, Vol. 22, No. 1, 1996, pp. 23-32.

[24] Pereira, F., Stuer, H., Graff, E.C., and Gharib, M., "Two-Frame 3d Particle Tracking," *Measurement Science & Technology*, Vol. 17, No. 7, 2006, pp. 1680-1692.

[25] Visbal, M.R., "High-Fidelity Simulation of Transitional Flows Past a Plunging Airfoil," *AIAA Journal*, Vol. 47, No. 11, 2009, pp. 2685-2697.

[26] Cleaver, D.J., Wang, Z., Gursul, I., and Visbal, M.R., "Lift Enhancement by Means of Small-Amplitude Airfoil Oscillations at Low Reynolds Numbers," *AIAA Journal*, Vol. 49, No. 9, 2011, pp. 2018-2033.

[27] Cleaver, D.J., Wang, Z., and Gursul, I., "Investigation of High-Lift Mechanisms for a Flat-Plate Airfoil Undergoing Small-Amplitude Plunging Oscillations," *AIAA Journal*, Vol. 51, No. 4, 2013, pp. 968-980.

[28] Jones, K.D., Dohring, C.M., and Platzer, M.F., "Experimental and Computational Investigation of the Knoller-Betz Effect," *AIAA Journal*, Vol. 36, No. 7, 1998, pp. 1240-1246.

[29] Lewin, G.C., and Haj-Hariri, H., "Modelling Thrust Generation of a Two-Dimensional Heaving Airfoil in a Viscous Flow," *Journal of Fluid Mechanics*, Vol. 492, 2003, pp. 339-362.

[30] Heathcote, S., and Gursul, I., "Jet Switching Phenomenon for a Periodically Plunging Airfoil," *Physics of Fluids*, Vol. 19, No. 2, 2007.

[31] von Ellenrieder, K.D., and Pothos, S., "PIV Measurements of the Asymmetric Wake of a Two Dimensional Heaving Hydrofoil," *Experiments in Fluids*, Vol. 44, No. 5, 2008, pp. 733-745.

[32] Liang, C.L., Ou, K., Premasuthan, S., Jameson, A., and Wang, Z.J., "High-Order Accurate Simulations of Unsteady Flow Past Plunging and Pitching Airfoils," *Computers & Fluids*, Vol. 40, No. 1, 2011, pp. 236-248.

[33] Emblemsvag, J.E., Suzuki, R., and Candler, G. "Numerical Simulation of Flapping Micro Air Vehicles," *32nd AIAA Fluid Dynamics Meeting*, AIAA Paper 2002-3197, St. Louis, MO; US, 2002.

[34] Godoy-Diana, R., Aider, J.L., and Wesfreid, J.E., "Transitions in the Wake of a Flapping Foil," *Physical Review E*, Vol. 77, No. 1, 2008.

[35] Godoy-Diana, R., Marais, C., Aider, J.L., and Wesfreid, J.E., "A Model for the Symmetry Breaking of the Reverse Benard-Von Karman Vortex Street Produced by a Flapping Foil," *Journal of Fluid Mechanics*, Vol. 622, 2009, pp. 23-32.

[36] Cleaver, D.J., Wang, Z., and Gursul, I., "Bifurcating Flows of Plunging Airfoils at High Strouhal Numbers," *Journal of Fluid Mechanics*, Vol. 708, 2012, pp. 349-376.

[37] Andro, J.Y., and Jacquin, L., "Frequency Effects on the Aerodynamic Mechanisms of a Heaving Airfoil in a Forward Flight Configuration," *Aerospace Science and Technology*, Vol. 13, No. 1, 2009, pp. 71-80.

[38] Young, J., and Lai, J.C.S., "Oscillation Frequency and Amplitude Effects on the Wake of a Plunging Airfoil," *AIAA Journal*, Vol. 42, No. 10, 2004, pp. 2042-2052.

[39] Bearman, P.W., "Vortex Shedding from Oscillating Bluff-Bodies," *Annual Review of Fluid Mechanics*, Vol. 16, 1984, pp. 195-222.

[40] Milne-Thomson, L.M., *Theoretical Hydrodynamics*, 5th ed., The Macmillan Press Ltd, London, 1968.

[41] Mueller, T.J., and DeLaurier, J. "An Overview of Micro Air Vehicle Aerodynamics". *Fixed and Flapping Wing Aerodynamics for Micro Air Vehicle Applications 2001* AIAA, Virginia, 2001,

[42] Calderon, D.E., Wang, Z., and Gursul, I. "Lift Enhancement of a Rectangular Wing Undergoing a Small Amplitude Plunging Motion," *48th AIAA Aerospace Sciences Meeting Including the New Horizons Forum and Aerospace Exposition*, AIAA 2010-386, Orlando, Florida, 2010.

[43] Calderon, D.E., Wang, Z., and Gursul, I. "Effect of Wing Geometry on the Lift of a Plunging Finite Wing," *40th Fluid Dynamics Conference and Exhibit*, AIAA-2010-459, Chicago, Illinois, 2010.

[44] Calderon, D.E., Wang, Z., and Gursul, I., "Lift Enhancing Vortex Flows Generated by Plunging Finite Wing," *AIAA Journal*, in press.

[45] Taira, K., and Colonius, T., "Three-Dimensional Flows around Low-Aspect-Ratio Flat-Plate Wings at Low Reynolds Numbers," *Journal of Fluid Mechanics*, Vol. 623, 2009, pp. 187-207.

[46] Rojratsirikul, P., Genc, M.S., Wang, Z., and Gursul, I., "Flow-Induced Vibrations of Low Aspect Ratio Rectangular Membrane Wings," *Journal of Fluids and Structures*, Vol. 27, No. 8, 2011, pp. 1296-1309.

[47] Calderon, D.E., Wang, Z., and Gursul, I. "Volumetric Measurements and Simulations of the Vortex Structures Generated by Low Aspect Ratio Plunging Wings " *50th AIAA Aerospace Sciences Meeting,* AIAA-2012-914, Nashville, Tennessee, 2012.

[48] Calderon, D.E., Wang, Z., Gursul, I., and Visbal, M.R., "Volumetric Measurements and Simulations of the Vortex Structures Generated by Low Aspect Ratio Plunging Wings," *Physics of Fluids,* Vol. 25, No. 6, 2013.

[49] Freymuth, P., "Visualizing the Connectivity of Vortex Systems for Pitching Wings," *Journal of Fluids Engineering - Transactions of the ASME,* Vol. 111, No. 2, 1989, pp. 217-220.

[50] von Ellenrieder, K.D., Parker, K., and Soria, J., "Flow Structures Behind a Heaving and Pitching Finite-Span Wing," *Journal of Fluid Mechanics*, Vol. 490, 2003, pp. 129-138.

[51] Blondeaux, P., Fornarelli, F., Guglielmini, L., Triantafyllou, M.S., and Verzicco, R., "Numerical Experiments on Flapping Foils Mimicking Fish-Like Locomotion," *Physics of Fluids,* Vol. 17, No. 11, 2005.

[52] Dong, H., Mittal, R., and Najjar, F.M., "Wake Topology and Hydrodynamic Performance of Low-Aspect-Ratio Flapping Foils," *Journal of Fluid Mechanics,* Vol. 566, 2006, pp. 309-343.

[53] Buchholz, J.H.J., and Smits, A.J., "On the Evolution of the Wake Structure Produced by a Low-Aspect-Ratio Pitching Panel," *Journal of Fluid Mechanics*, Vol. 546, 2006, pp. 433-443.

[54] Yilmaz, T.O., and Rockwell, D., "Three-Dimensional Flow Structure on a Maneuvering Wing," *Experiments in Fluids,* Vol. 48, No. 3, 2010, pp. 539-544.

[55] Yilmaz, T.O., and Rockwell, D., "Flow Structure on Finite-Span Wings Due to Pitch-up Motion," *Journal of Fluid Mechanics,* Vol. 691, 2012, pp. 518-545.

[56] Visbal, M., Yilmaz, T.O., and Rockwell, D., "Three-Dimensional Vortex Formation on a Heaving Low-Aspect-Ratio Wing: Computations and Experiments," *Journal of Fluids and Structures*, Vol. 38, No. 0, 2013, pp. 58-76.

[57] Calderon, D.E., Cleaver, D.J., Wang, Z., and Gursul, I. "Wake Structure of Plunging Finite Wings," *43rd AIAA Fluid Dynamics Conference and Exhibit*, AIAA-2013-2993, San Diego, California, 2013.

[58] Cleaver, D.J., Wang, Z., and Gursul, I. "Oscillating Flexible Wings at Low Reynolds Numbers," *51st AIAA Aerospace Sciences Meeting*, AIAA-2013-0674, Grapevine, Texas, 2013.

[59] Masoud, H., and Alexeev, A., "Resonance of Flexible Flapping Wings at Low Reynolds Number," *Physical Review E*, Vol. 81, No. 5, 2010.

[60] Barnes, C.J., Visbal, M., and Gordnier, R.E. "High-Fidelity Simulations of a Flexible, Heaving Finite-Aspect-Ratio Wing," *43rd AIAA Fluid Dynamics Conference*, AIAA-2013-3179, San Diego, CA, 2013.

[61] Cleaver, D.J., Calderon, D.E., Wang, Z., and Gusul, I. "Low Aspect Ratio Oscillating Flexible Wings at Low Reynolds Numbers," *43rd AIAA Fluid Dynamics Conference and Exhibit*, AIAA-2013-3178, San Diego, California, 2013.

List of Publications from this Project

[P1] Gursul, I., Cleaver, D.J., and Wang, Z., "Control of Low Reynolds Number Flows by Means of Fluid-Structure Interactions," *Progress in Aerospace Sciences*, in press.

[P2] Calderon, D.E., Wang, Z., and Gursul, I., "Lift Enhancing Vortex Flows Generated by Plunging Finite Wing," *AIAA Journal*, in press.

[P3] Calderon, D.E., Wang, Z., Gursul, I., and Visbal, M.R., "Volumetric Measurements and Simulations of the Vortex Structures Generated by Low Aspect Ratio Plunging Wings," *Physics of Fluids*, Vol. 25, No. 6, 2013.

[P4] Cleaver, D.J., Wang, Z., and Gursul, I., "Investigation of High-Lift Mechanisms for a Flat-Plate Airfoil Undergoing Small-Amplitude Plunging Oscillations," *AIAA Journal*, Vol. 51, No. 4, 2013, pp. 968-980.

[P5] Tregidgo, L., Wang, Z., and Gursul, I., "Frequency Lock-in Phenomenon for Self-Sustained Roll Oscillations of Rectangular Wings Undergoing a Forced Periodic Pitching Motion," *Physics of Fluids*, Vol. 24, No. 11, 2012.

[P6] Cleaver, D.J., Wang, Z., and Gursul, I., "Bifurcating Flows of Plunging Airfoils at High Strouhal Numbers," *Journal of Fluid Mechanics*, Vol. 708, 2012, pp. 349-376.

[P7] Calderon, D.E., Wang, Z., and Gursul, I., "Three-Dimensional Measurements of Vortex Breakdown," *Experiments in Fluids*, Vol. 53, No. 1, 2012, pp. 293-299.

[P8] Cleaver, D.J., Wang, Z., Gursul, I., and Visbal, M.R., "Lift Enhancement by Means of Small-Amplitude Airfoil Oscillations at Low Reynolds Numbers," *AIAA Journal*, Vol. 49, No. 9, 2011, pp. 2018-2033.

Figures

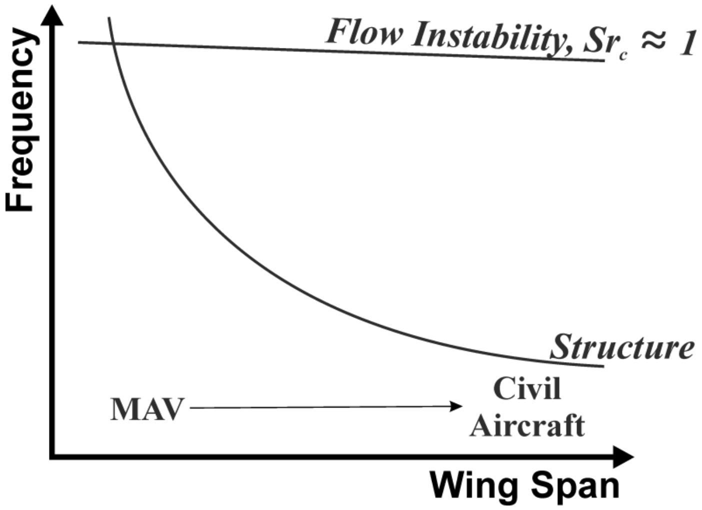

Fig. 1 Schematic variation of natural frequency of flow instabilities and wing structure as a function of wing span. Optimal Strouhal number of the flow instabilities is on the order of unity. The Strouhal number is defined based on the chord length and free stream velocity. Schematic variation of the frequency of flow instabilities is shown after the variations of wing chord and flight speed with wing span are taken into account.

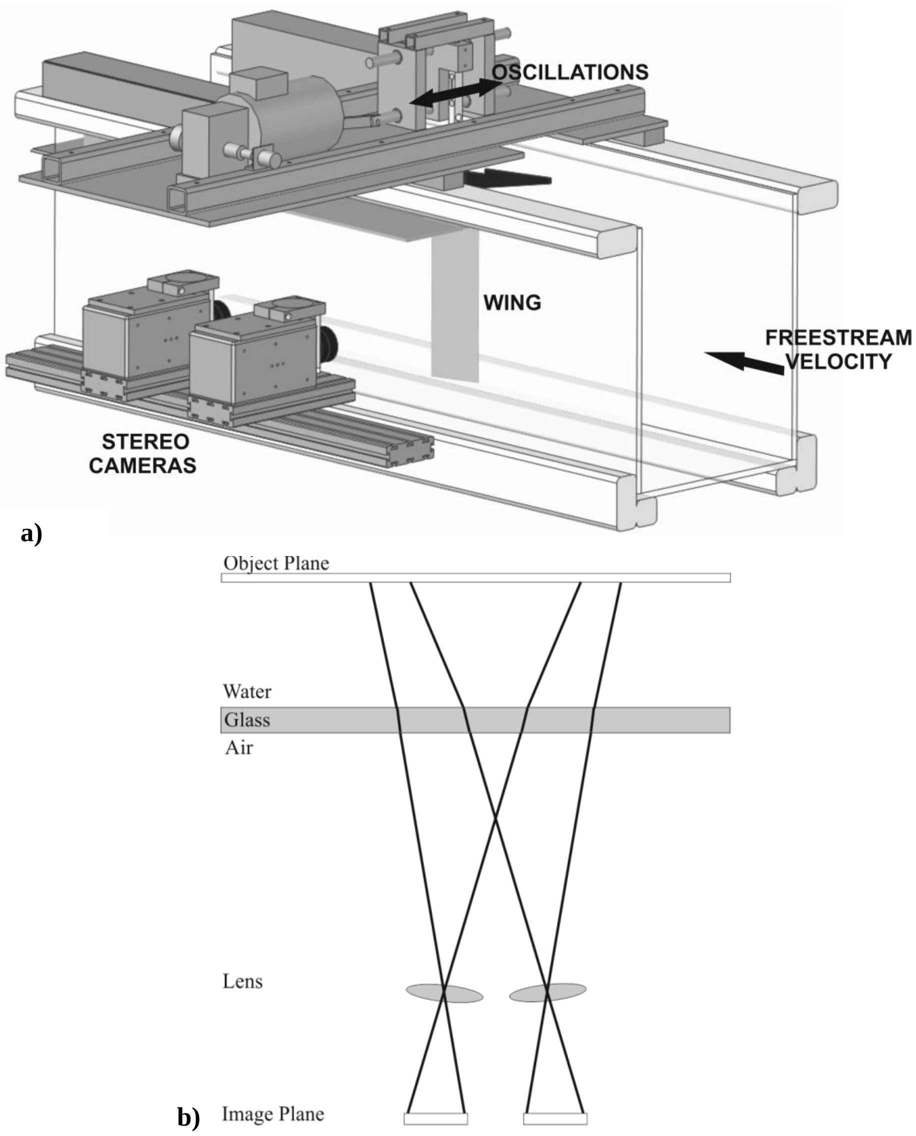

Fig. 2 a) Digital image correlation setup, b) method used to correct for image warping using Scheimpflug mounts. Maximum error was always less than 0.15%c.

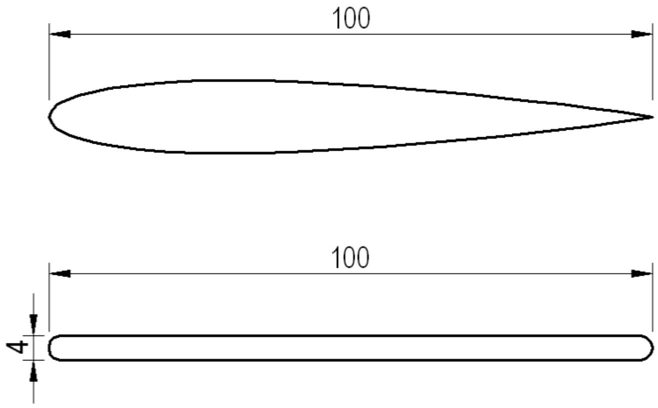

Fig. 3 Wing cross-section showing: NACA 0012 airfoil (top) and flat plate (bottom).

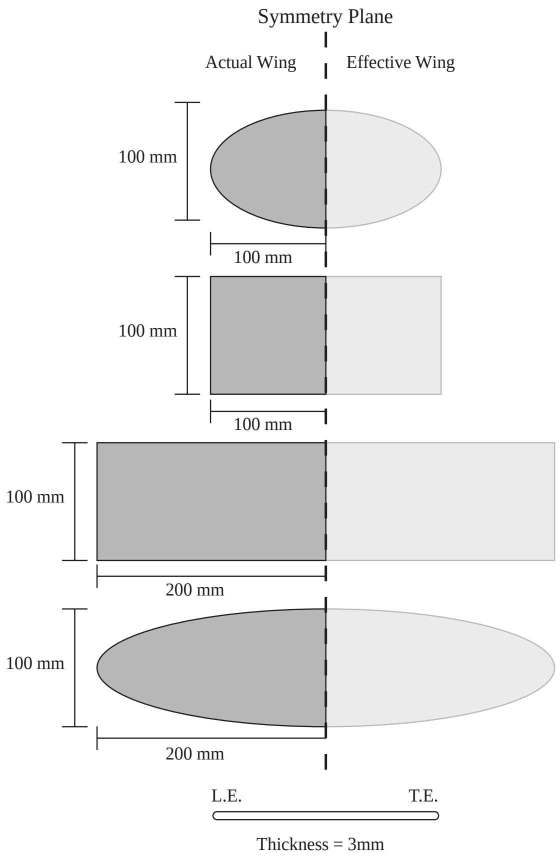

Fig. 4 A comparison between planform shapes and wing profile.

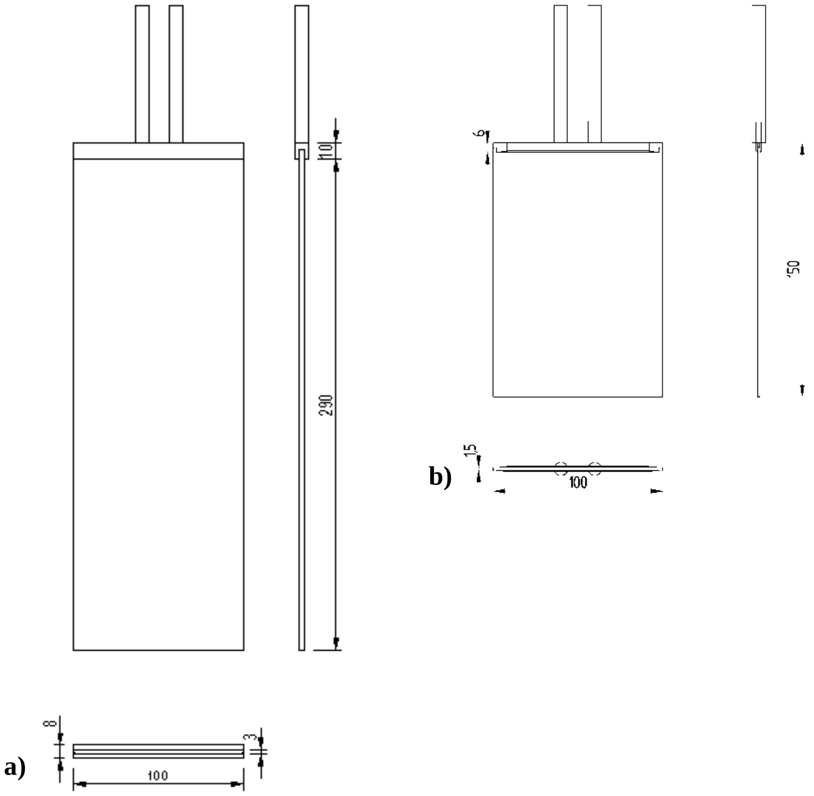

Fig. 5 Flexible wing geometry: a) sAR = 3 and b) sAR = 1.5.

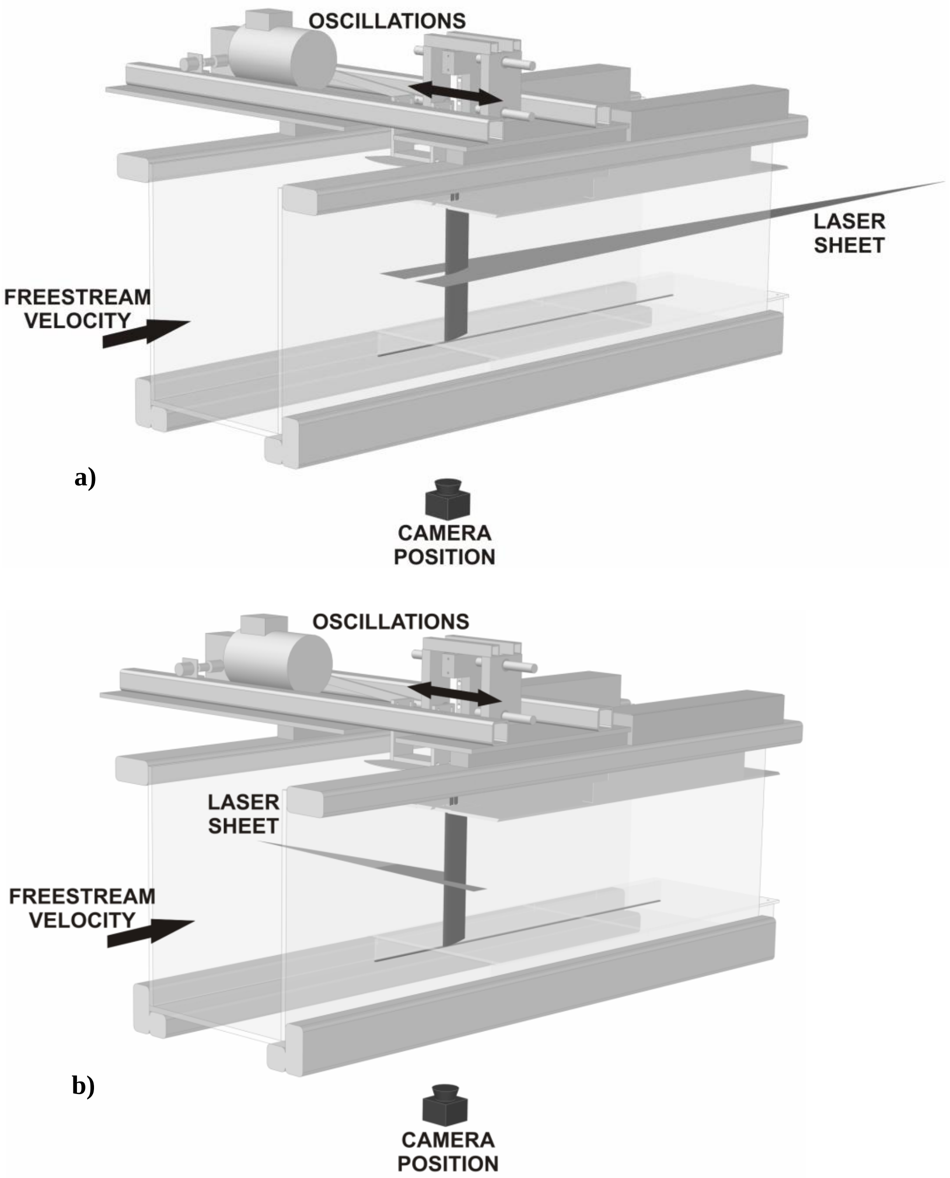

Fig. 6 2D-PIV experimental setup a) for measurements over the upper surface, and b) for measurements over the lower surface.

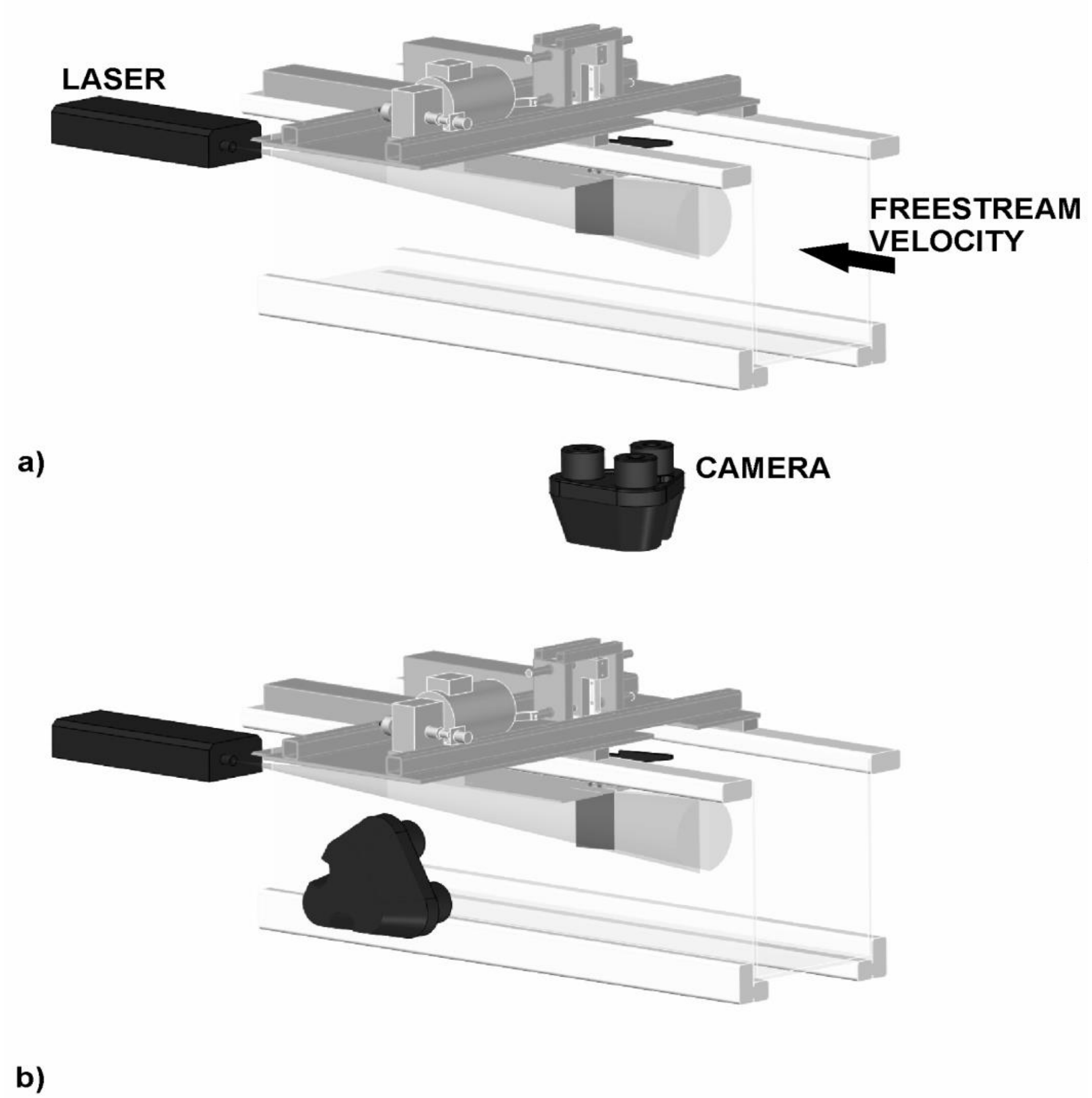

Fig. 7 Volumetric velocimetry experimental setup.

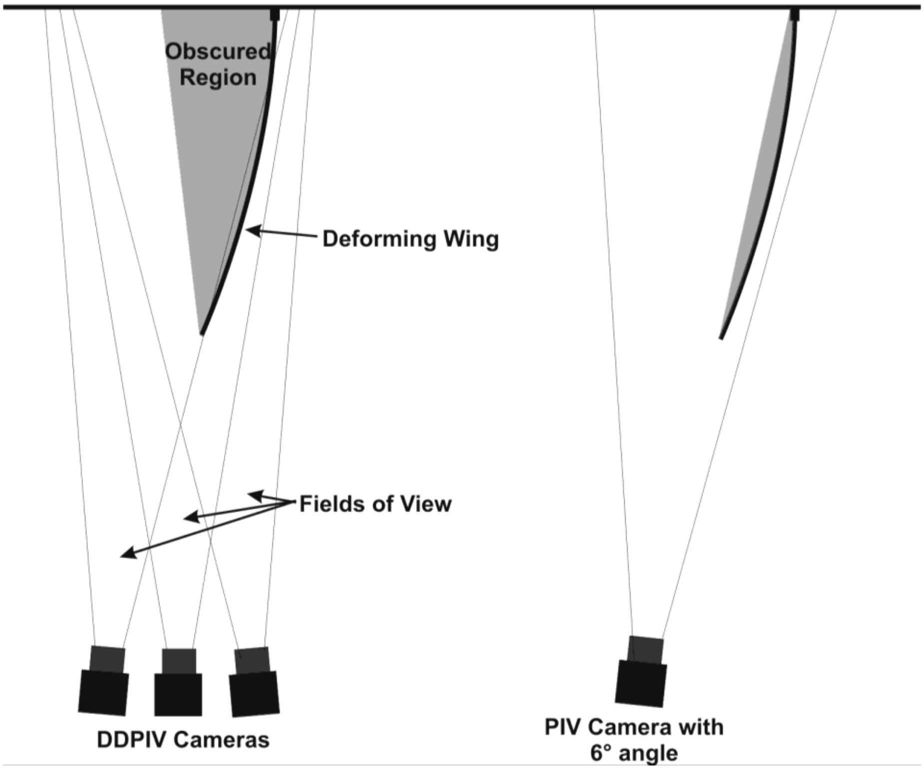

Fig. 8 Visual obstruction for DDPIV measurements (left) and comparison with 2D-PIV measurements (right).

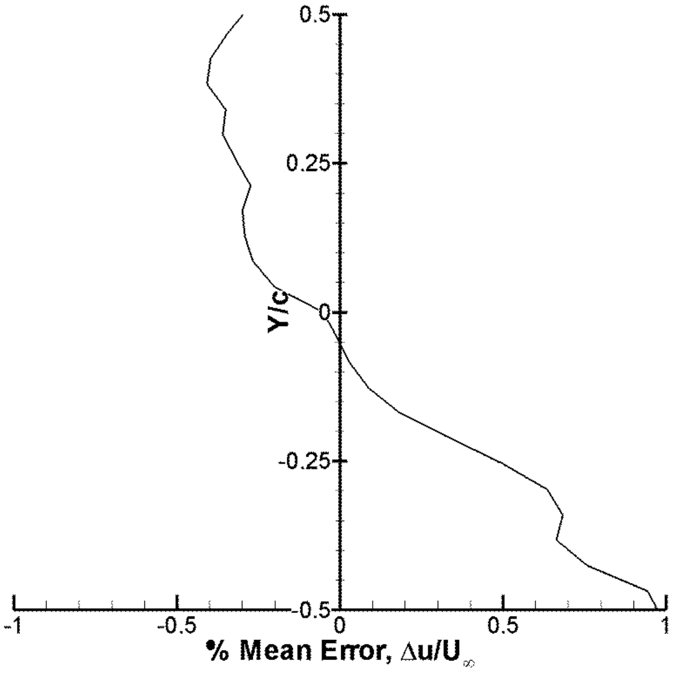

Fig. 9 Measured error due to the 6° 2D-PIV Camera tilt angle. Defined as the mean, along x, of the measured freestream velocity with 6° tilt angle subtracted from the measured freestream velocity with 0° angle.

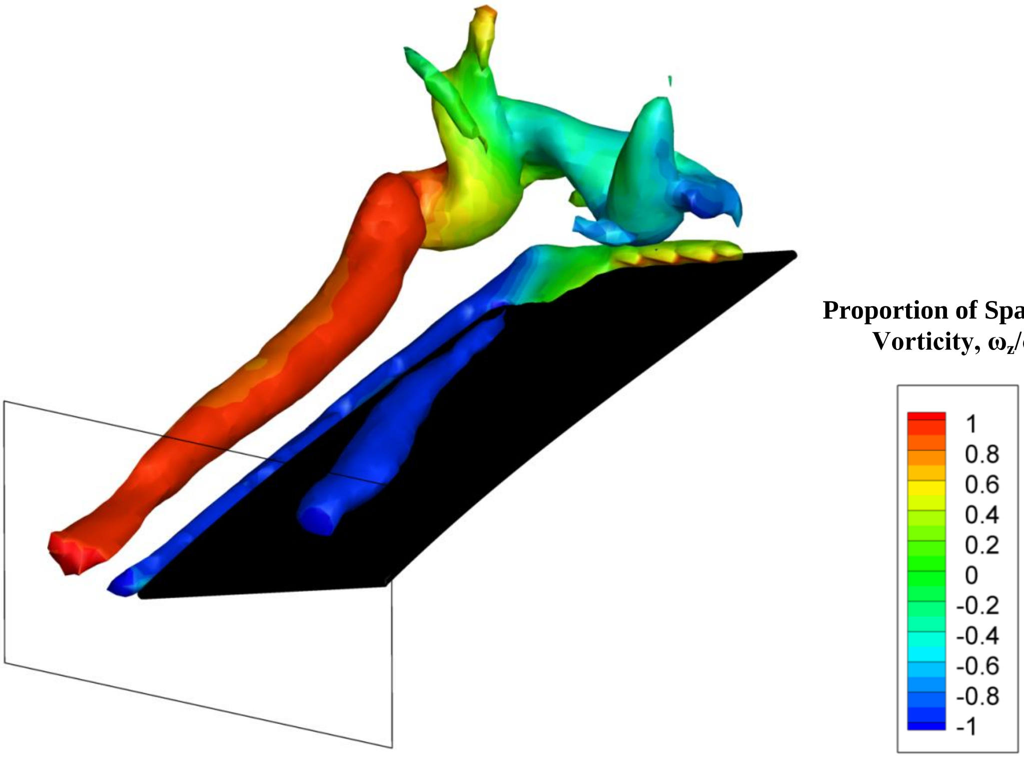

Fig. 10 A single isosurface of phase-averaged (t/T = 0.75) vorticity magnitude ($\omega c/U_\infty$ = 25) acquired using volumetric velocimetry for the highly flexible sAR = 3 wing oscillating with Sr_c = 1.500. Where the isosurface is solid red or blue, spanwise vorticity is the primary contributor to vorticity magnitude.

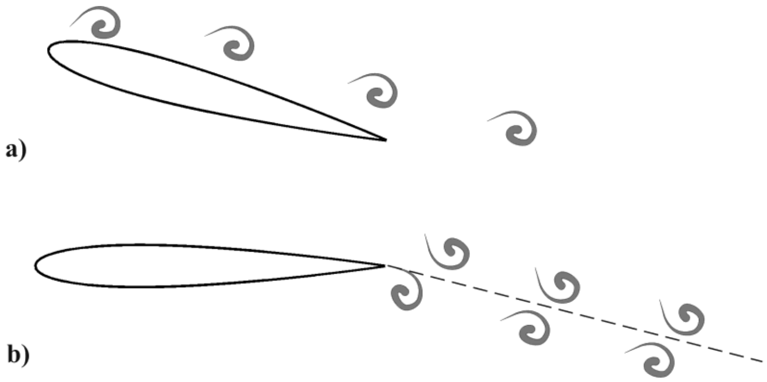

Fig. 11 High-lift mechanisms for an airfoil oscillating with small-amplitude: a) LEV for post-stall angles of attack, and b) deflected jets for pre-stall angles of attack.

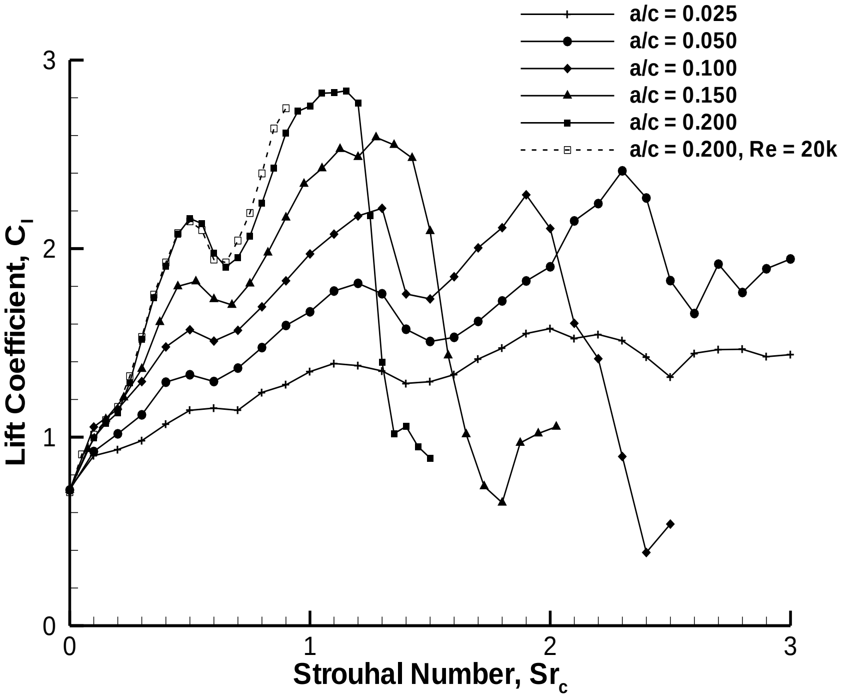

Fig. 12 Time-averaged lift coefficient for a NACA 0012 airfoil for α = 15°, *Re* = 10,000 and different amplitudes.

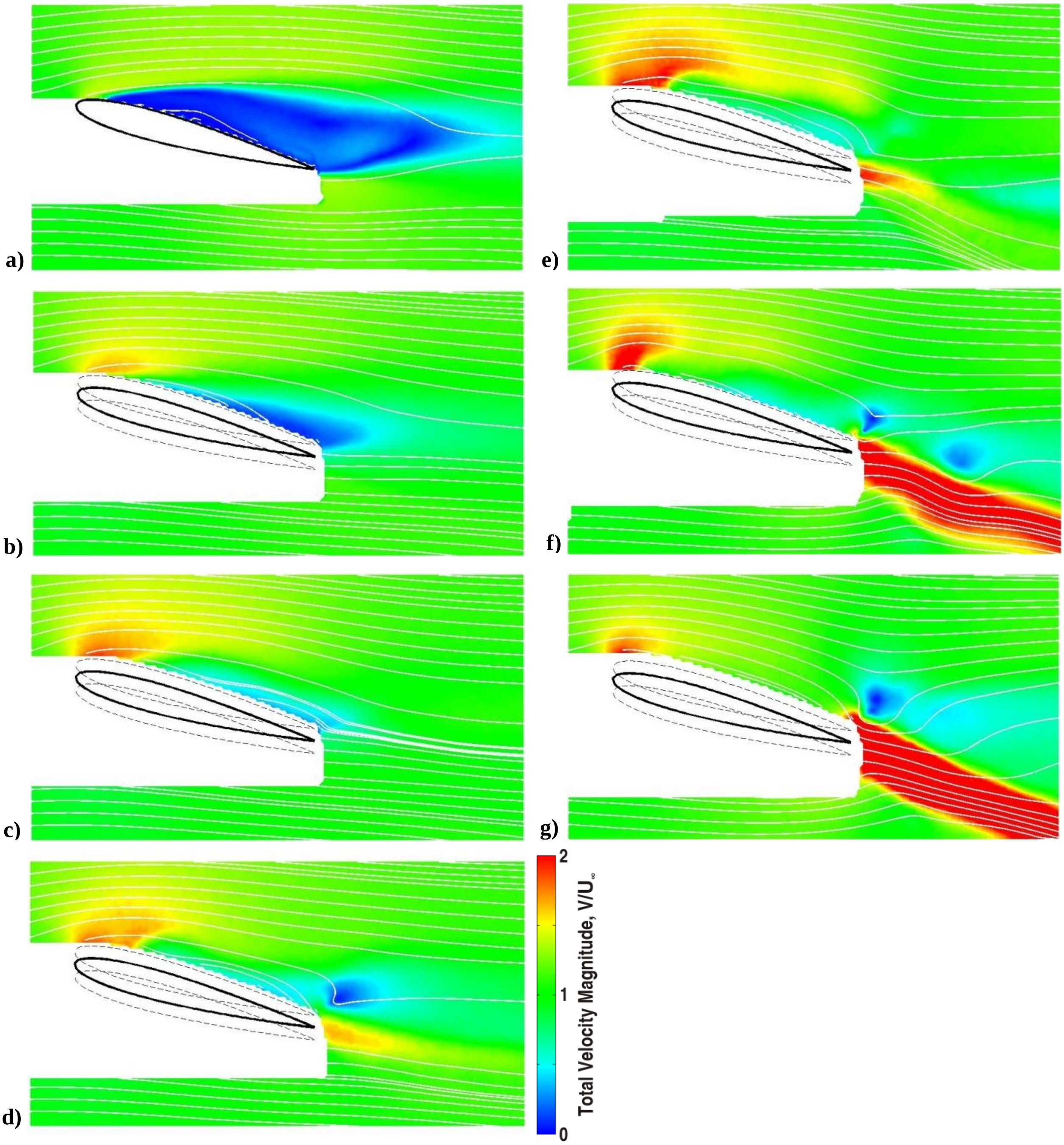

Fig. 13 Magnitude of time-averaged velocity for *a/c* = 0.050: a) stationary; b) Sr_c = 0.5; c) Sr_c = 1.0; d) Sr_c = 1.5; e) Sr_c = 2.0; f) Sr_c = 2.5 and g) Sr_c = 3.0. NACA 0012 airfoil for α = 15°, *Re* = 10,000.

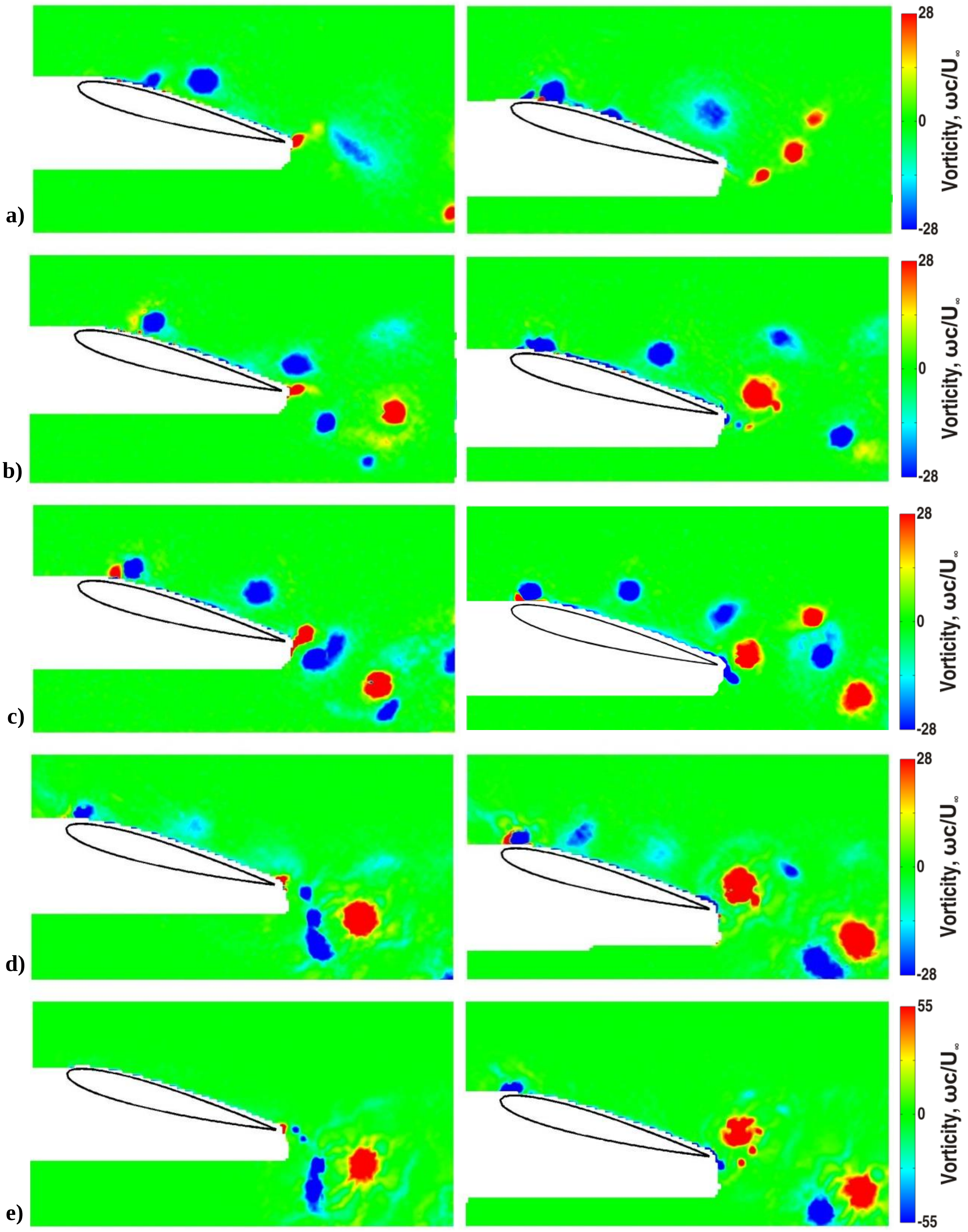

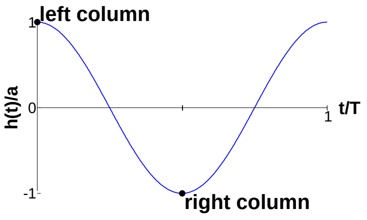

Fig. 14 Phase-averaged vorticity at top (left) and bottom (right) of airfoil displacement for *a/c* = 0.050: a) Sr_c = 1.0; b) Sr_c = 1.5; c) Sr_c = 2.0; d) Sr_c = 2.5; e) Sr_c = 3.0. a) through c) demonstrate mode-1, e) demonstrates mode-2, and d) demonstrates a mixed mode. Note the different scale for e). NACA 0012 airfoil for α = 15°, *Re* = 10,000.

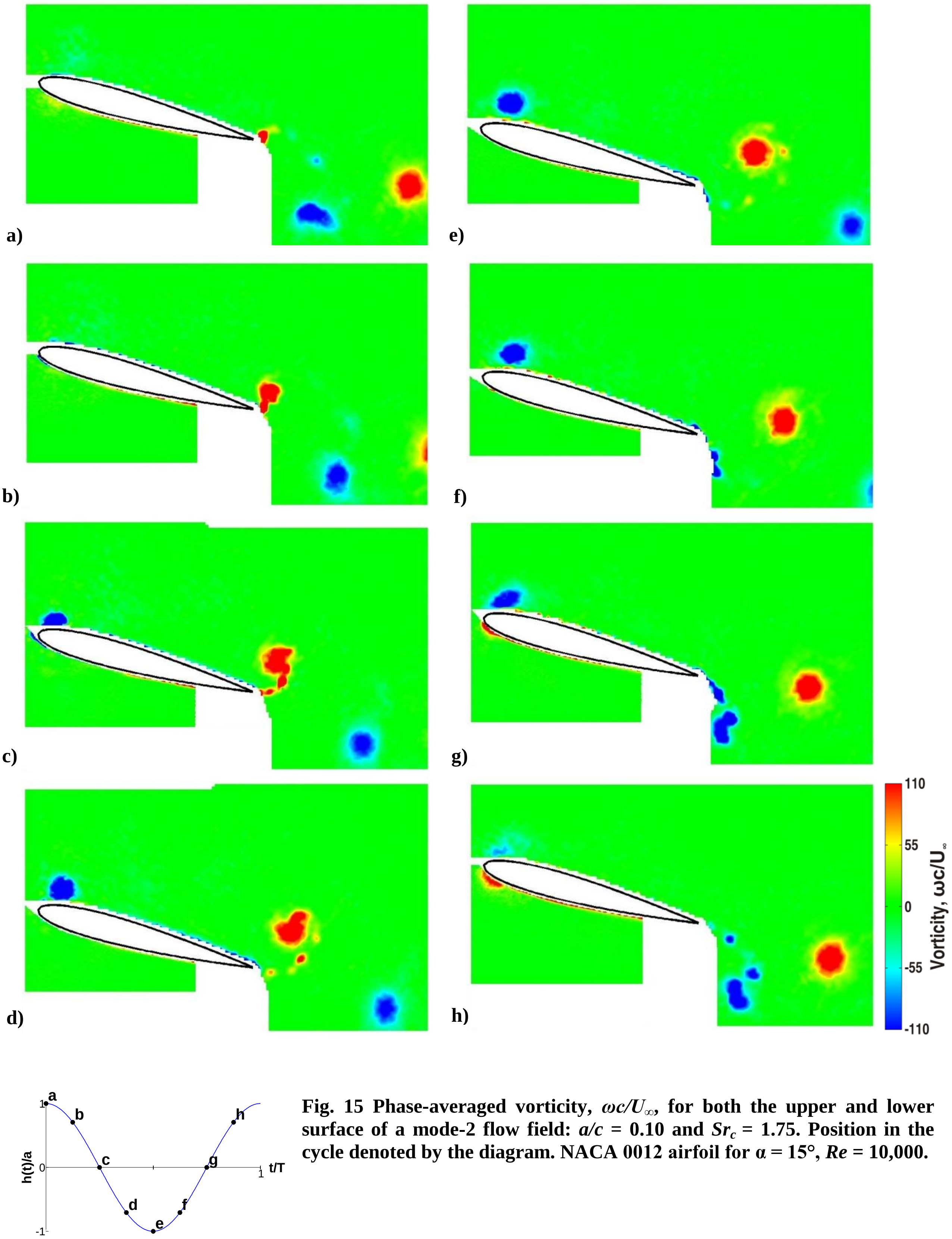

Fig. 15 Phase-averaged vorticity, $\omega c/U_\infty$, for both the upper and lower surface of a mode-2 flow field: $a/c = 0.10$ and $Sr_c = 1.75$. Position in the cycle denoted by the diagram. NACA 0012 airfoil for $\alpha = 15°$, $Re = 10{,}000$.

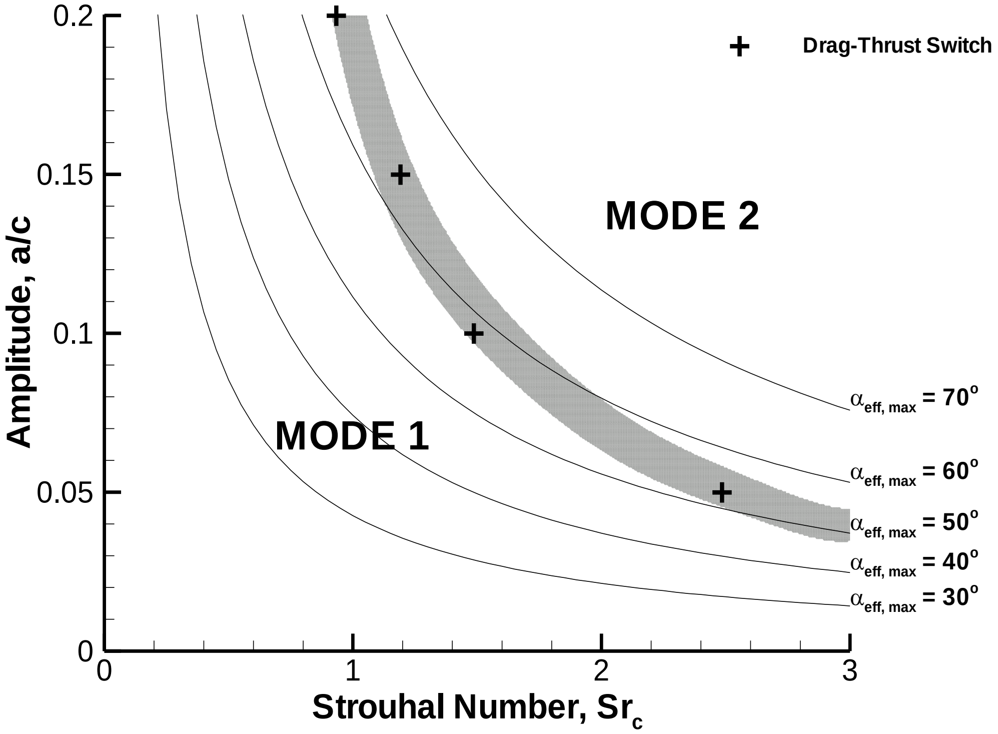

Fig. 16 Mode diagram derived from phase-averaged flow fields measured by PIV. The mode-switch boundary is represented by the shaded area. NACA 0012 airfoil for α = 15°, *Re* = 10,000.

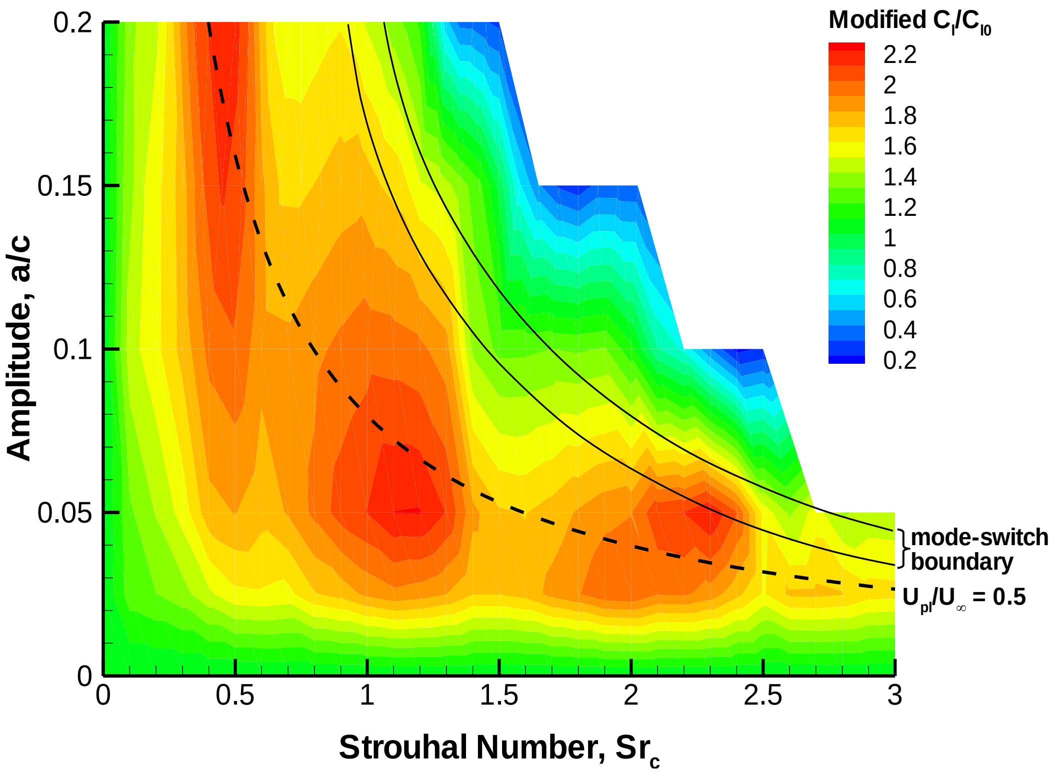

Fig. 17 Contour plot of modified lift coefficient normalized by the value for a stationary airfoil. Solid lines represent the mode-switch boundary from Figure 7. Dashed line represents a constant normalized plunge velocity. NACA 0012 airfoil for α = 15°, *Re* = 10,000.

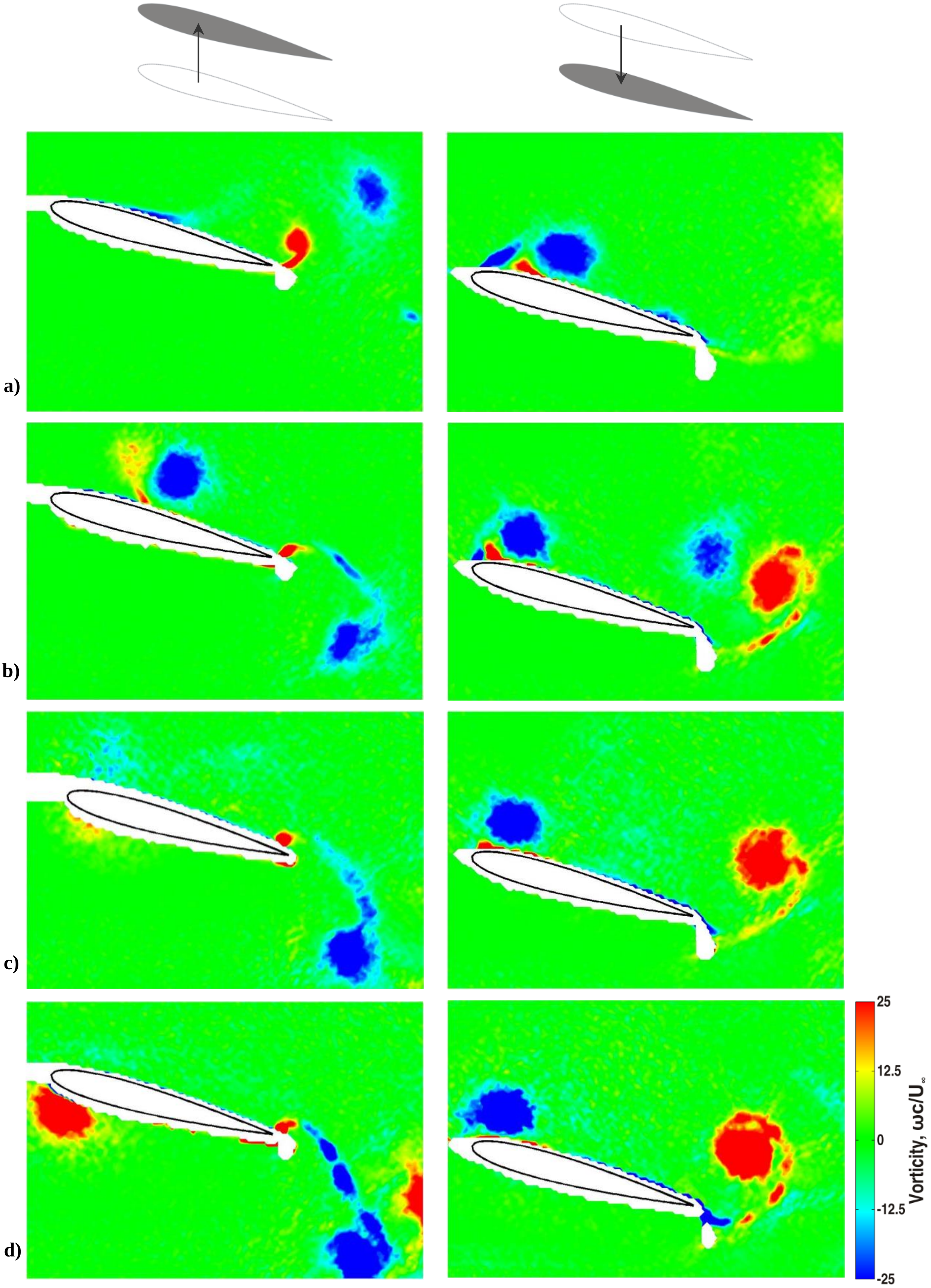

Fig. 18 Normalized vorticity at top (left) and bottom (right) of motion with $a/c = 0.15$, for: a) $Sr_A = 0.15$ ($Sr_c = 0.50$), b) $Sr_A = 0.30$ ($Sr_c = 1.00$), c) $Sr_A = 0.375$ ($Sr_c = 1.25$), d) $Sr_A = 0.525$ ($Sr_c = 1.75$). NACA 0012 airfoil for $\alpha = 15°$, $Re = 10{,}000$.

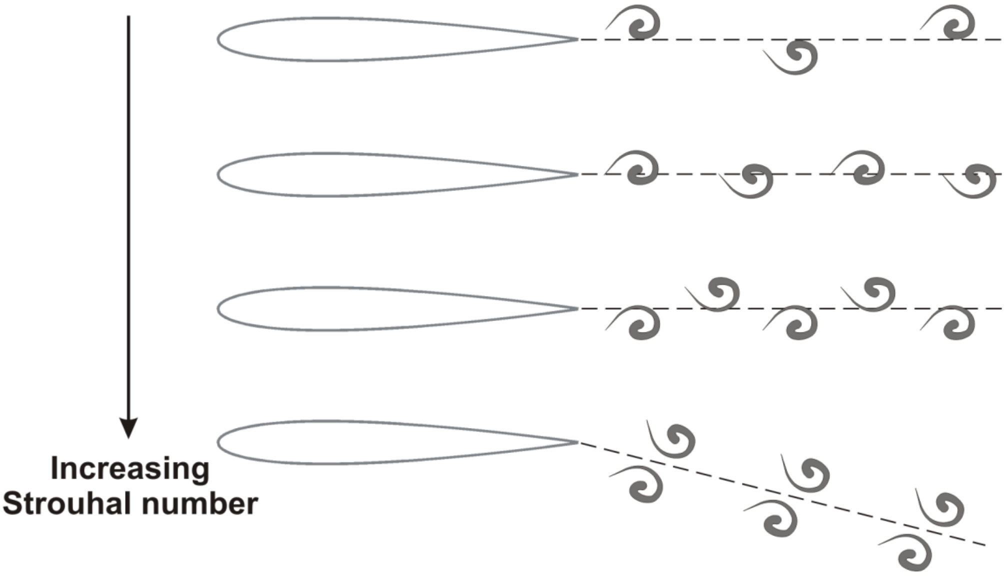

Fig. 19 Wake patterns with increasing Strouhal number.

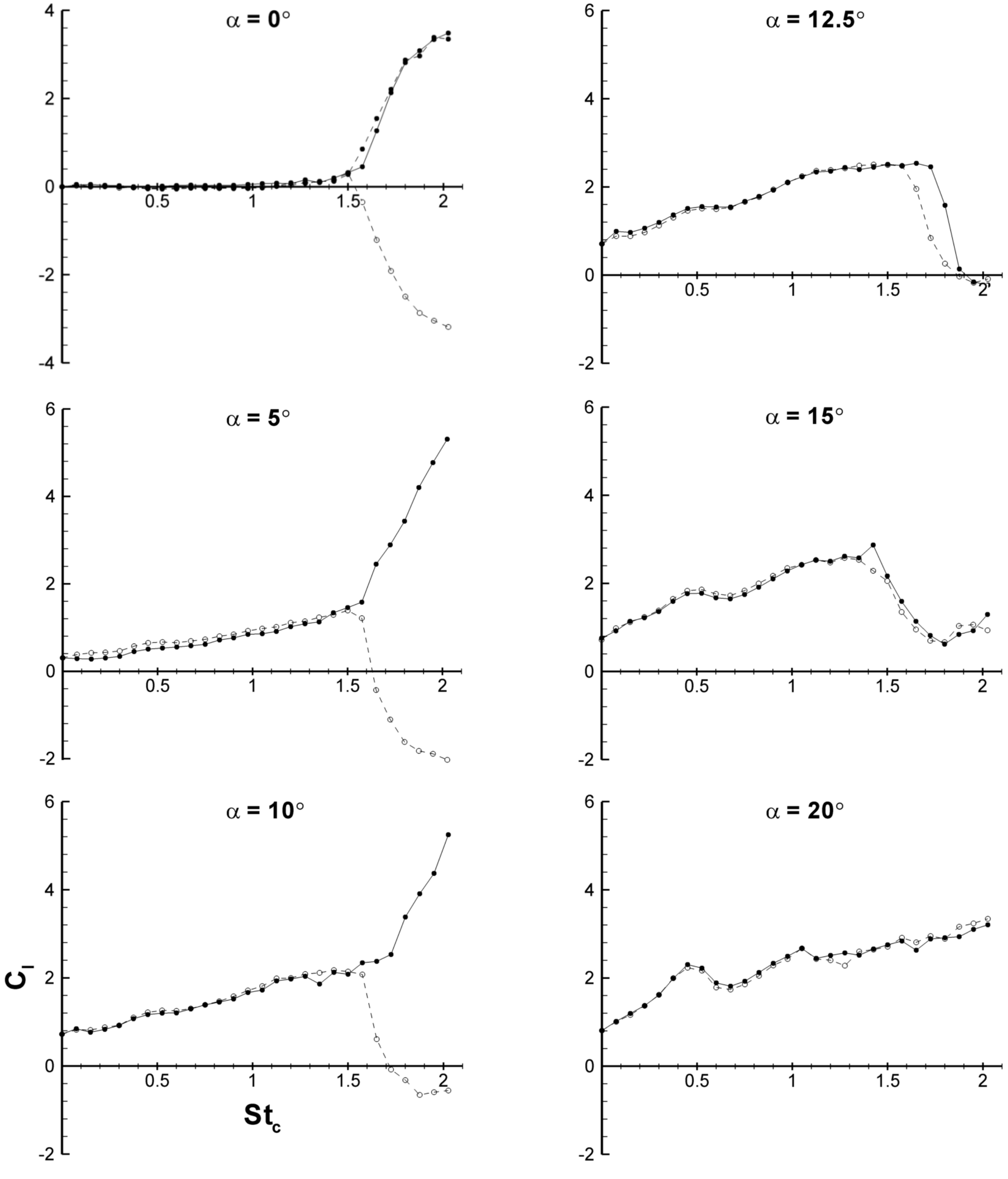

Fig. 20 Time-averaged lift coefficient for *a/c* = 0.15 and all angles of attack considered. Solid line represents increasing frequency, dashed line represents decreasing frequency with a starting position for $\alpha = 0°$ of $h_i = \pm a$, and for $\alpha > 0°$ $h_i = 0$ (airfoil moving upwards). NACA 0012 airfoil, *Re* = 10,000.

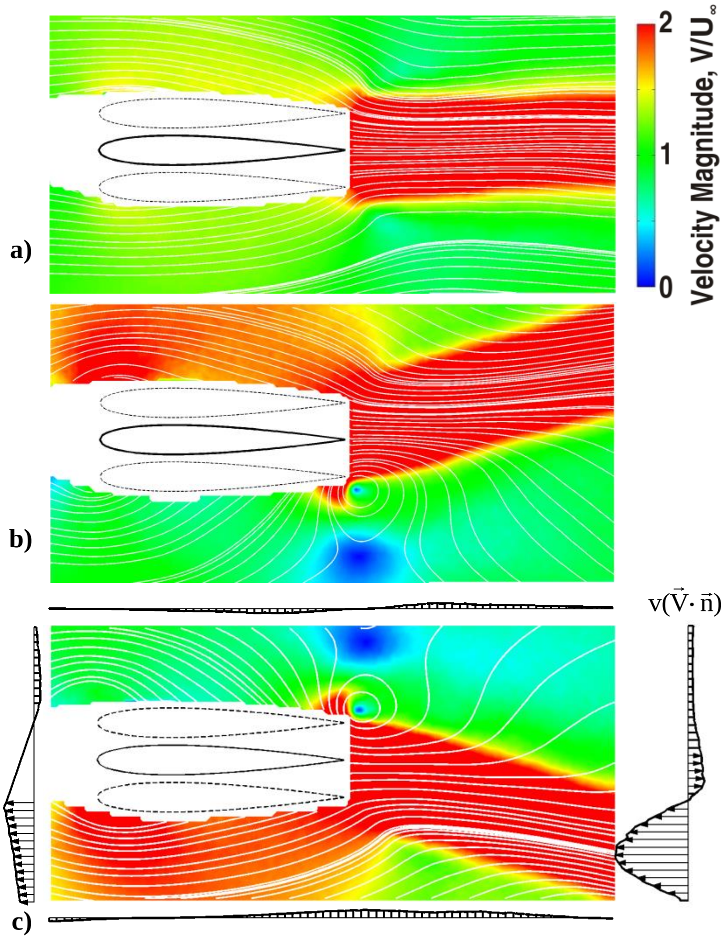

Fig. 21 Time-averaged velocity magnitude for a/c = 0.15, α = 0°, and: a) Sr_c = 1.500 - pre-bifurcation, b) Sr_c = 2.025 – mode A, and c) Sr_c = 2.025 – mode B. For c) arrows show momentum flux component in the vertical direction for the boundaries of the control volume. NACA 0012 airfoil, Re = 10,000.

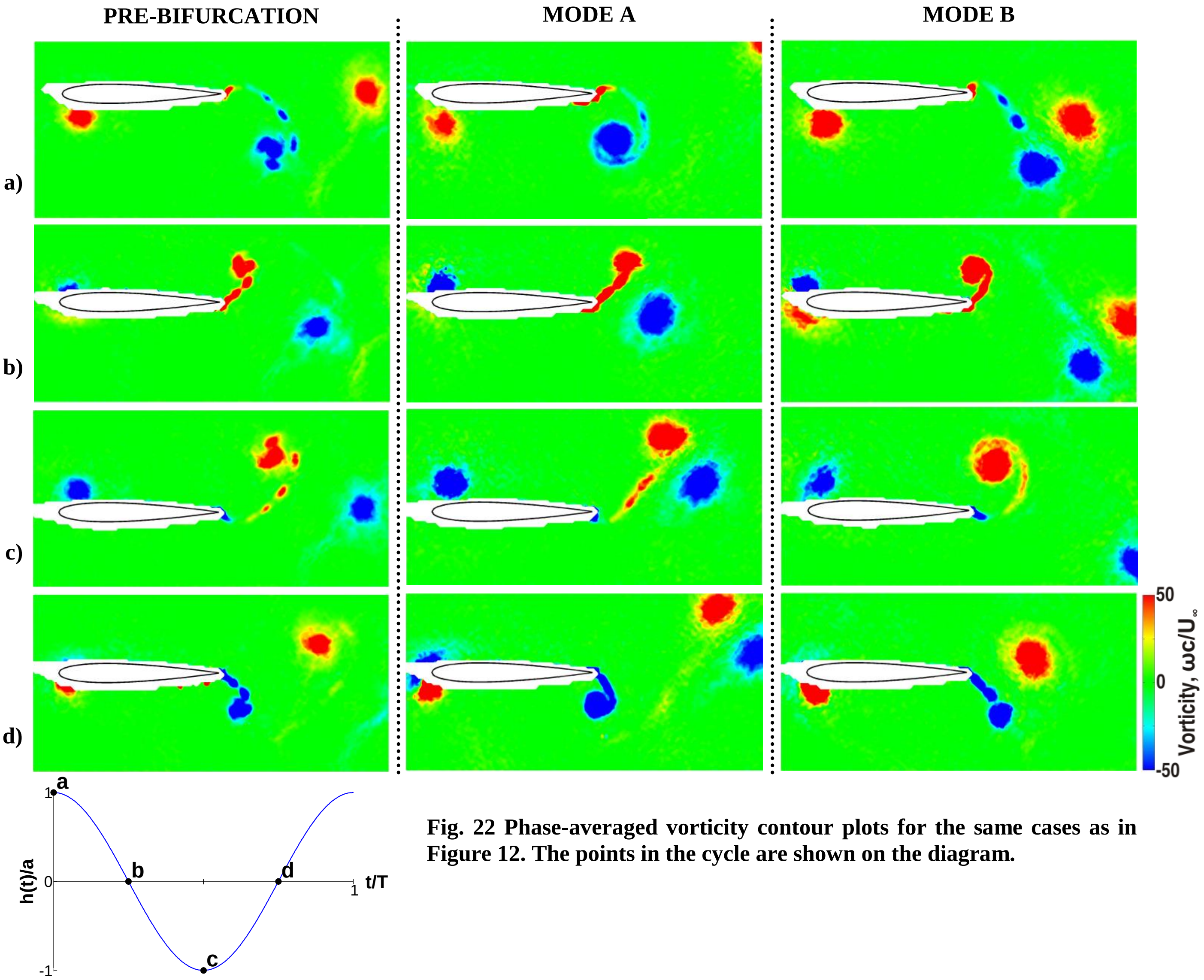

Fig. 22 Phase-averaged vorticity contour plots for the same cases as in Figure 12. The points in the cycle are shown on the diagram.

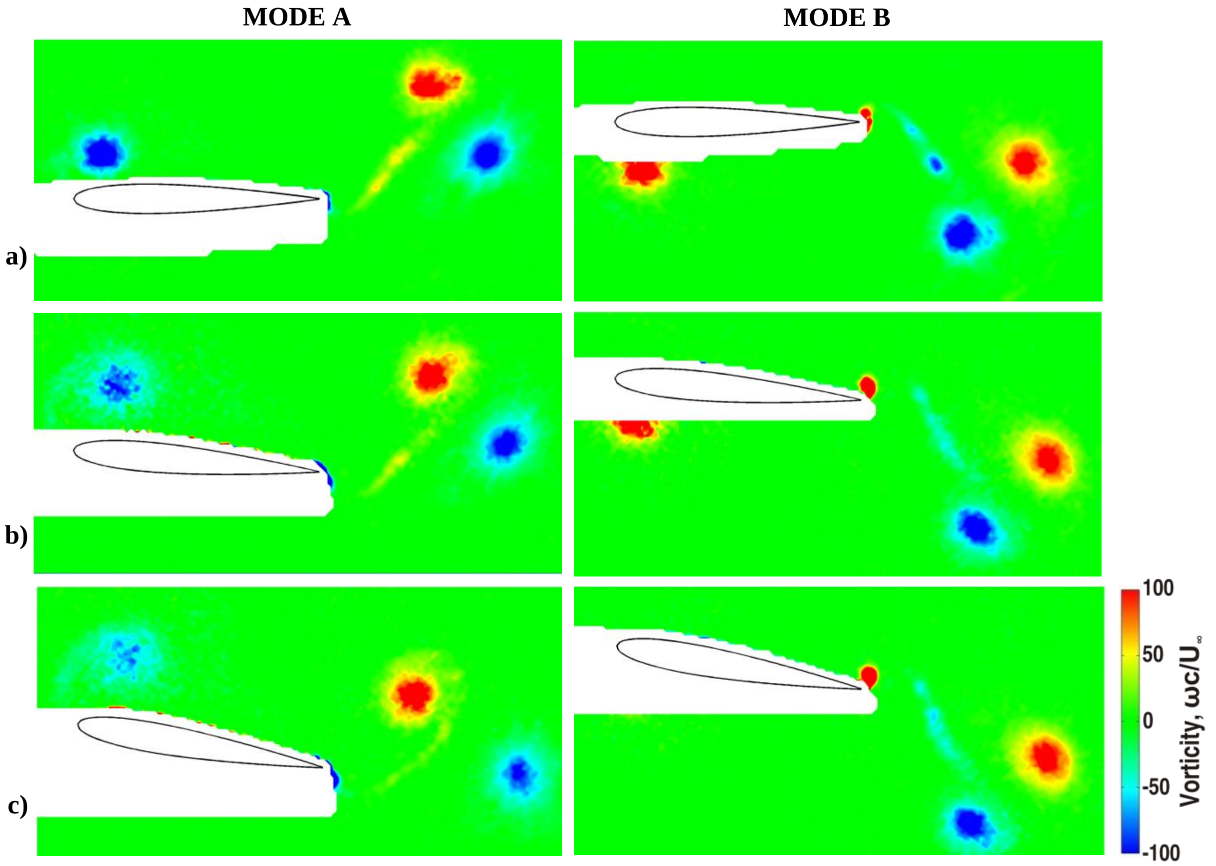

Fig. 23 Phase-averaged vorticity contour plots comparing the mode A flow field (left) at the bottom of the motion, and mode B flow field (right) at the top of the motion for a/c = 0.15, Sr_c = 2.025 and: a) α = 0°, b) α = 5°, and c) α = 10°. NACA 0012 airfoil, *Re* = 10,000.

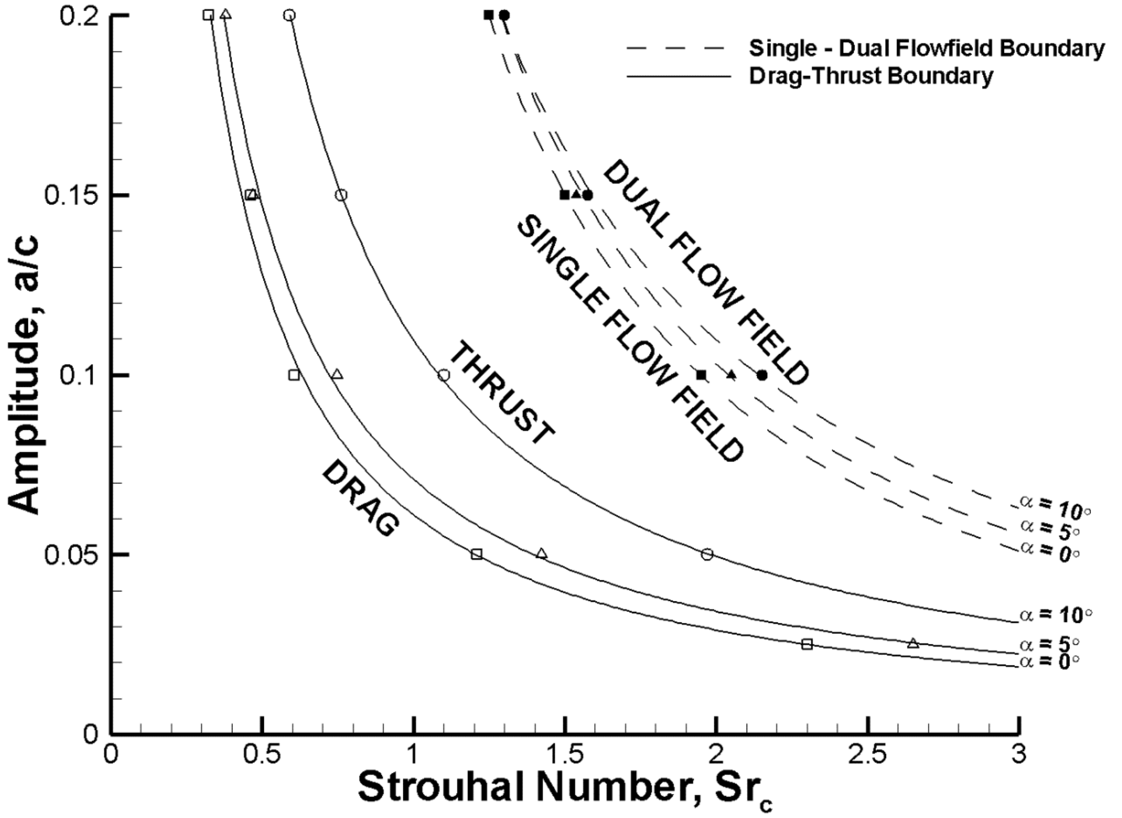

Fig. 24 Boundary between drag / thrust producing and single / dual flow field for: α = 0° (square), α = 5° (triangle), and α = 10° (circle). Lines are power law curve fits. NACA 0012 airfoil, *Re* = 10,000.

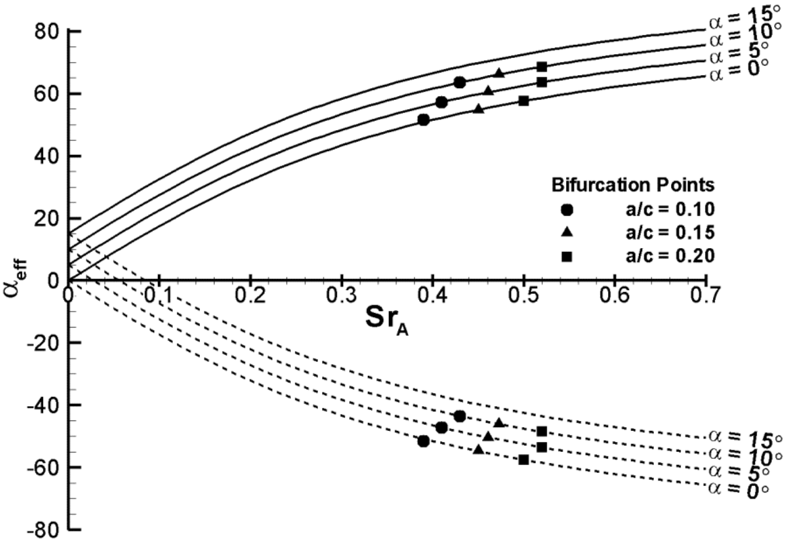

Fig. 25 Effective angle of attack as a function of Strouhal number based on amplitude. Solid line: αeff,max, dashed line: αeff,min. Symbols denote the point of bifurcation as determined from the force measurements. NACA 0012 airfoil, *Re* = 10,000.

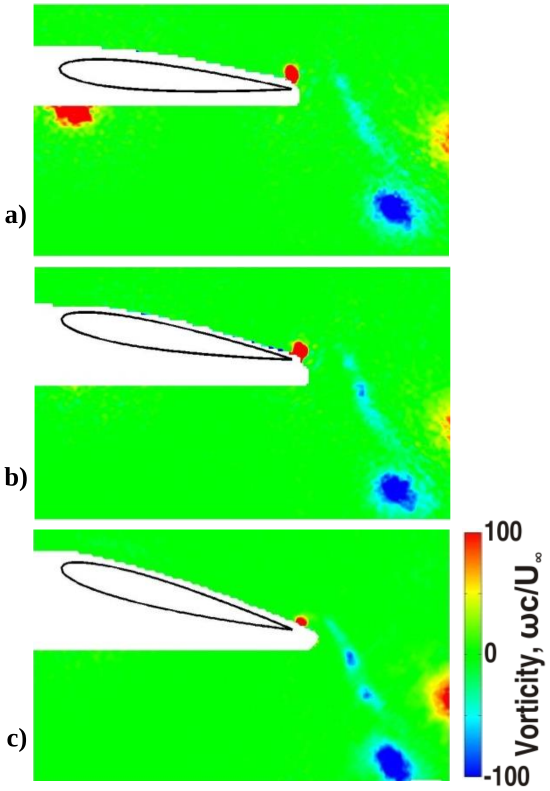

Fig. 26 Vorticity contours showing the similarity of flow fields across different angles of attack for a/c = 0.150, Sr_c = 2.025 and: a) α = 5° - mode B, b) α = 10° - mode B, and c) α = 15°. NACA 0012 airfoil, *Re* = 10,000.

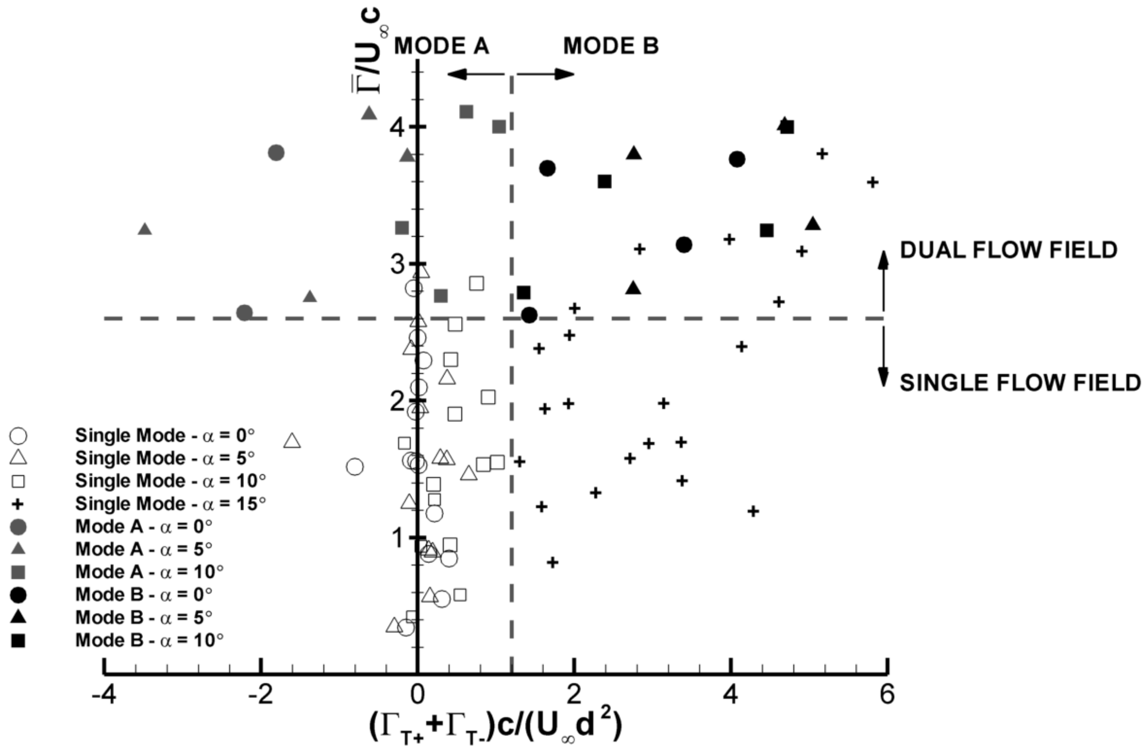

Fig. 27 Normalized circulation as a function of asymmetry parameter. NACA 0012 airfoil, *Re* = 10,000.

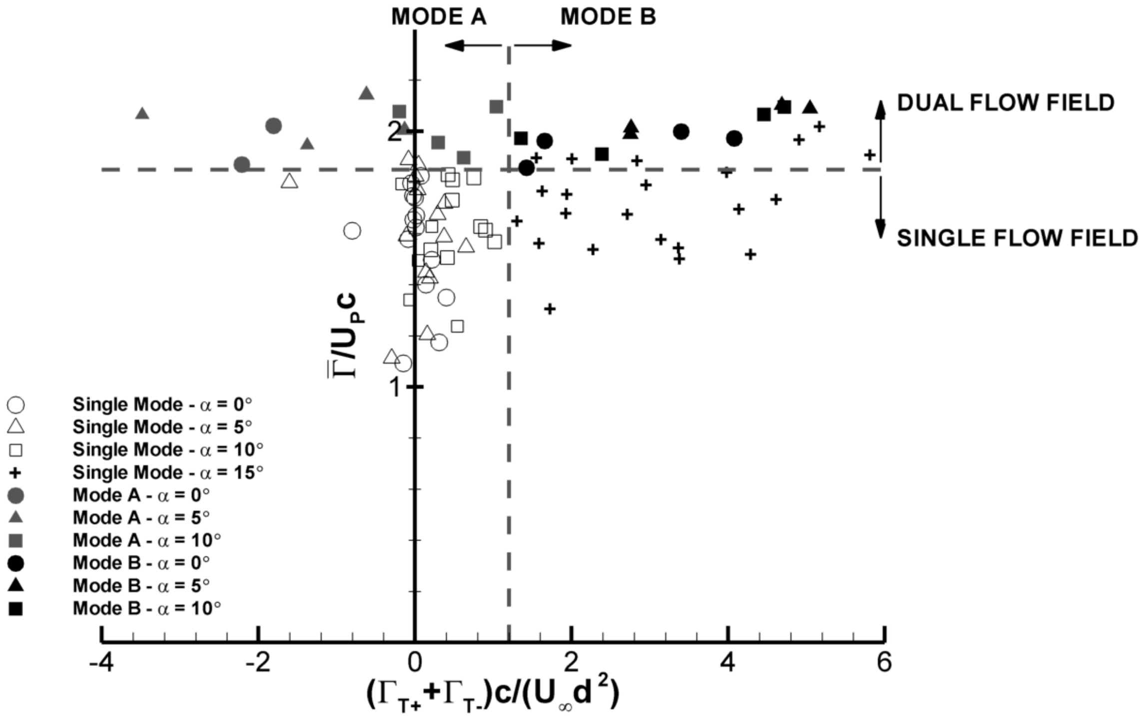

Fig. 28 Circulation normalized by plunge velocity as a function of asymmetry parameter. NACA 0012 airfoil, *Re* = 10,000.

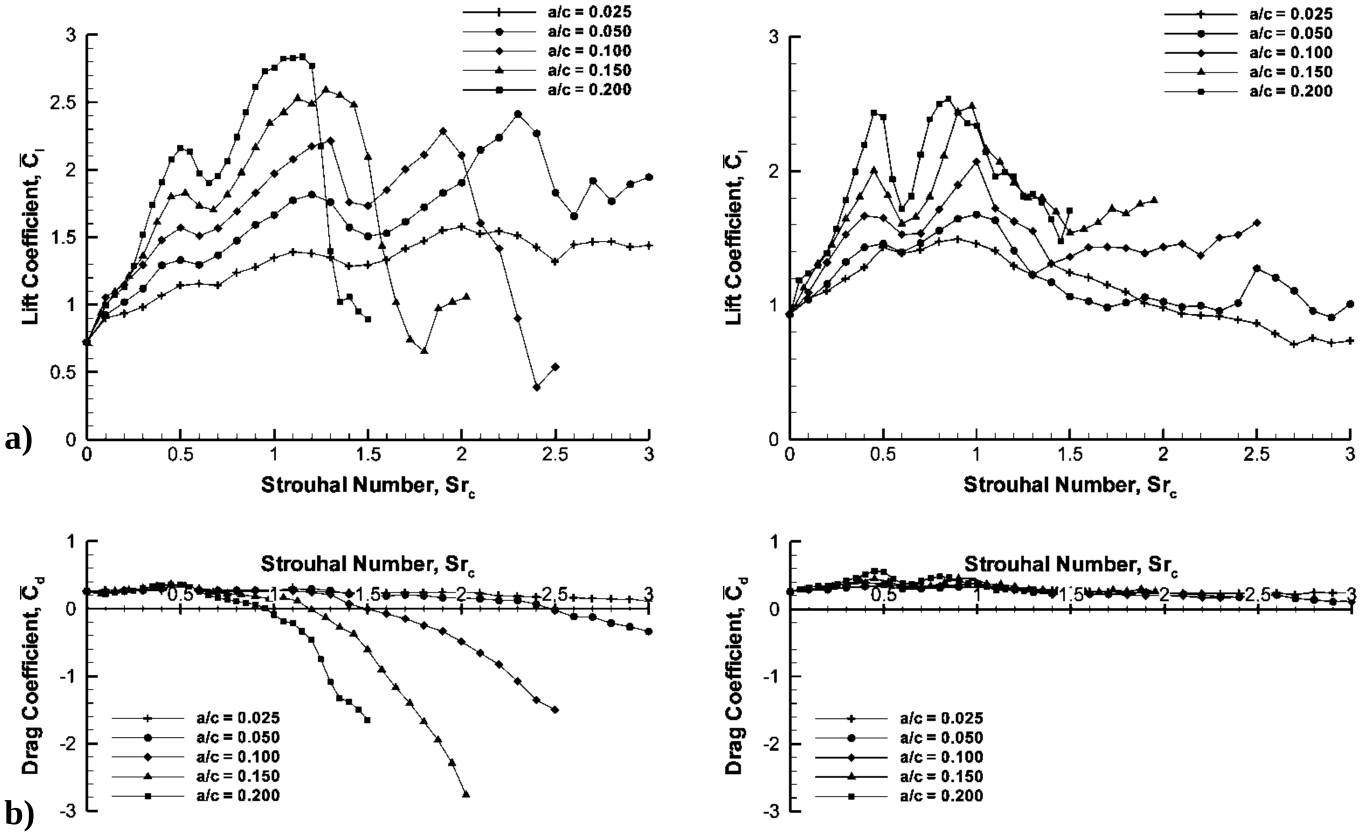

Fig. 29 a) Time-averaged lift coefficient, and b) drag coefficient plotted against Strouhal number based on chord for the NACA 0012 airfoil (left column) and the flat plate (right column) at $\alpha = 15°$. *Re* = 10,000.

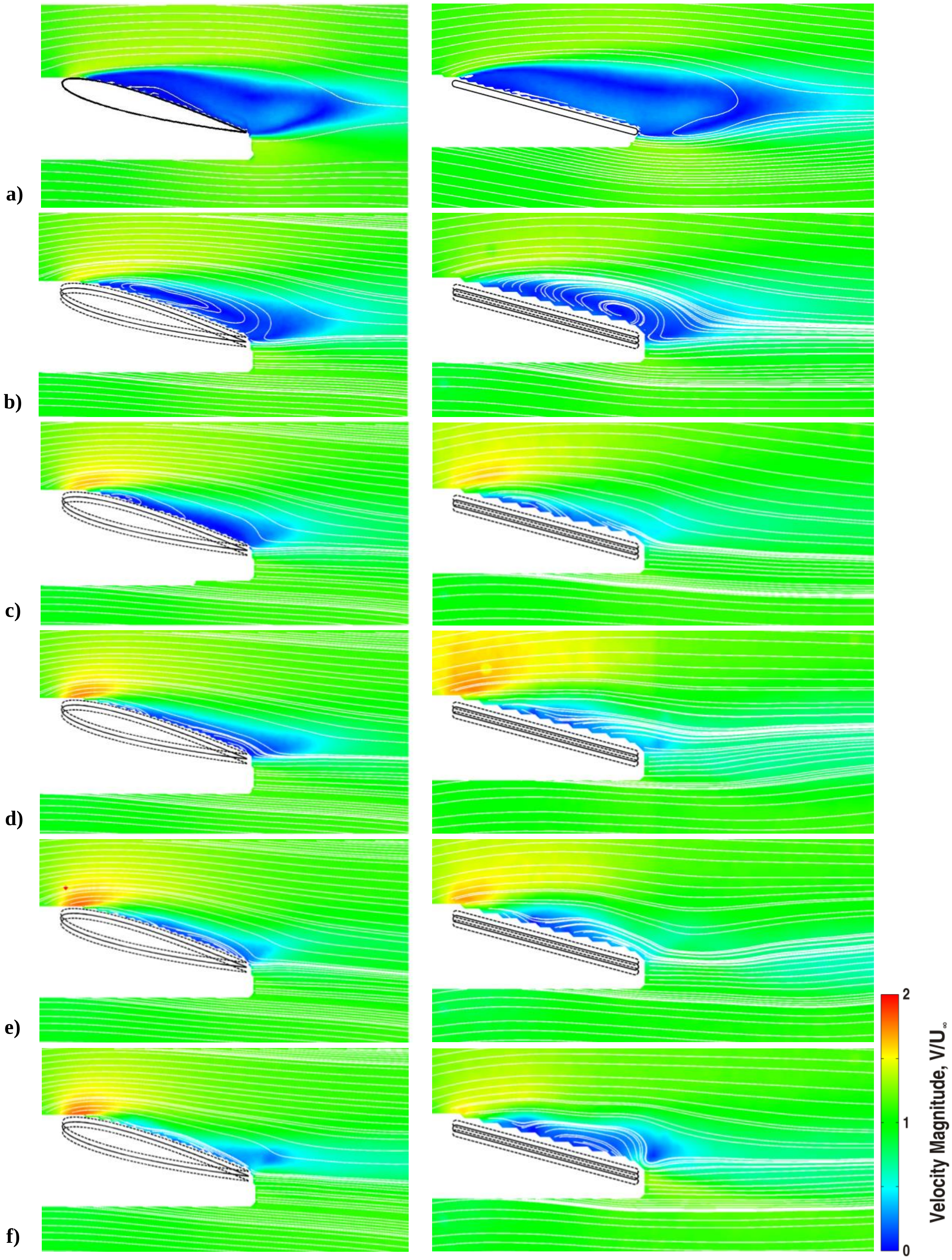

Fig. 30 Time-averaged velocity magnitude for the NACA 0012 airfoil (left column) and flat plate (right column) for a/c = 0.025 and α = 15° at Strouhal numbers of: a) Sr_c = 0, b) Sr_c = 0.25, c) Sr_c = 0.50, d) Sr_c = 0.75, e) Sr_c = 1.00, f) Sr_c = 1.25, g) Sr_c = 1.50, h) Sr_c = 1.75, i) Sr_c = 2.00, j) Sr_c = 2.25, k) Sr_c = 2.50, l) Sr_c = 2.75, and m) Sr_c = 3.00 . Re = 10,000. Continued on next page.

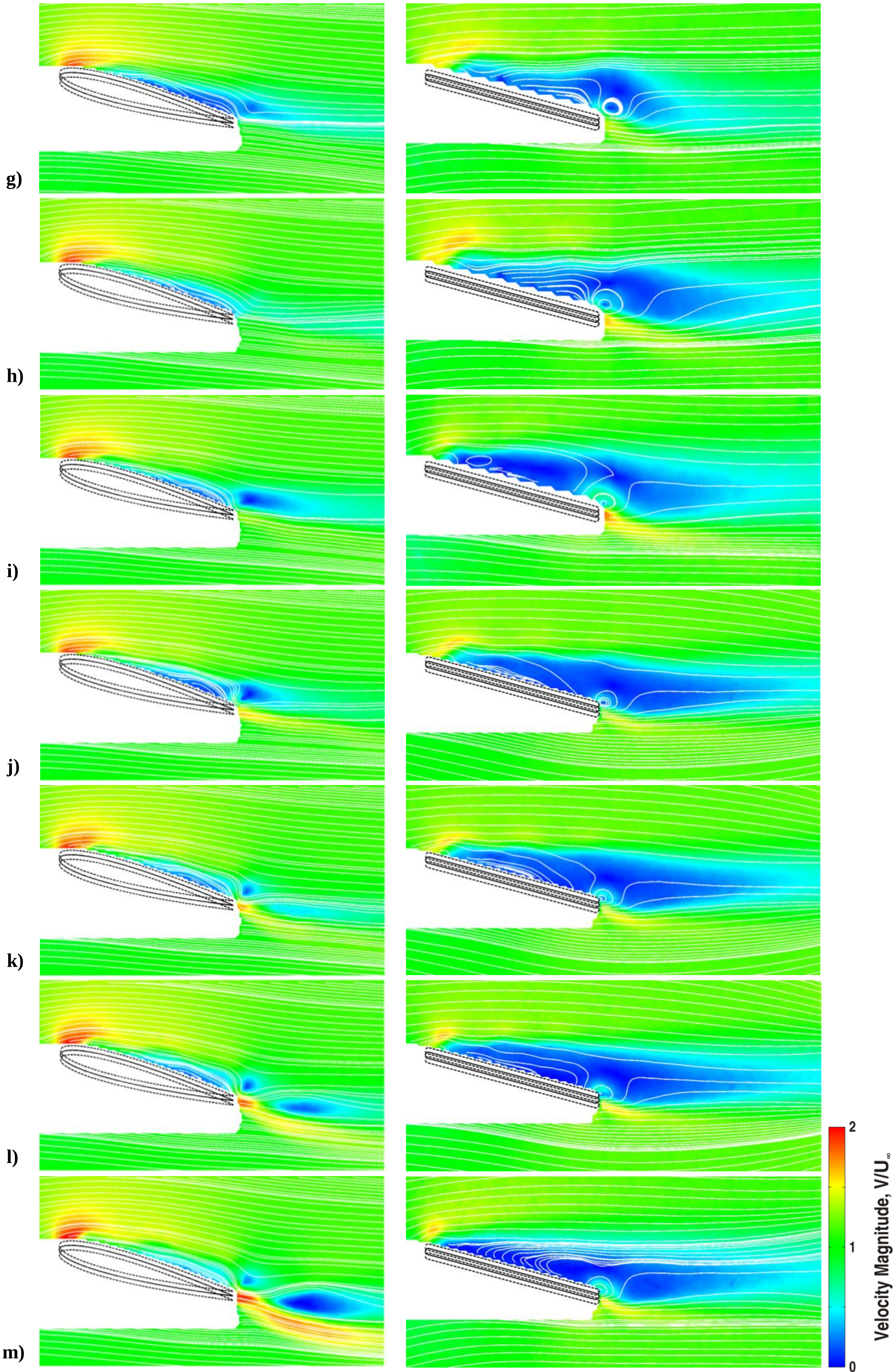

Fig. 30 Continued

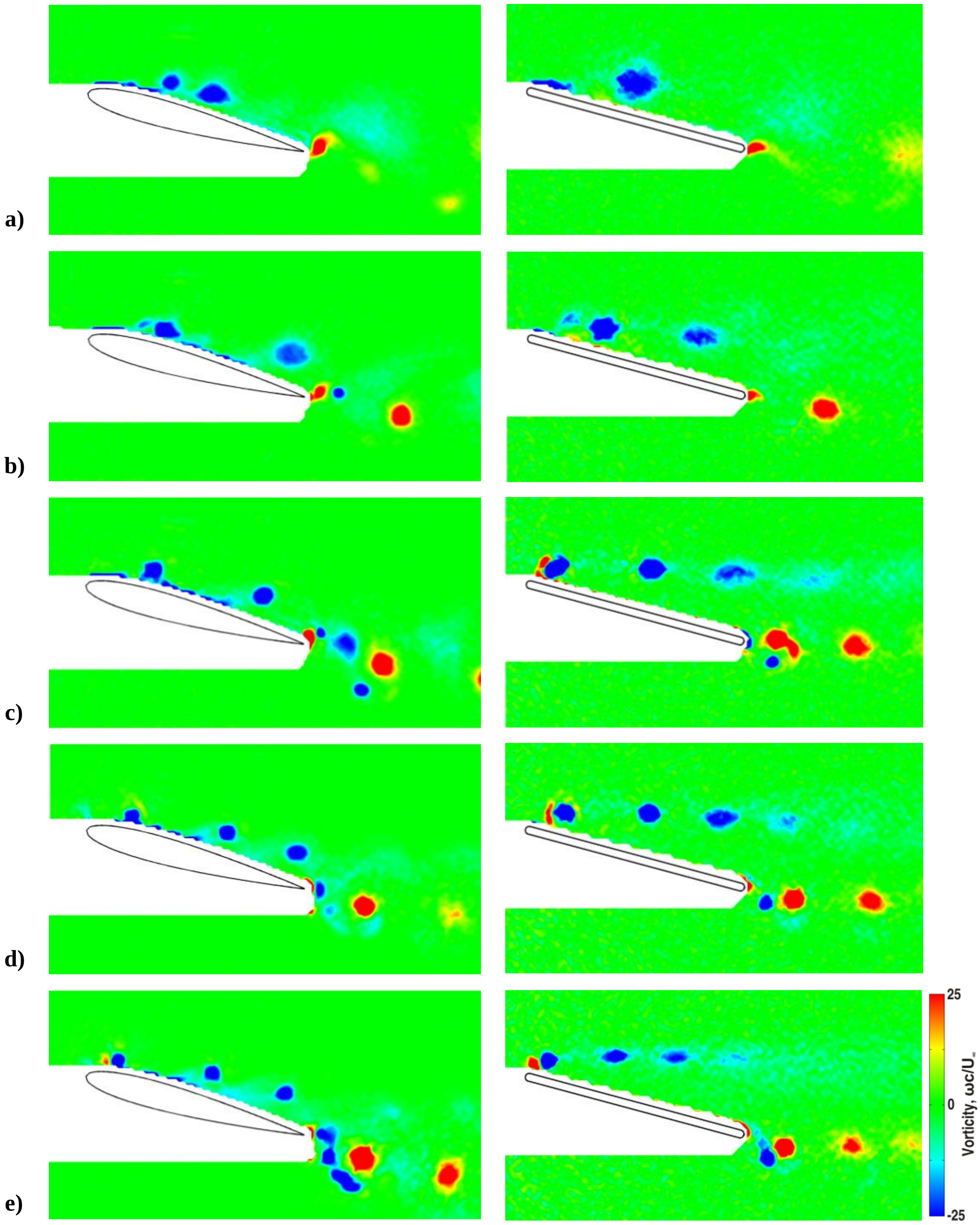

Fig. 31 Phase-averaged vorticity contour plots at the top of the motion for the NACA 0012 airfoil (left column) and flat plate (right column) for a/c = 0.025 and α = 15° at Strouhal numbers of: a) Sr_c = 1.00, b) Sr_c = 1.50, c) Sr_c = 2.00, d) Sr_c = 2.50, and e) Sr_c = 3.00. Re = 10,000.

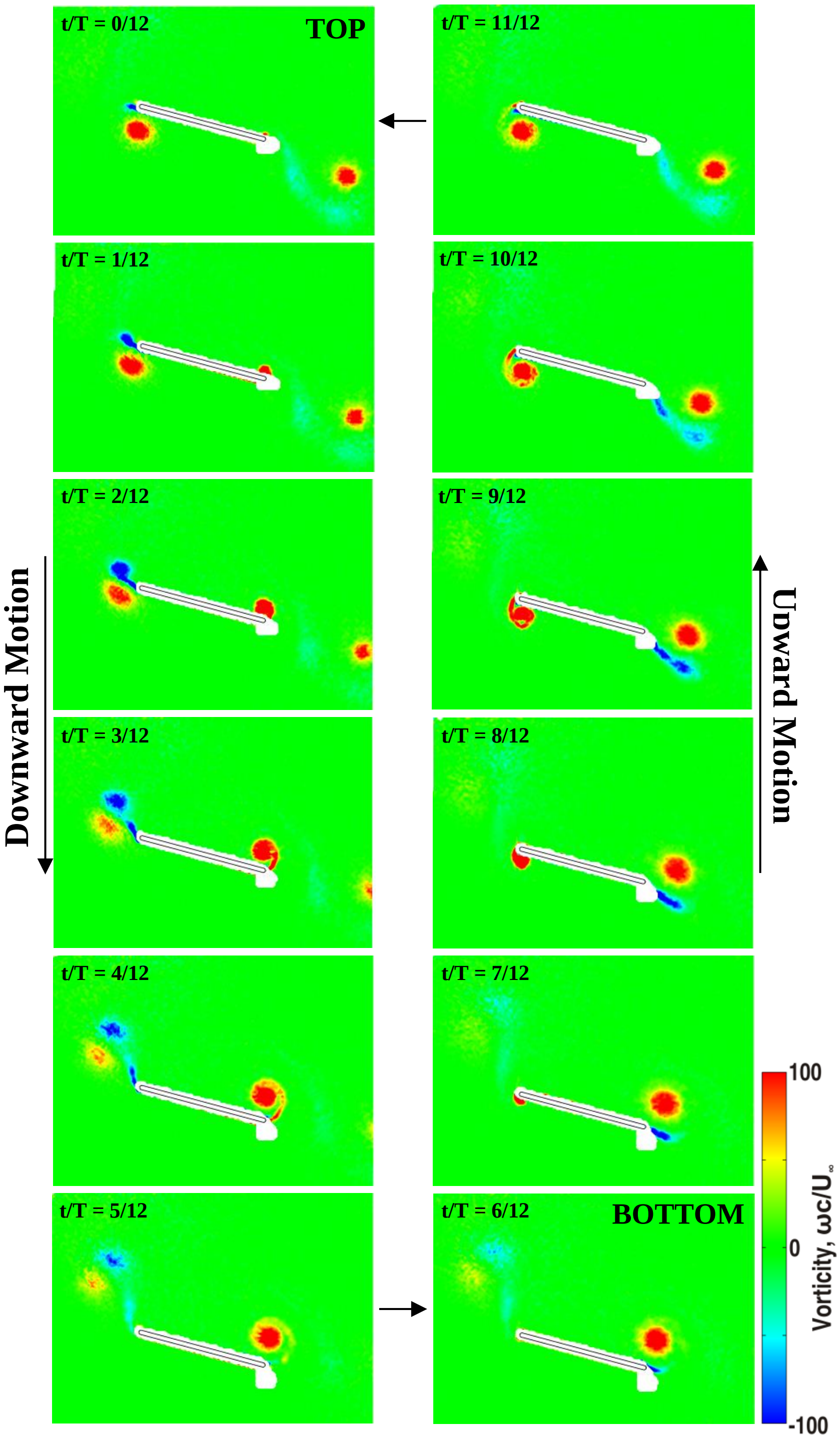

Fig. 32 Phase-averaged vorticity contour plots for the 2D flat plate at twelve phases in the cycle for α = 15°, a/c = 0.15 and Sr_c = 2.00. Re = 10,000.

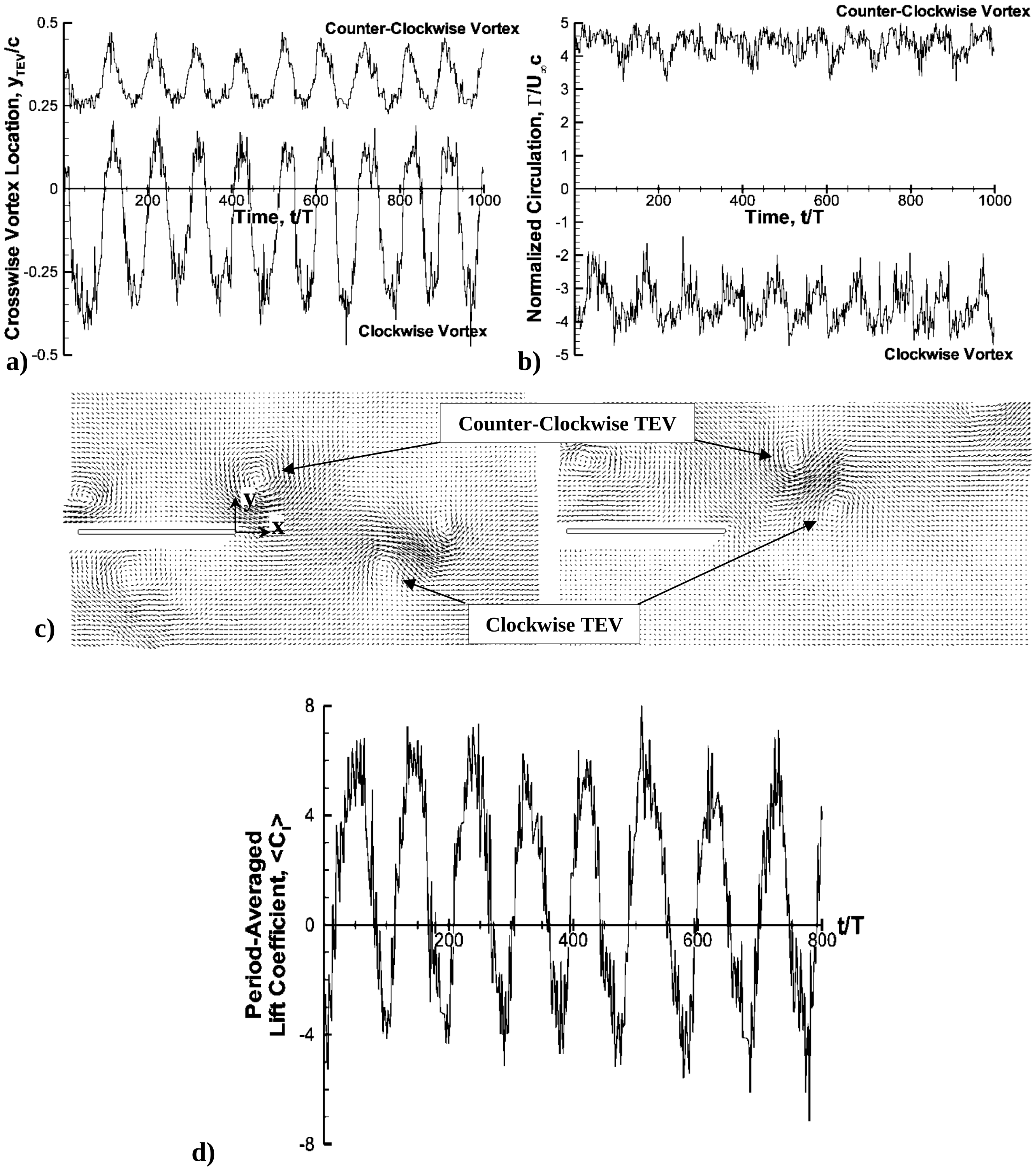

Fig. 33 a) Instantaneous cross-stream position of trailing-edge vortex as measured in phase-locked measurements at $h = -a$, b) Instantaneous normalized circulation as measured in phase-locked measurements at $h = -a$, c) Inset identifying clockwise and counter-clockwise vortex for two extreme cases, d) Period-averaged lift coefficient. Flat plate airfoil, $a/c = 0.15$, $Sr_c = 2.025$, $\alpha = 0°$, $Re = 10{,}000$.

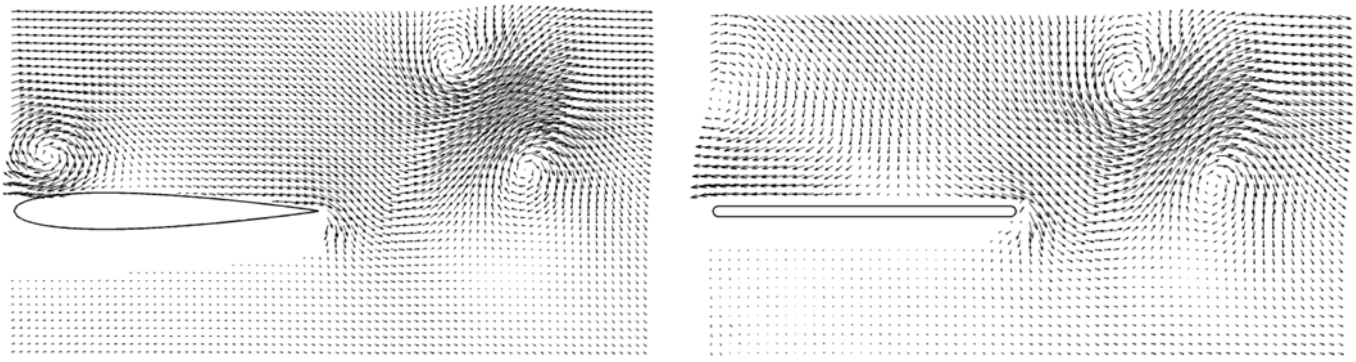

Fig. 34 Comparison of phase-averaged mode A flow fields for the NACA 0012 airfoil and flat plate airfoil. $a/c = 0.15$, $Sr_c = 2.025$, $\alpha = 0°$, $Re = 10{,}000$.

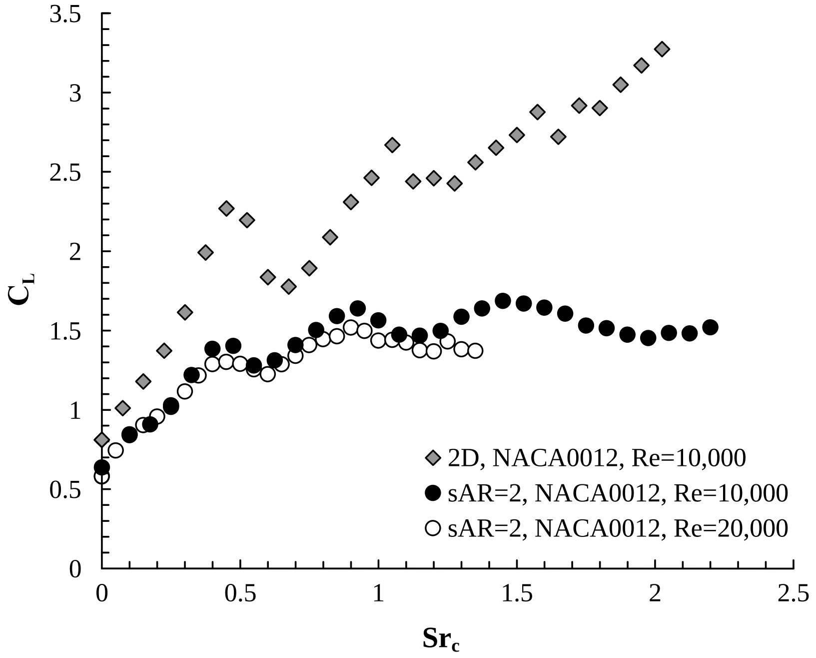

Fig. 35 Time-averaged lift measurements of a plunging NACA0012 profile airfoil and *sAR*=2 rectangular wing. *a/c* = 0.15, α = 20º.

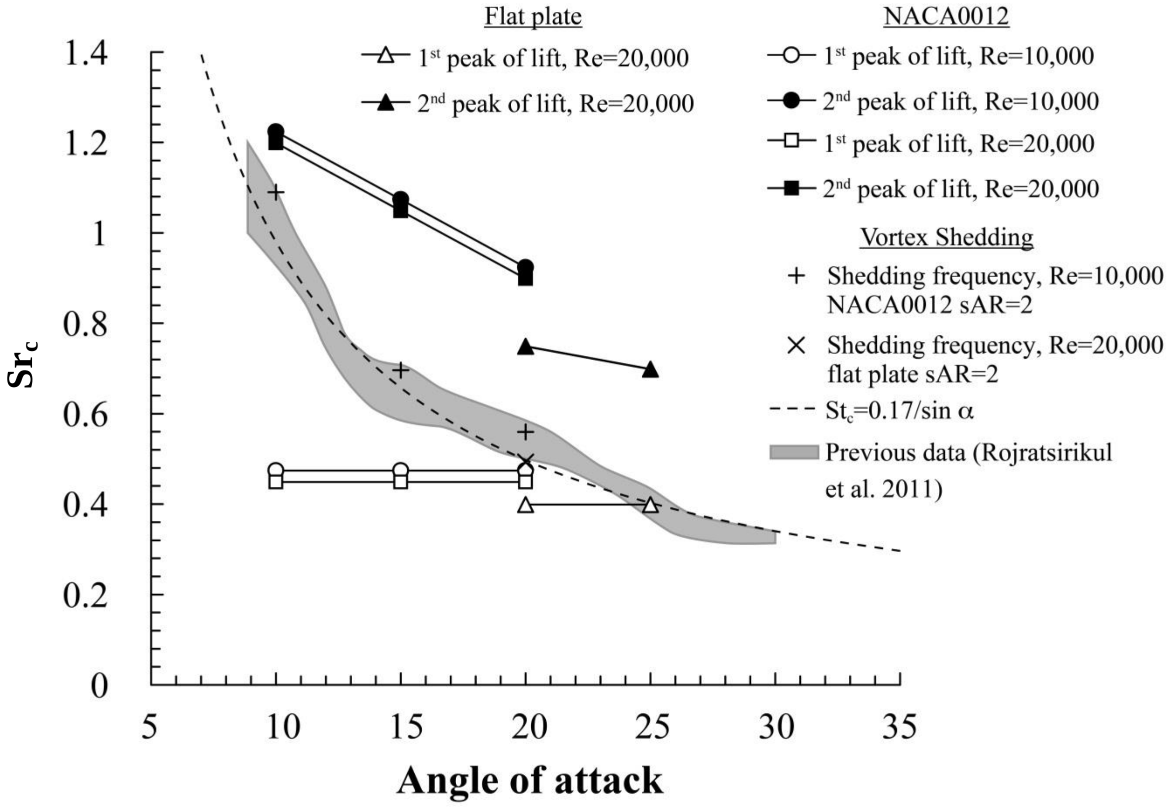

Fig. 36 Comparison between the frequency at which lift peaks occur for the oscillating wing and the natural shedding frequency of the stationary wing. ***sAR*** **= 2,** ***a/c*** **= 0.15.**

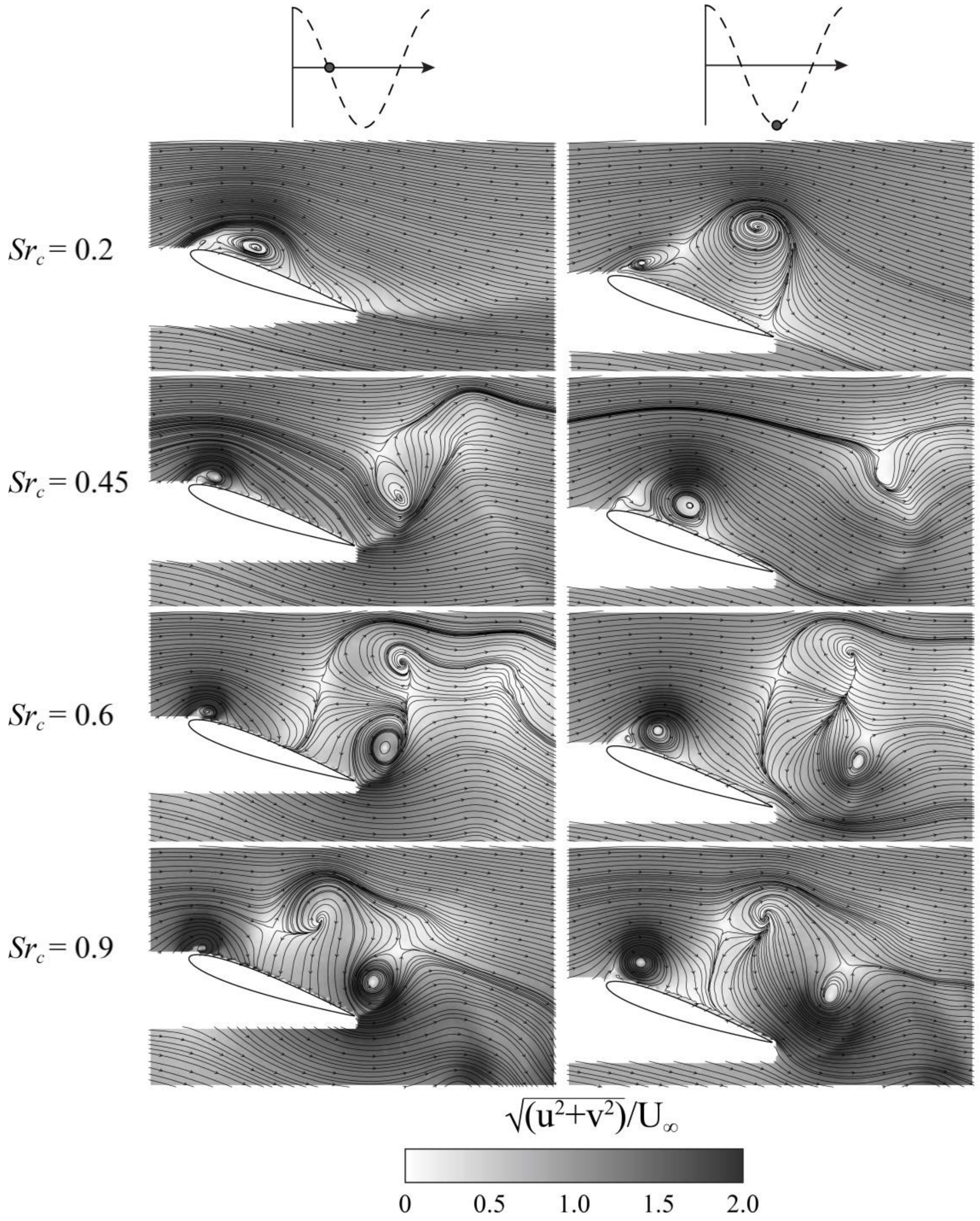

Fig. 37 Velocity magnitude and streamlines at the mid-span plane for the NACA0012 *sAR* = 2 wing taken at two phases for various Strouhal numbers, *Re* = 20,000, α = 20º, *a*/*c* = 0.15.

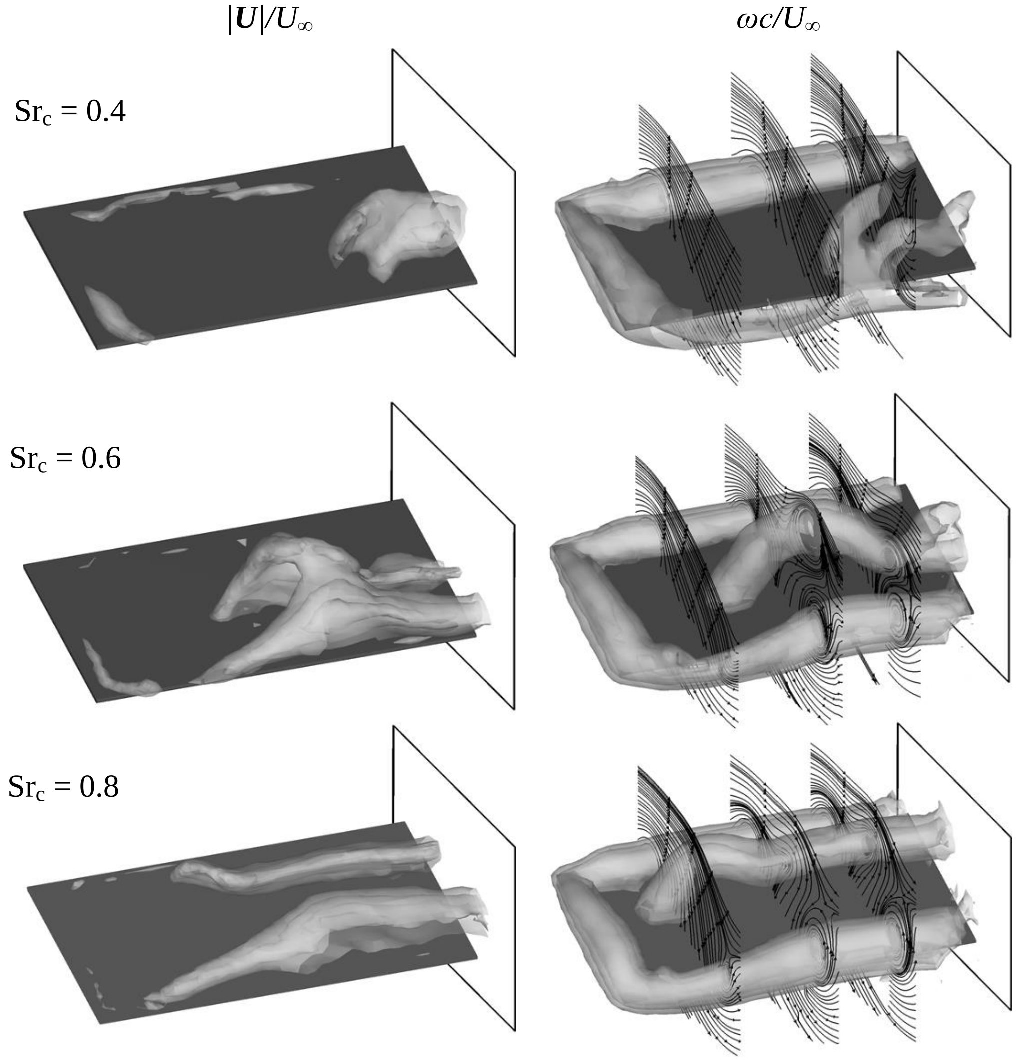

Fig. 38 Isometric views of iso-surfaces defined by constant velocity magnitude ($|U|/U_\infty$ = 0.15, 0.3 and 0.45) and vorticity magnitude ($|\omega^*|$ = 7, 15 and 25), superimposed by streamlines at three separate spanwise locations. Measurements are presented for the phase when the wing is at the botton of the motion. *sAR* = 2 wing with flat plate cross-section, *Re* = 20,000, α = 20º, *a/c* = 0.15.

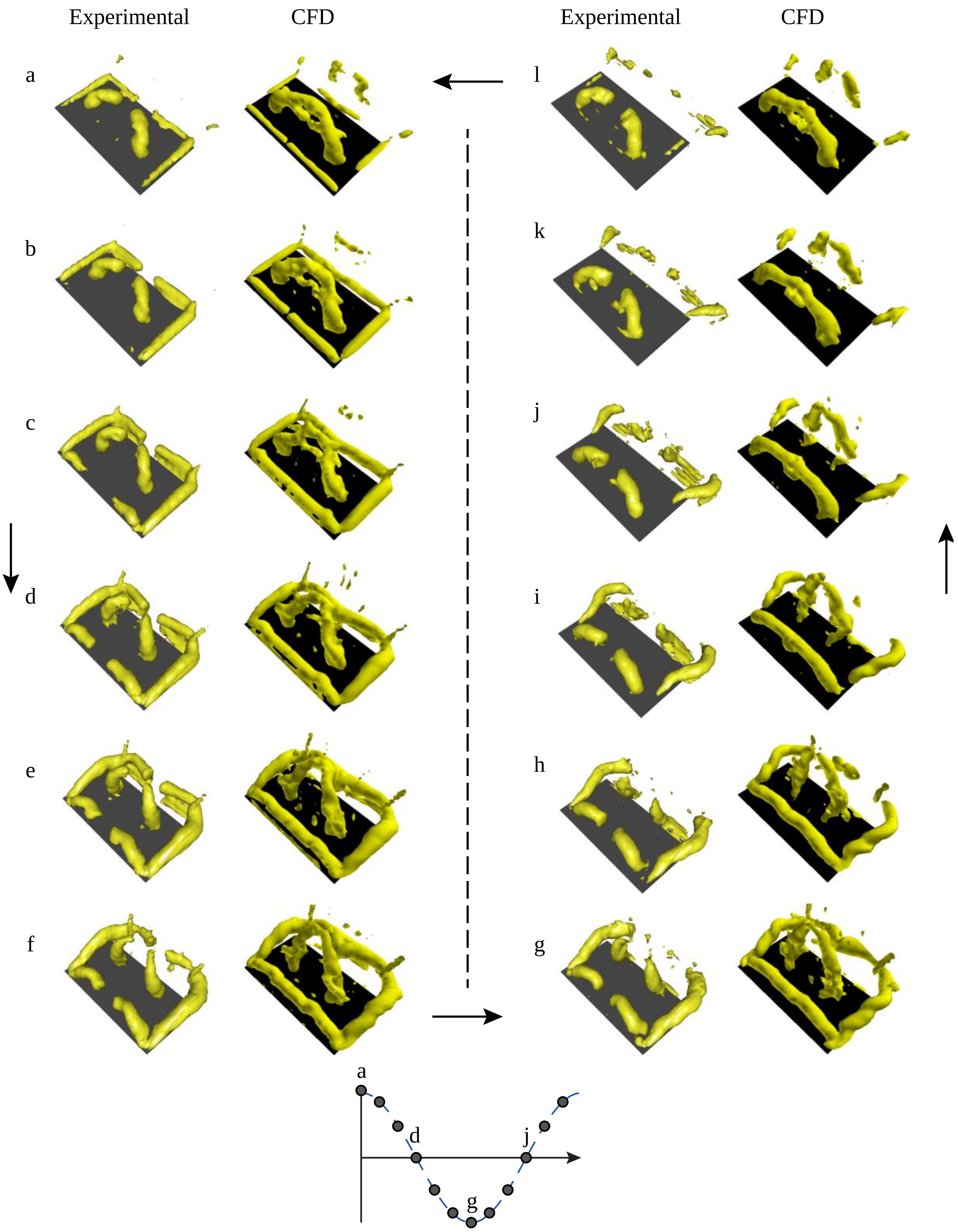

Fig. 39 A twelve-phase comparison between CFD and experimental results, for the $sAR = 1$ rectangular wing (with flat-plate cross-section) at $Sr_c = 0.65$, showing $Qc/U_\infty = 20$. $Re = 20{,}000$, $\alpha = 20^\circ$, $a/c = 0.15$.

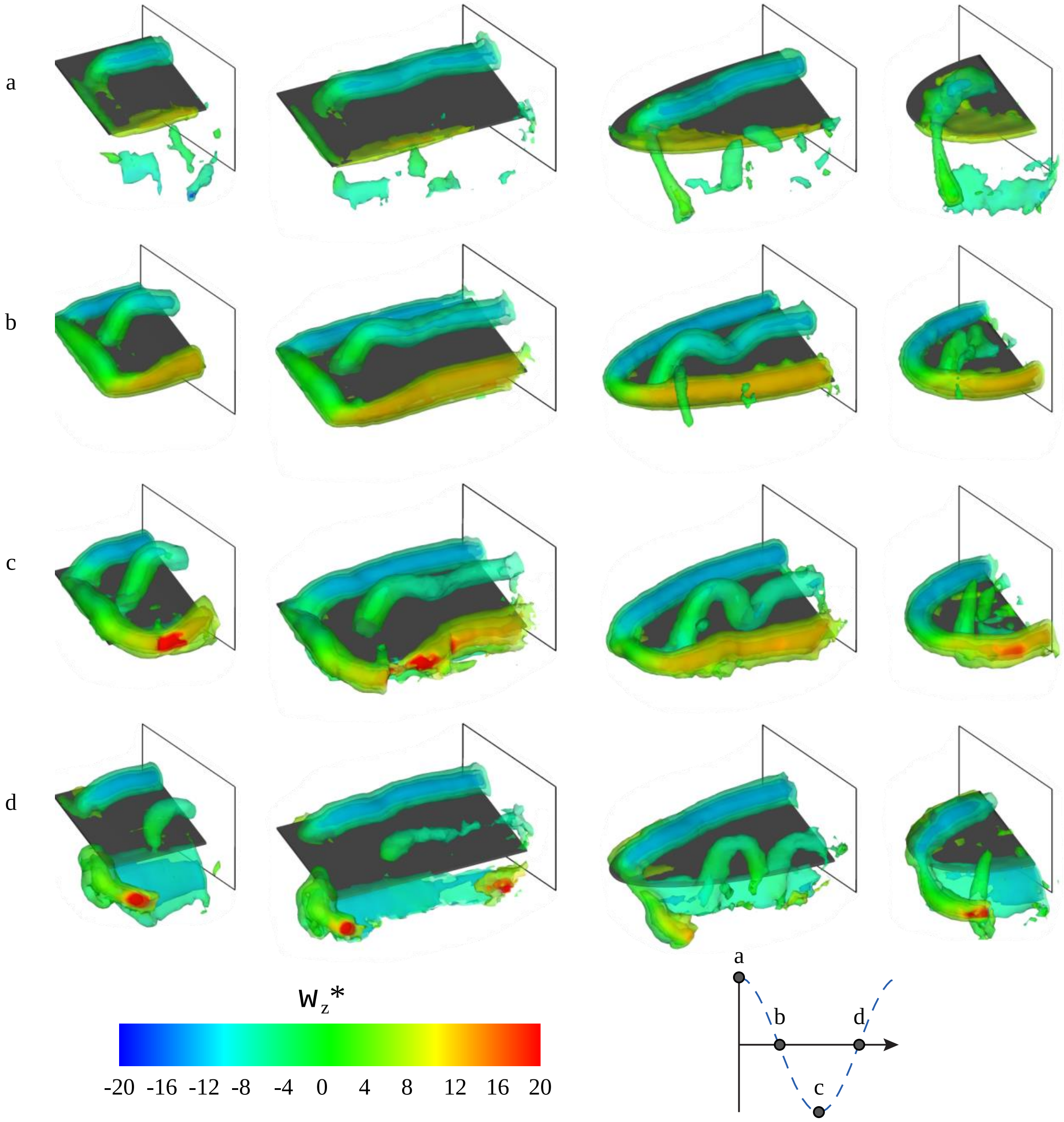

Fig. 40 A comparison between different wing planforms at Sr_c = 0.8. Iso-surfaces represent constant vorticity magnitude, $|\omega^*|$ =7, 15 and 25 and colour maps represent spanwise vorticity. Re = 20,000, α = 20°, a/c = 0.15.

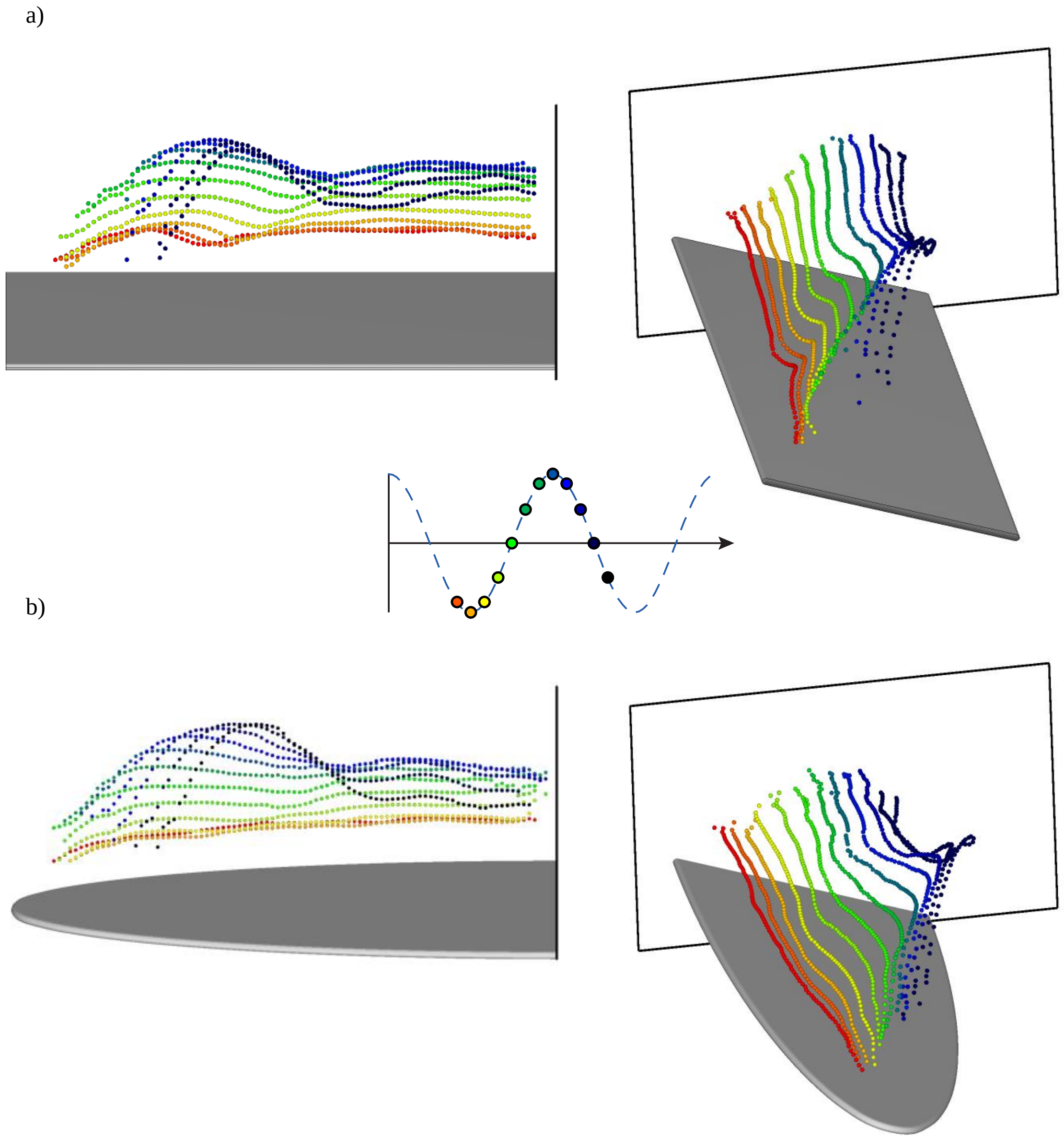

Fig. 41 Vortex core tracking for a) rectangular and b) elliptical wings, at Sr_c = 0.75, viewed from different angles. The wing corresponds to its location at the bottom of the cycle. *Re* = 20,000, α = 20º, *a/c* = 0.15.

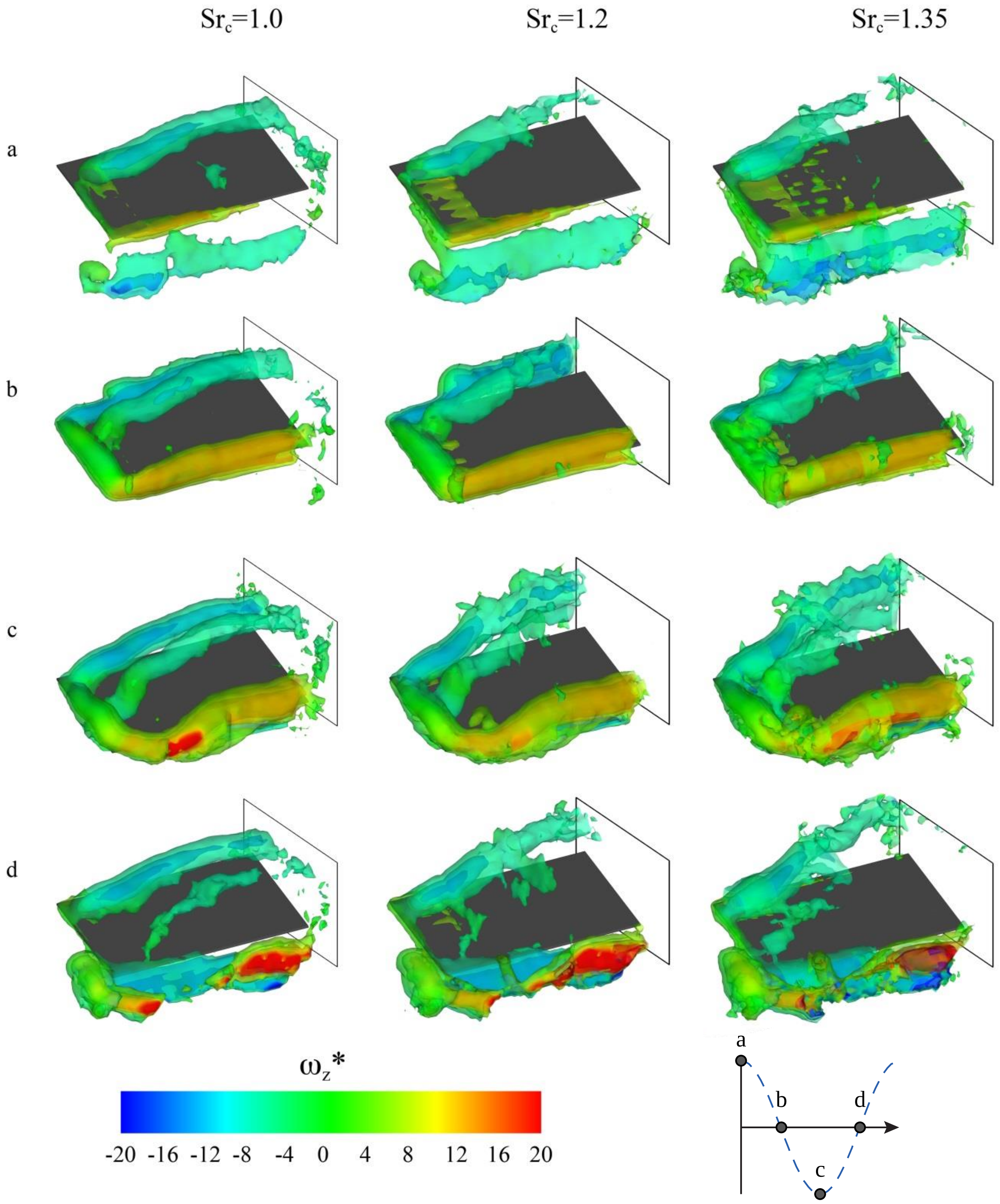

Fig. 42 Isometric views of the vortices that surround the *sAR* = 2 flat-plate rectangular wing at four phases in the cycle for various frequencies, operating at *Re* = 20,000. Iso-surfaces represent constant vorticity magnitude, $|\omega^*|$ = 7, 15 and 25. α = 20º, *a*/*c* = 0.15.

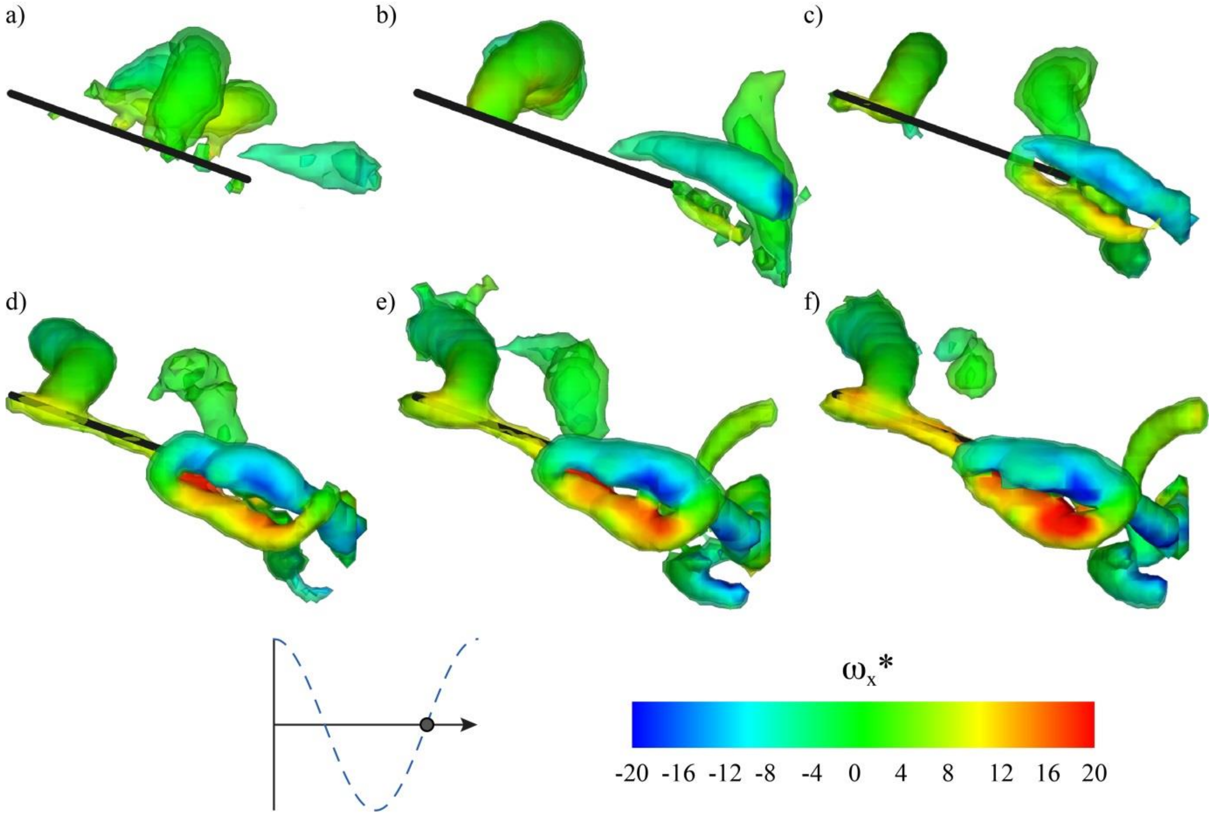

Fig. 43 A side view of the Q-criterion iso-surfaces surrounding the *sAR* = 1 rectangular wing at t* = 0.75 for various frequencies: a) Sr_c = 0.4, b) Sr_c = 0.6, c) Sr_c = 0.8, d) Sr_c = 1.0, e) Sr_c = 1.2 and f) Sr_c = 1.35. Iso-surfaces represent constant Q-Criterion, Qc/U_∞ = 15, 30 and 45 and colour maps represent streamwise vorticity. *Re* = 20,000, α = 20°, *a*/*c* = 0.15.

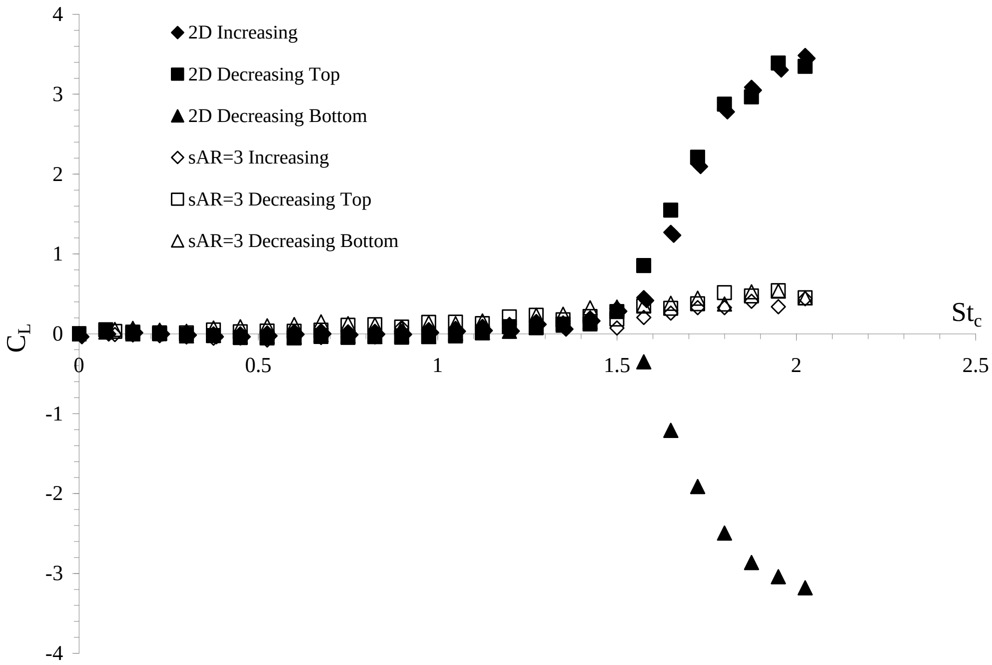

Fig. 44 A comparison of the time-averaged lift, at various operating Strouhal numbers, obtained for the 2D NACA0012 airfoil and *sAR* = 3 NACA0012 rectangular wings.

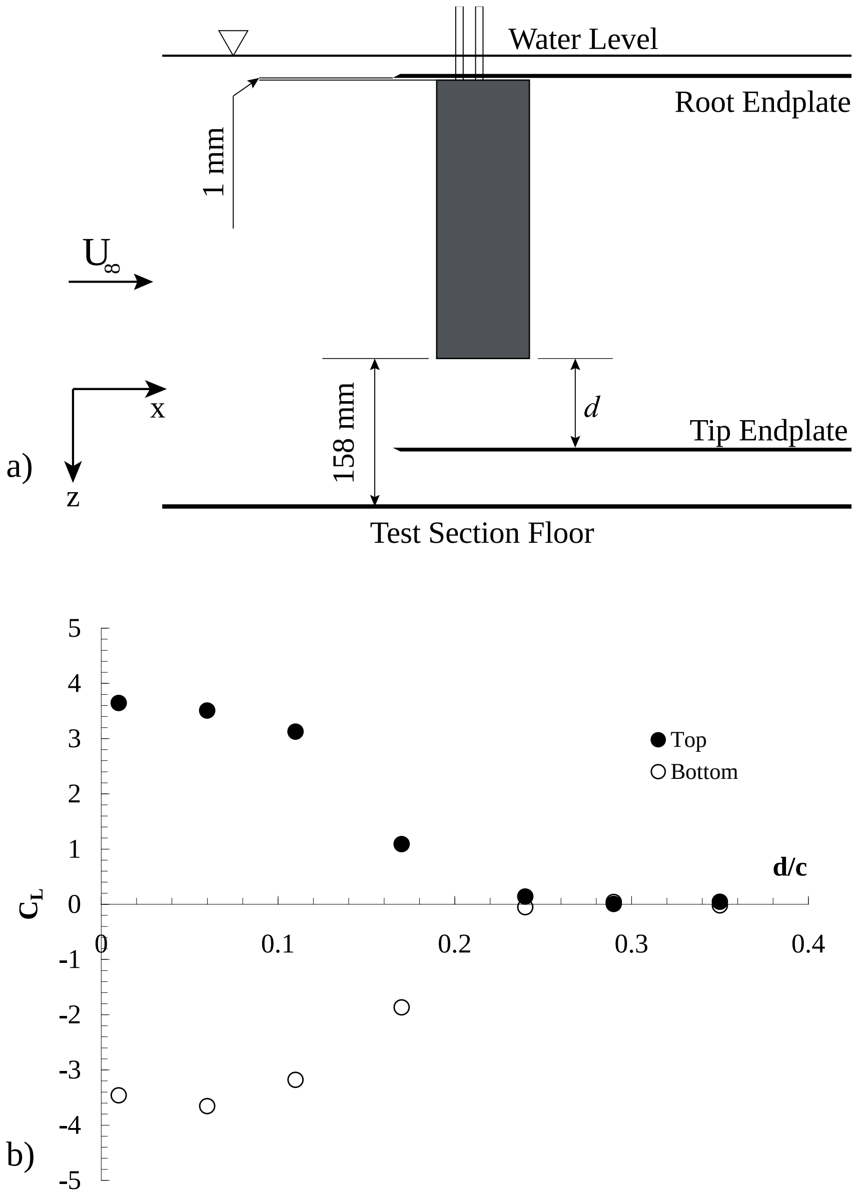

Fig. 45 a) schematic of the test section, showing the *sAR* = 3 NACA0012 wing. The distance *d* between the tip of the wing and the endplate is varied by adjusting the height of the tip endplate; b) the effect of tip spacing on the time-averaged lift, the hollow and solid markers represent the wing impulsively started from the bottom and top of the motion, respectively.

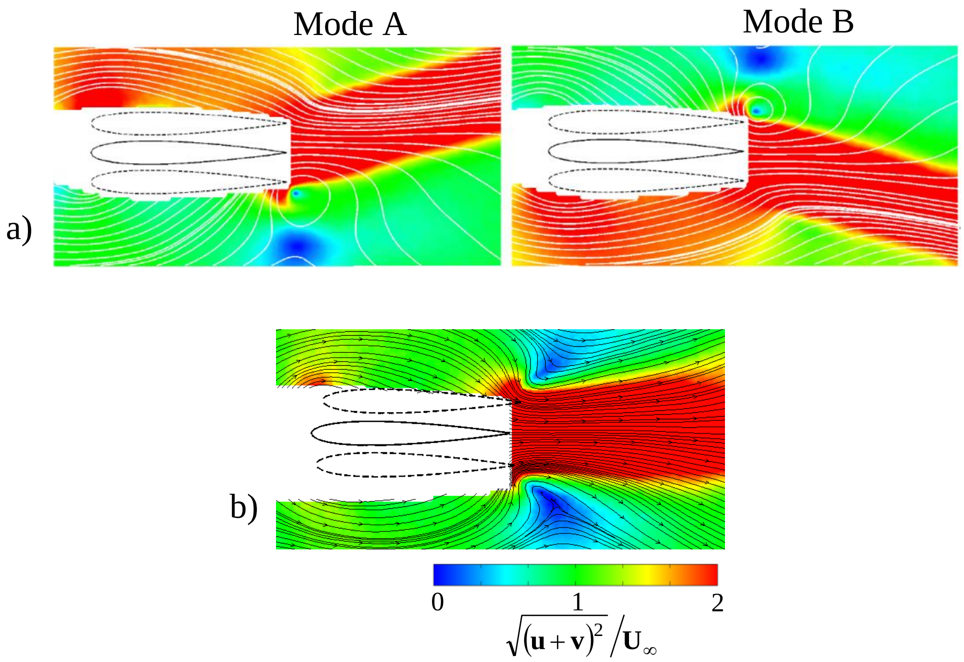

Fig. 46 Time-averaged flow showing non-dimensionalised velocity magnitude for the a) two bifurcation modes of the 2D NACA0012 airfoil and b) the symmetric flow of the *sAR* = 3 NACA0012 rectangular wing, both taken at *z*/*c* = 1.5.

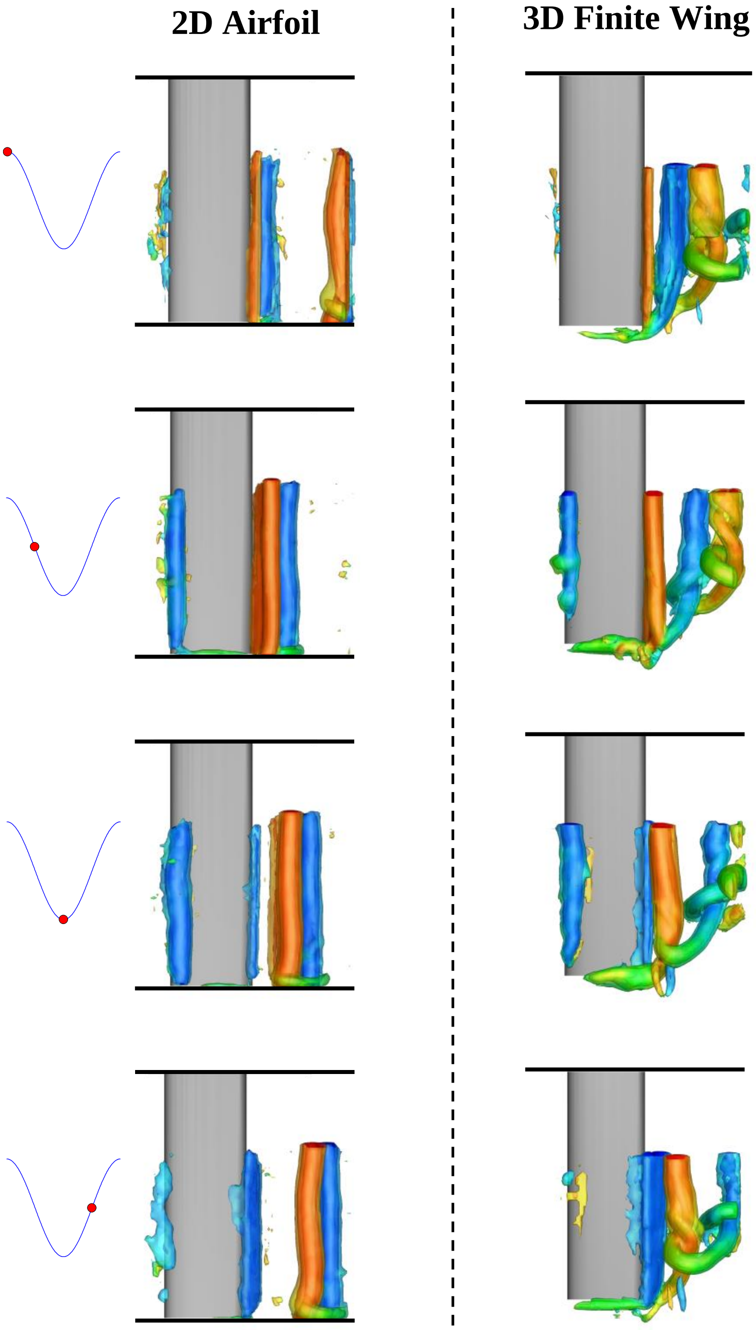

Fig. 47 Top view of iso-surfaces defined by non-dimensionalised vorticity magnitude for a) 2D airfoil and b) *sAR* = 3 finite wing.

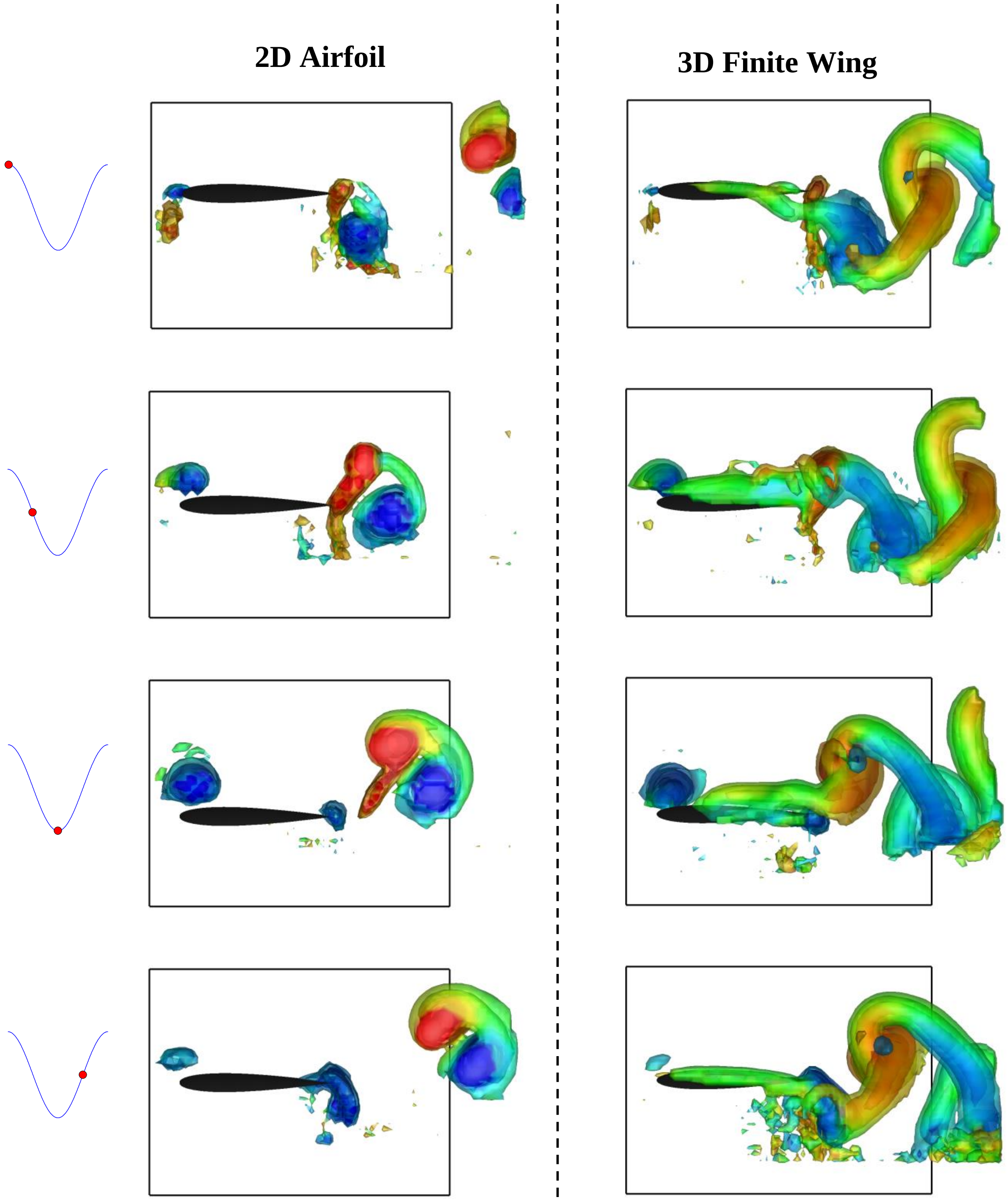

Fig. 48 Side view of iso-surfaces defined by non-dimensionalised vorticity magnitude for a) 2D airfoil and b) *sAR* = 3 finite wing.

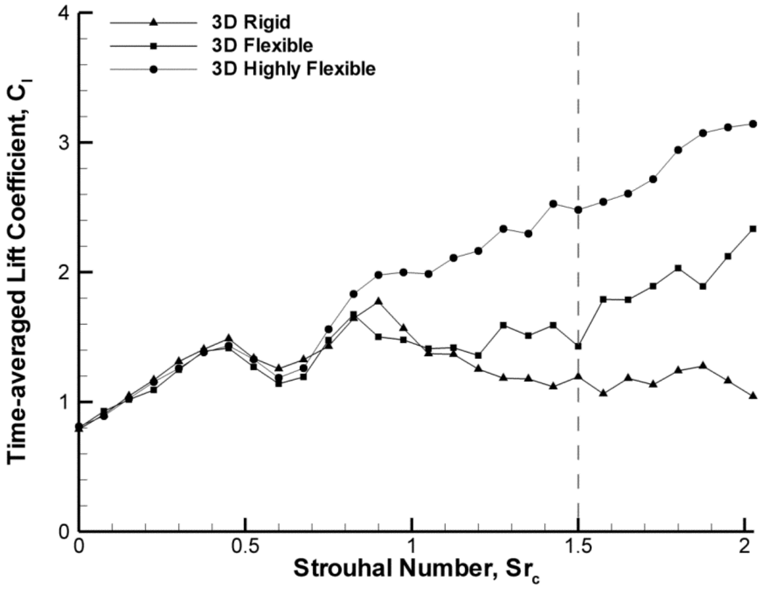

Fig. 49 Time-averaged lift coefficient as a function of Strouhal number. The wing natural frequency was measured as $Sr_c \approx 2.2$ for the flexible wing and $Sr_c \approx 1.5$ for the highly flexible wing.

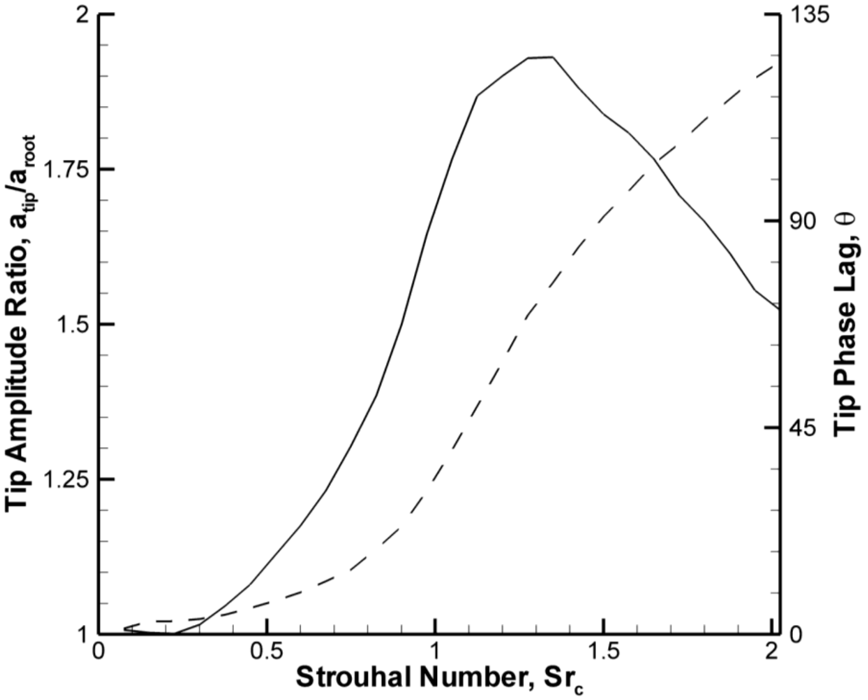

Fig. 50 Tip amplitude ratio (solid line) and tip phase lag (dashed line) against Strouhal number. The wing natural frequency was measured as $Sr_c \approx 1.5$. $sAR = 3$, $Re = 10{,}000$, $\alpha = 15^\circ$, $a/c = 0.15$.

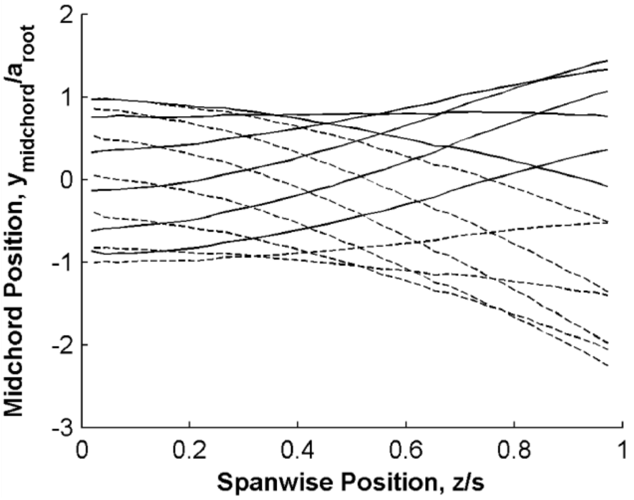

Fig. 51 Midchord position of the highly flexible wing normalized by the root amplitude for ten selected instants oscillating at *Sr*$_c$ = 1.50. Solid line is for the root moving downwards; dashed line is for the root moving upwards. *sAR* = 3, *Re* = 10,000, α = 15º, *a/c* = 0.15.

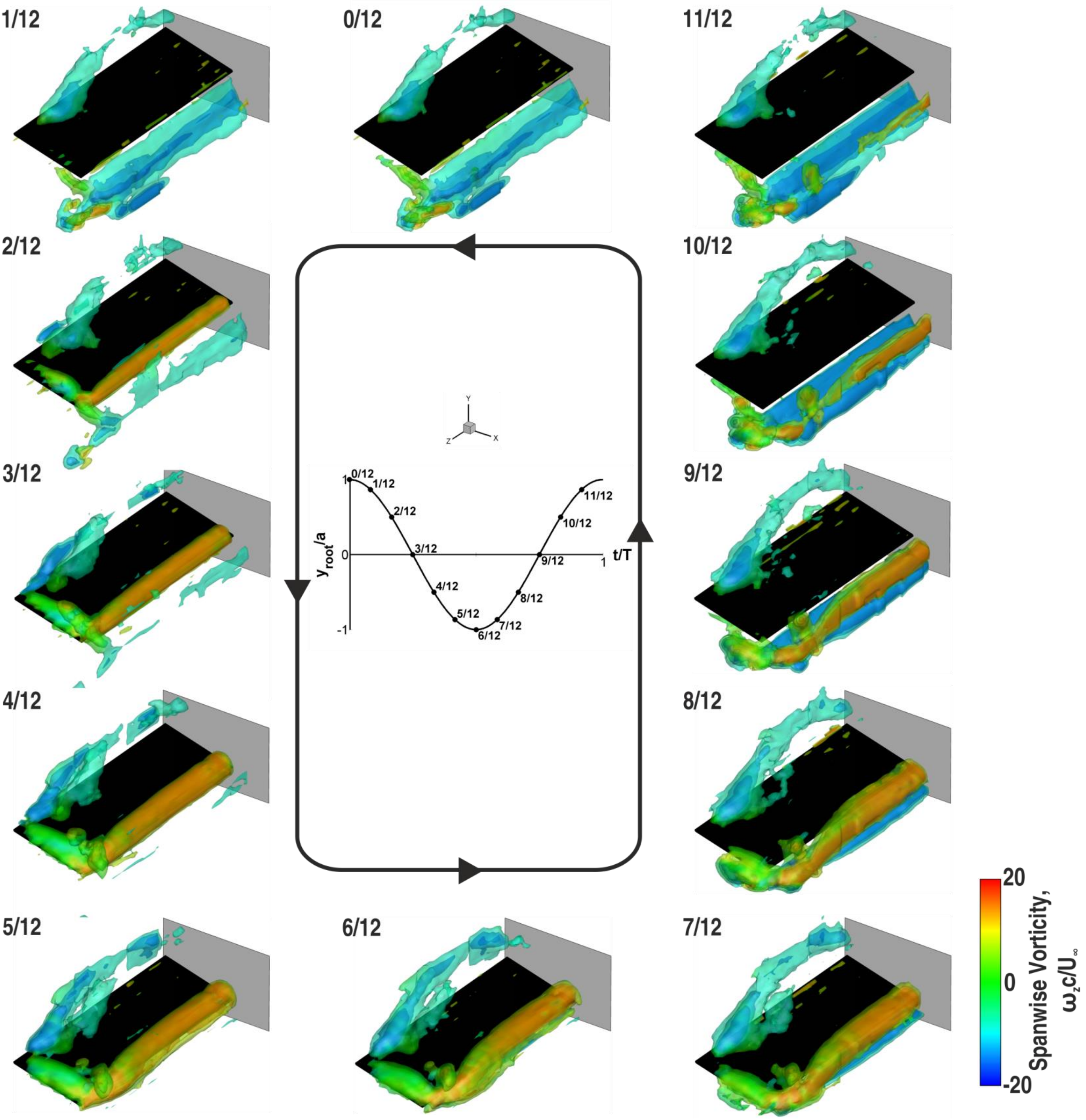

Fig. 52 Isosurfaces of phase-averaged vorticity magnitude ($\omega c/U_\infty$ = 8, 16, and 24) overlaid with spanwise vorticity for the rigid wing oscillating with Sr_c = 1.50. sAR = 3, Re = 10,000, α = 15º, a/c = 0.15.

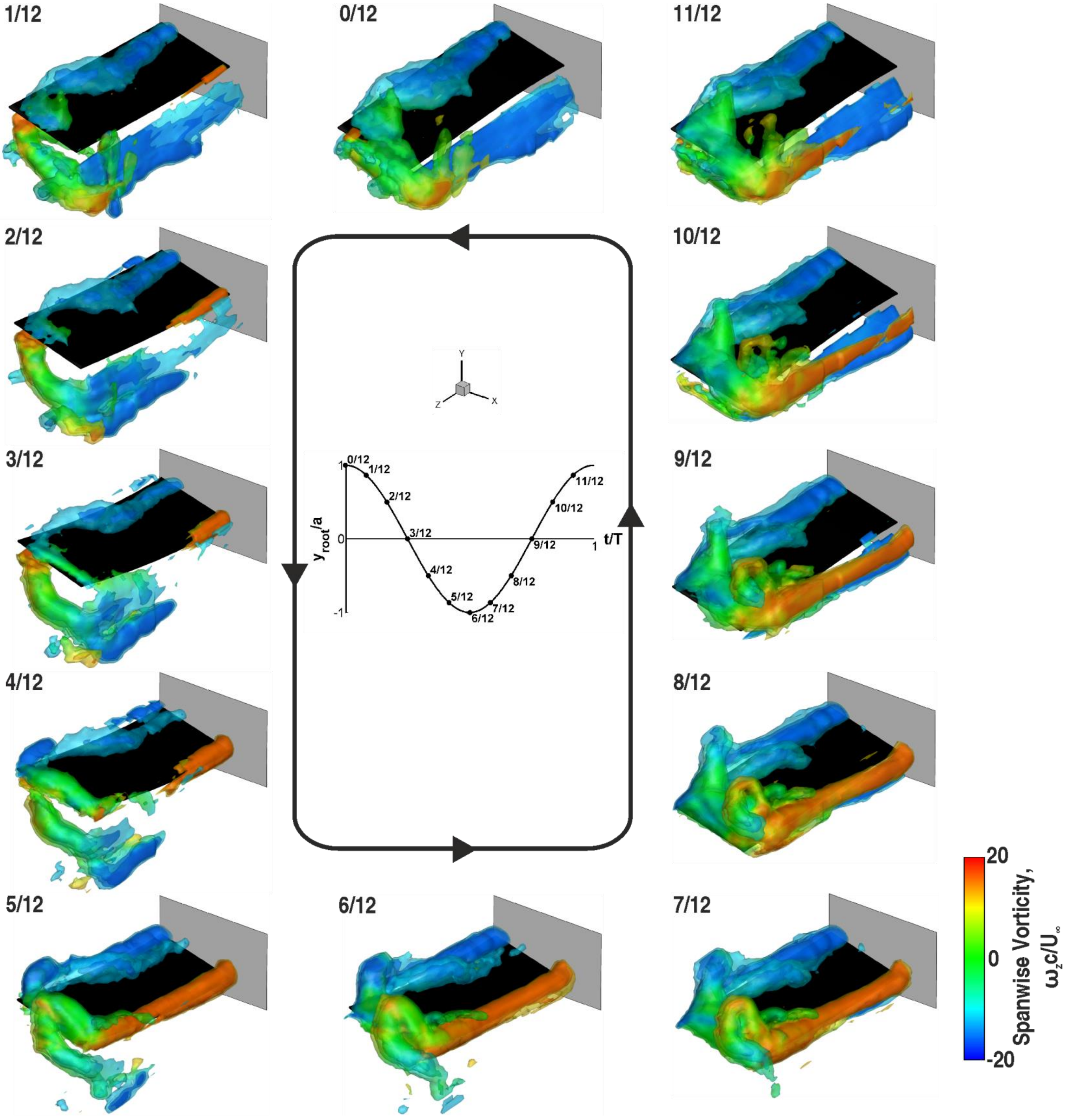

Fig. 53 Isosurfaces of phase-averaged vorticity magnitude ($\omega c/U_\infty$ = 12, 18, and 24) overlaid with spanwise vorticity for the highly flexible wing oscillating with Sr_c = 1.50. *sAR* = 3, *Re* = 10,000, α = 15º, *a/c* = 0.15.

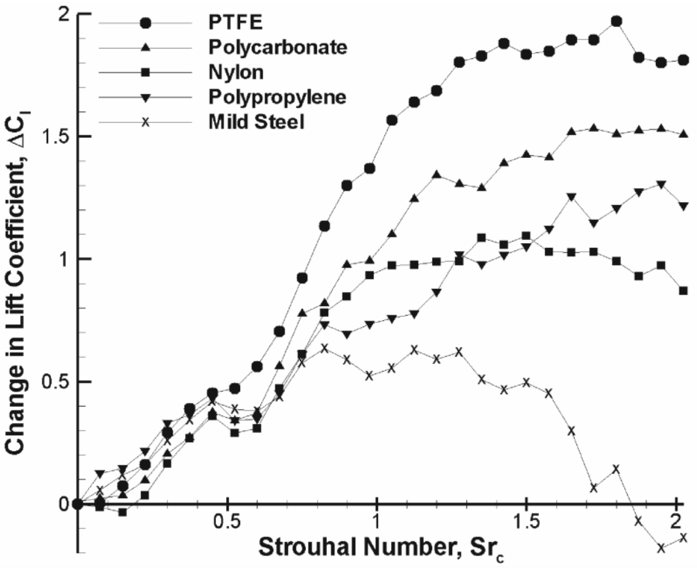

Fig. 54 Change, relative to $Sr_c = 0$, in time-averaged lift coefficient for rigid and flexible *sAR* = 1.5 wings oscillating with $a/c = 0.150$.

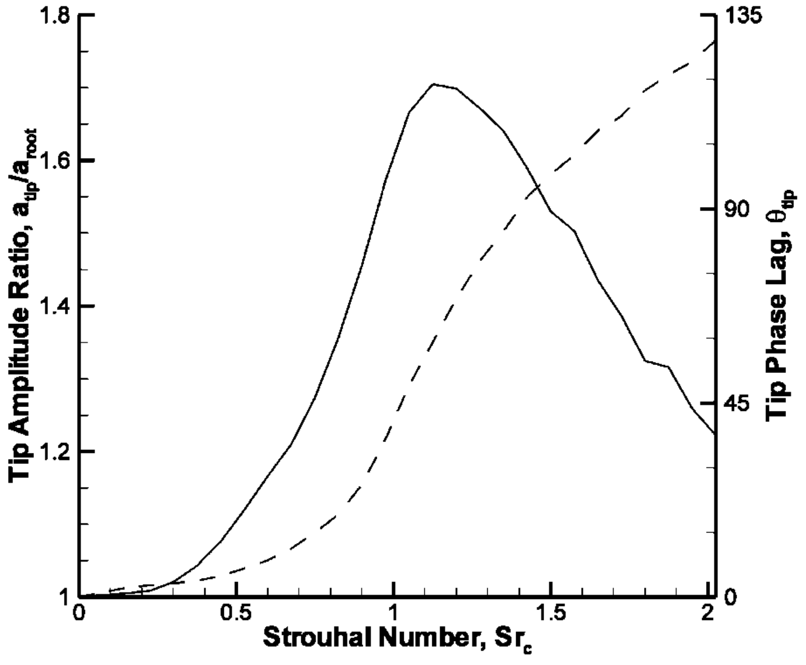

Fig. 55 Tip amplitude ratio (solid line) and tip phase lag (dashed line) against Strouhal number for the *sAR* = 1.5 PTFE wing.

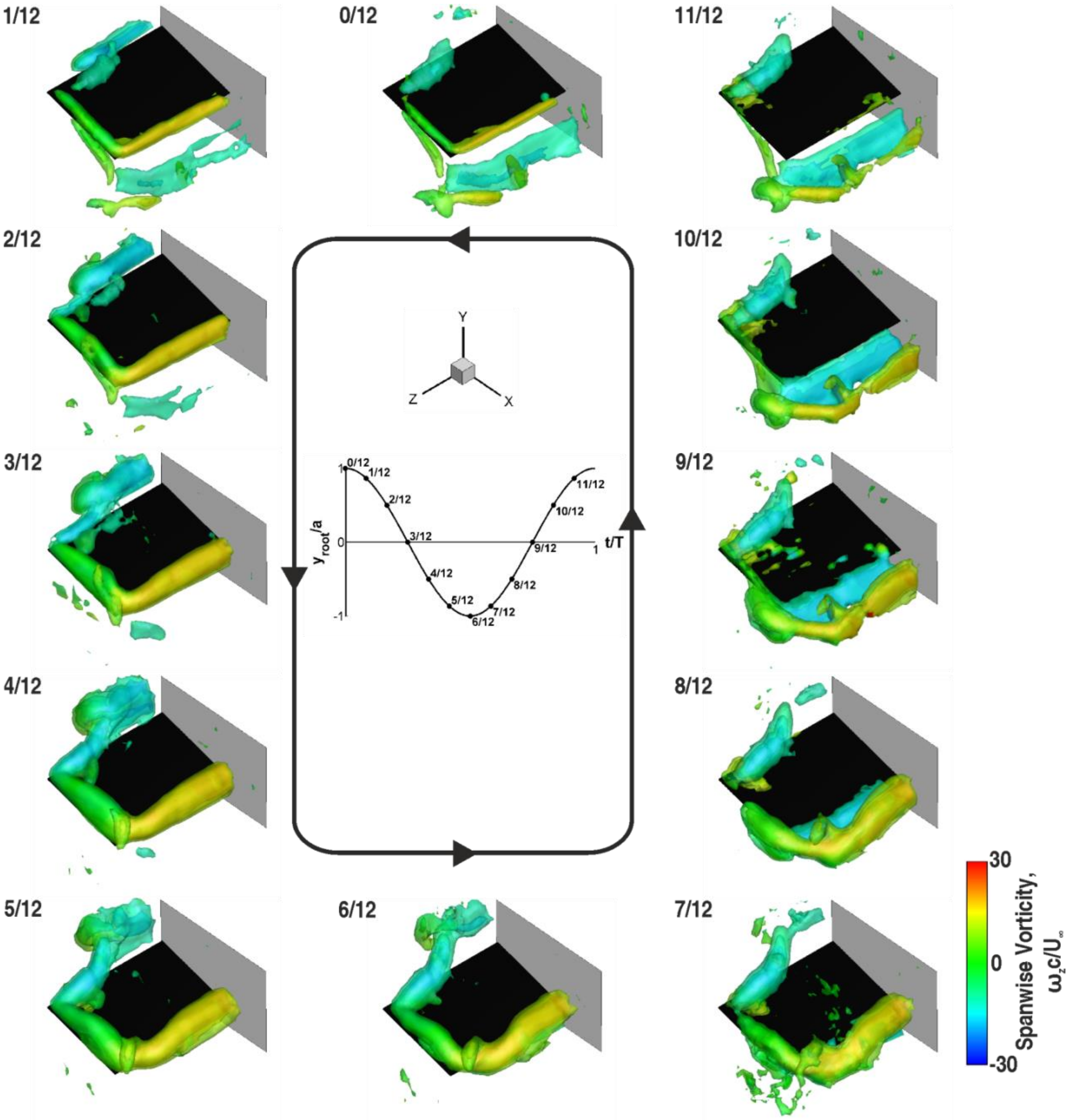

Fig. 56 Isosurfaces of phase-averaged vorticity magnitude ($\omega c/U_\infty$ = 12, 20, and 28) overlaid with spanwise vorticity for the *sAR* = 1.5 rigid wing oscillating with Sr_c = 1.500.

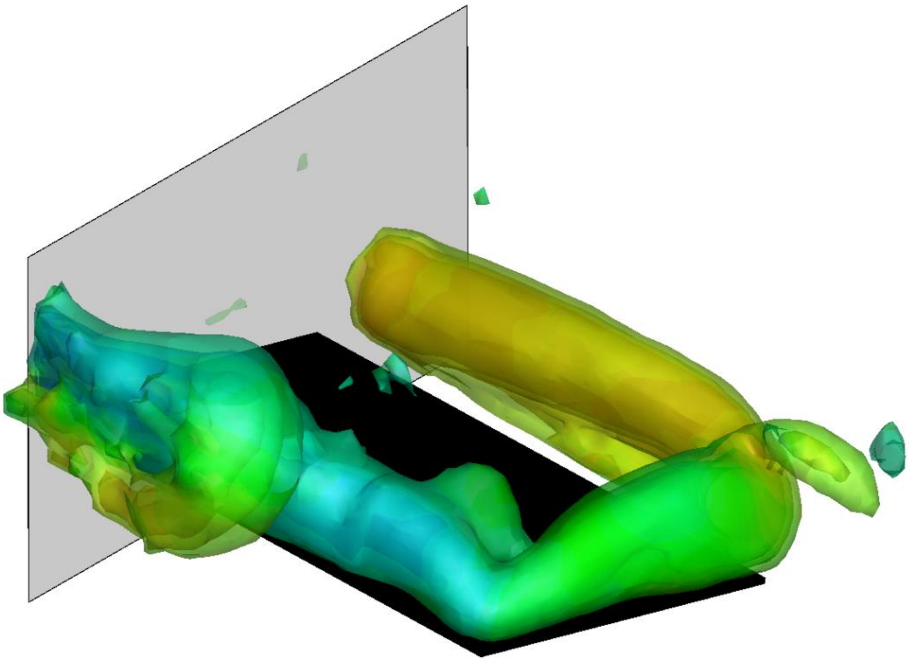

Fig. 57 LEV dipole from an upstream perspective for *t/T* = 4/12. The lower surface counter-clockwise LEV has gone beyond the upstream edge of the volume and is therefore only partially captured.

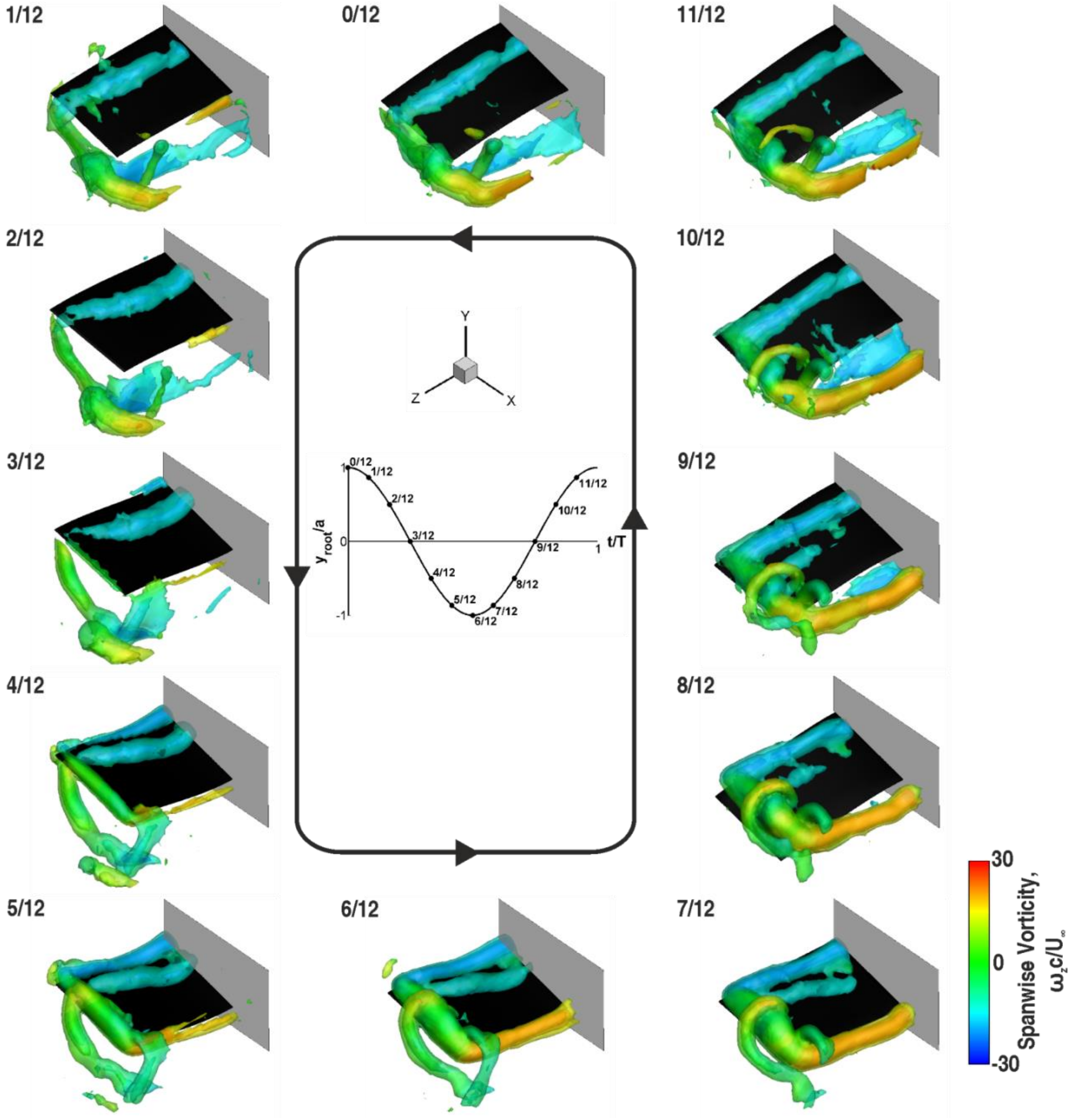

Fig. 58 Isosurfaces of phase-averaged vorticity magnitude ($\omega c/U_\infty$ = 15, 25, and 35) overlaid with spanwise vorticity for the sAR = 1.5 flexible wing oscillating with Sr_c = 1.500.